CHANGES IN TROPICAL CONVECTION AND CLOUD POPULATIONS WITH ITCZ WIDTH AND IMPLICATIONS FOR THE HADLEY CIRCULATION

A Dissertation

by

KYLE R. WODZICKI

Submitted to the Office of Graduate and Professional Studies of
Texas A&M University
in partial fulfillment of the requirements for the degree of

DOCTOR OF PHILOSOPHY

Chair of Committee,	Anita D. Rapp
Committee Members,	Courtney Schumacher
	Kenneth P. Bowman
	Steven F. DiMarco
Head of Department,	Ramalingam Saravanan

May 2021

Major Subject: Atmospheric Sciences

ABSTRACT

The Intertropical Convergence Zone (ITCZ) and Hadley and Walker circulations are primary drivers of the hydrologic cycle in the tropics. The ITCZ controls some of the wettest regions of the globe, while the Hadley circulation controls subtropical deserts and the Walker circulation acts to regulate convection within the ITCZ. As convection within the ITCZ drives the Hadley circulation, understanding the connections between ITCZ and circulation variability is vital to improving climate forecasts. Although long-term trends from observations and climate models indicate a narrowing of the ITCZ and an intensificaiton of associated precipitation in a warming climate, few studies have examined the relationship between ITCZ width and the characteristics of convection within the ITCZ. Using the Tropical Rainfall Measuring Mission (TRMM) precipitation feature (PF) database, Moderate Resolution Imaging Spectroradiometer (MODIS) level 3 data, an ITCZ identification database, and European Centre for Medium-Range Weather Forecasts (ECMWF) Reanalysis Interim (ERA-Interim) data the variability of cloud and convective populations are studied as a function of ITCZ width.

In the Pacific basin, convection is more (less) intense, with large (small) stratiform rain fractions and high (low) maximum echo-top heights, when the Pacific ITCZ is wide (narrow). This apparent discrepancy with long-term changes is linked to Walker circulation and El Niño-Southern Oscillation (ENSO) variability, with wide (narrow) ITCZs tending to occur during El Niño (La Niña).

Further analysis of variability within the Pacific, controlling for signals such as ENSO and the seasonal cycle, further indicates a Walker circulation influence over variations of convective intensity with ITCZ width. The relationships between the Hadley circulation and ENSO both within and outside of the Pacific Ocean show clear zonal variability, with a strengthening and widening (narrowing and weakening) of the circulation within (outside) the Pacific during El Niño.

To control for zonal differences, tropical ascent area fraction is used to study global variability in convection with changes in the area of ascent. Convection in the ascent region becomes more

intense (i.e., higher cloud-top heights and large stratiform area fractions) when tropical ascent area fraction is low; a relationship similar to that of long-term trends. In descent regions, variability in clouds with respect to tropical ascent area fraction differs between cloud regions (i.e., shallow cumulus and stratocumulus regions), but both indicate an intensification of subsidence.

DEDICATION

To my wife and my parents for their love and support

ACKNOWLEDGEMENTS

My career as a graduate student has been a long, often bumpy, road. While the path always appeared to be a straight line from A to B, I realize now that I was unable to see the many hills and valleys that awaited me along the way. This enormous opportunity I have been afforded, to study alongside some of the brightest minds in the field of Atmospheric Sciences, has been both amazing and terrifying. I am forever grateful to those that have helped me along the way, no matter how seemingly insignificant the help was, and I am especially thankful to those I can now call my friends. Of course, none of this would have been possible without my advisor, Dr. Anita Rapp.

From our first correspondence late in the application cycle for the Fall 2013 academic year, which resulted in both a rejection and acceptance letter from Texas A&M, to now, you have been an exceptional advisor and I could not imagine completing this work under anyone else. Through time crunches before conferences, my exceptionally slow writing pace, and seemingly endless rounds of revisions you have pushed me to become a better scientist and I thank you for that. I also appreciate you helping ensure that I was able to be a teacher's assistant for at least one semester during my graduate career, as it is a career path I still consider pursing. Lastly, I want to thank you for being so very kind and understanding about changes in life; getting married, commuting from Houston so my wife could start her career, and all the other little things. Thank you so much.

My committee members have also been an enormous part of my graduate career, helping to shape how I approach problems, analyze data, and present findings. Dr. Courtney Schumacher really opened my eyes to the world of tropical meteorology through her approach to ATMO 656 and has been a fantastic resource throughout my research. She asks some difficult questions, but it is all in the name of improving the science. Dr. Ken Bowman has been a mentor since serving as a committee member on my Masters degree, helping me become a proficient coder and data scientist. I had the honor of being his teaching assistant in a computer programming class for undergraduate students and I would be lying if I said it was not one of the most rewarding things I have done. Last, but certainly not least, I must thank Dr. Steven DiMarco for instilling a love of data in me through

his data analysis class. I learned so very much from you and cringe whenever I read a paper where a boxcar filter is used; oh so much ringing.

The final group of people I need to thank is my family and friends. Tara, my wife, where would I be without you. For all the times I felt I would never finish, wanted to quit, or felt generally lost, you were a guiding force of encouragement that helped make the light at the end of the tunnel a little bit brighter. I am still not sure exactly where life is going to take us after this chapter ends, but I know it will be amazing because it will be with you. I thank my parents for always being supportive of what I do and being there for me when I need them. My siblings, Ashley, Greg, and Justin have also been a great support system, allowing me to vent frustrations when hitting a road block and just generally being available to talk about life. To all the friends I have made at A&M that have helped me with debugging code, reading manuscripts, and sitting in on practice talks I am so thankful; Jack Cooney, Chris Siu, Kevin Smalley, Troy Arcomano, Adam Bell, Montana Etten-Bohm, Keith White, Rob Marter, and many others.

Thank you again everyone, I would not have been able to get this far without y'all.

A number of different datasets and programming packages were used to complete this work. The Pacific Intertropical Convergence Zone (ITCZ) mask dataset is available from the Texas Data Digital Repository at `https://doi.org/10.18738/T8/T5PH8N` (Wodzicki and Rapp 2016). The TRMM Precipitation Feature Database is available at `http://atmos.tamucc.edu/trmm/` (Nesbitt et al. 2000; Liu et al. 2008). TMI data are produced by Remote Sensing Systems and sponsored by the NASA Earth Science MEaSUREs DISCOVER Project. Data are available at `www.remss.com` (Wentz et al. 2015). Moderate Resolution Imaging Spectroradiometer (MODIS) Terra and Aqua level 3 gridded data were obtained from NASA's The Level-1 and Atmosphere Archive & Distribution System (LAADS) Distributed Active Archive Center (DAAC) server (Hubanks et al. 2019). ERA-Interim data were obtained from the ECMWF Meteorological Archival and Retrieval System (MARS) server via their python API (Dee et al. 2011). MEI version 2 data

were obtained from https://psl.noaa.gov/enso/mei/ (Wolter and Timlin 1993, 1998). The Helmholtz decomposition was done using the windspharm python package; code is available at https://ajdawson.github.io/windspharm/latest/ (Dawson 2016).

CONTRIBUTORS AND FUNDING SOURCES

Contributors

This work was supported by a dissertation committee consisting of advisor Professor Anita D. Rapp, Professor Courtney Schumacher, and Professor Kenneth P. Bowman of the Department of Atmospheric Sciences and Professor Steven F. DiMarco of the Department of Oceanography.

All work conducted for the dissertation was completed by the student independently.

Funding Sources

Graduate study was supported by a fellowship from the Texas A&M Hagler Institute for Advanced Study and by NASA grants NNX13AG91G and NNX15AD13G.

NOMENCLATURE

CAM	Community Atmospheric Model
CCKW	convectively-coupled Kelvin wave
CMAP	Climate Prediction Center Merged Analysis of Precipitation
CMIP5	Coupled Model Intercomparison Project Phase 5
CPAC	central Pacific
CWV	columnar water vapor
ECMWF	European Centre for Medium-Range Weather Forecasts
ENSO	El Niño-Southern Oscillation
EPAC	eastern Pacific
EPIC	Eastern Pacific Investigation of Climate
ERA-Interim	ECMWF Reanalysis Interim
ERSST	Extended Reconstructed Sea Surface Temperature
GCM	general circulation model
GPCP	Global Precipitation Climatology Project
HadISST	Hadley Centre Sea Ice and Sea Surface Temperature
ISCCP	International Satellite Cloud Climatology Project
ITCZ	Intertropical Convergence Zone
IWP	ice water path
LWP	liquid water path

MEI	Multivariate ENSO Index
MODIS	Moderate Resolution Imaging Spectroradiometer
OLR	outgoing longwave radiation
PDF	probability density function
PF	precipitation feature
PR	precipitation radar
RR	rain rate
RSS	Remote Sensing Systems
SPCZ	South Pacific Convergence Zone
SST	sea surface temperature
TAO	Tropical Atmosphere-Ocean
TMI	TRMM Microwave Imager
TRMM	Tropical Rainfall Measuring Mission

TABLE OF CONTENTS

Page

LIST OF FIGURES

FIGURE Page

1. INTRODUCTION

The hydrologic cycle is vital to life on earth, transporting moisture, and heat around the globe. In the tropics, the largest driver of the hydrologic cycle is the Hadley circulation; a thermally direct meridional overturning circulation with an ascending branch near the equator and descending branches that extend to 30° latitude in both hemispheres (Webster 2004). Through these ascending and descending branches, the circulation controls the driest and wettest regions around the globe, with deserts found within the descending branches of the circulation and the wettest regions within the ascending branch. The ascending branch of the circulation is typically referred to as the Intertropical Convergence Zone (ITCZ), an area of relatively low pressure that forms where the northern and southern hemispheric trade winds meet that is characterized by heavy precipitation and extensive cloud cover (Riehl and Malkus 1958; Waliser and Gautier 1993; Wodzicki and Rapp 2016). As convection within the ITCZ is the driving force behind the Hadley circulation, changes in either of these tropical features lead to changes in the other. Using a simple model Lindzen and Hou (1988) found that the latitudinal location of heating (i.e., the location of the ITCZ) impacts the strength of the overturning circulation. Hou and Lindzen (1992) furthered their previous work by studying the impacts of the meridional extent of heating, finding that reducing the extent of heating led to a strengthening of the overturning circulation. The relationship between convection in the ITCZ and the overturning circulation has been the subject of many studies (e.g., Hack et al. 1989; Dodd and James 1997; Fierro et al. 2009), illustrating the importance of understanding how these tropical features interact. This knowledge may help explain predicted variability in a future, warmer climate.

Quantifying the variability of the Hadley circulation has been the subject of many studies over the last few decades. Many of these studies used data from reanalyses or general circulation models (GCMs) to compute the zonal-mean mass meridional stream function to determine the strength and meridional extent of the circulation. Mitas and Clement (2005) performed such an analysis of the overturning circulation using three reanalysis datasets, a rawinsonde dataset, and model data

from the Community Atmospheric Model (CAM). While two of the reanalyses and the CAM data indicated a strengthening of the circulation over the past few decades, the third reanalysis and the observational data showed no trend. More recent studies of trends in the Hadley circulation using a wider array of reanalyses (i.e., Stachnik and Schumacher 2011; Nguyen et al. 2013) found evidence of strengthening and poleward expansion of the overturning circulation; however, the strengthening signal varied greatly between the reanalyses. The poleward expansion of the circulation has also been observed in various observational datasets such as outgoing longwave radiation (OLR) and precipitation data (Hu et al. 2011; Zhou et al. 2011). With uncertainty surrounding the change in circulation strength, a look at changes in ITCZ characteristics may be of use.

The identification and characterization of the ascending branch of the Hadley cell, the ITCZ, has also been the focus of many studies over the years. Waliser and Gautier (1993) analyzed the mean latitude of the ITCZ along with the seasonal variability in ITCZ location around the globe at monthly timescales. More recent studies of ITCZ variability have been performed using satellite observations and statistical methods for identification in the Pacific Ocean (Bain et al. 2011) and reanalysis data to identify convergence zones around the globe (Berry and Reeder 2014). However, these studies did not attempt to quantify the intensity or extent of the zone of convection associated with the ITCZ, which is important for quantifying changes in the hydrologic cycle and cloud radiative forcings. To study broader variability of the ITCZ, such as convective intensity and meridional extent, Wodzicki and Rapp (2016) developed an ITCZ characteristics database for the Pacific Ocean using the methods of Berry and Reeder (2014) to identify the center of the ITCZ and Global Precipitation Climatology Project (GPCP; Huffman et al. 2009) and Remote Sensing Systems (RSS) Tropical Rainfall Measuring Mission (TRMM) Microwave Imager (TMI; Hilburn and Wentz 2008) rain rate (RR) data to identify ITCZ extent. The RR data were also used as a proxy for the intensity of convection (Cheng and Houze 1979; Short et al. 1997) associated with the ITCZ. Wodzicki and Rapp (2016) found that the Pacific ITCZ narrowed, and associated convection (precipitation) intensified over the period Jan. 1979 - Dec. 2014. Their findings are consistent with studies of changes in precipitation that have shown an apparent narrowing and intensifica-

tion of the ITCZ, with increases in precipitation near the climatological center latitude of the ITCZ and decreases in precipitation to the north and south (Zhou et al. 2011; Gu and Adler 2013). The changes are also in line with changes hypothesized by the "upped-ante mechanism" (Chou and Neelin 2004), wherein a warming climate raises the moisture threshold, or ante, for convection to occur across the tropics. In the deep tropics (i.e., the ITCZ region), the increased ante is easily met through increased evaporation and moisture convergence; however, convection at the margins of the convective zone is suppressed as the new ante is more difficult to meet. This, ultimately, leads to a narrowing of the ITCZ and intensification of rainfall. But, how exactly does the morphology of convection vary with variations in ITCZ width?

Tan et al. (2015) used International Satellite Cloud Climatology Project (ISCCP) cloud-top height and optical thickness data and GPCP RRs to determine what types of cloud systems (e.g., shallow cumulus, congestus, deep convection, etc.) were responsible for the observed changes in ITCZ precipitation intensity. After identifying various cloud types using a k-means clustering algorithm applied to cloud-top height and optical thickness data, and attributing RRs to the various cloud types, they found that increases in the frequency of the regime they associated with deep, organized convection contributed the most to changes in precipitation. As large, organized convective systems produce much of the rainfall observed in the tropics even though they make up only a small percentage of all convection (Nesbitt et al. 2000; Liu et al. 2008), it makes sense that changes in the frequency of such storms would be the most influential to changes in RR. However, this raises the question as to whether these convective systems are just becoming more frequent, or if their convective characteristics are changing as their frequency varies. The work of Tan et al. (2015) was limited in this respect as they were unable to study the internal structure of convection due to the datasets used. How the morphology of convection changes, coupled with the apparent changes in frequency, is key to understanding how convection is linked with large-scale circulation changes in a warming climate.

Studies of climate model output indicate that the ITCZ, or ascent region of the Hadley circulation, will continue narrowing and intensifying as the climate warms (Lau and Kim 2015; Su

et al. 2014, 2017, 2019). Based in these projections, and long-term observed trends, the following hypothesis is tested:

H1. Pacific ITCZ convection is more intense (i.e., taller with larger stratiform area fractions) when the Pacific ITCZ is narrow.

Results are presented in Chapter 2 and reproduced from a paper published in the Journal of Climate (Wodzicki and Rapp 2020). To test this hypothesis, data from the TRMM precipitation feature (PF) database (Nesbitt et al. 2000; Liu et al. 2008) and the Pacific ITCZ characteristics database (Wodzicki and Rapp 2016) are used to study the morphology of convection within wide and narrow ITCZ width regimes. As the TRMM data period is relatively short (roughly 17 years), the use of anomalously narrow and wide ITCZ months is used to quantify differences between convective populations at the two extremes of the ITCZ width distribution. The convective characteristics of features, such as areal extent, maximum echo-top height, and stratiform area fraction, are then compared between the width regimes to determine how convection varies with Pacific ITCZ width. The analysis ultimately led to a rejection of the hypothesis for the Pacific as relatively intense convection is more frequent under the wide ITCZ regime than the narrow. The findings are attributed to the strong influence of El Niño-Southern Oscillation (ENSO) in the Pacific dominating the variability in convection and ITCZ width; the ITCZ tends to be wide, with more intense convection, under El Niño and narrow, with less intense convection, under La Niña (Bain et al. 2011; Wodzicki and Rapp 2016; Henderson et al. 2018). This result shows that a more complete understanding of the driving forces of variability in the Pacific, and their full impacts on the previous results, is necessary to guide further research into the relationship between convection and variability in ITCZ width.

Chapter 3 aims to better understand the influence of variability in the Pacific on convection by mitigating various forms of variability that may have impacted the analysis of Chapter 2. This is done by excluding months where double ITCZs or large ENSO events occurred and analyzing multiple different zonal domains across the Pacific. However, similar results were obtained to those of the previous analysis, leading to the conclusion that convection in the Pacific ITCZ is most

influenced by changes in the Walker circulation and the associated zonal sea surface temperature (SST) gradient. These results indicate that variability in the Pacific Ocean in the current climate differs from that of future climates, due mainly to regional variability in the overturning circulation (Schwendike et al. 2015; Martin et al. 2020). Thus, a different metric is needed to understand the link between the width of the ascending region and the morphology of convection.

Su et al. (2019) used tropical ascent area fraction (A_u) as a means to study changes in the overturning circulation in climate model output. They found that as A_u decreased (narrowed), precipitation intensity increased, consistent with current observations and model projections of ITCZ narrowing. They also discussed changes in the descent region of the circulation, as cloud-radiative feedbacks across the tropics are one of the largest sources of uncertainty in climate predictions (Bony and Dufresne 2005). To further improve on the analysis of Chapter 2, A_u is calculated from reanalysis data to study how convective and cloud properties vary in tropical ascent and descent regions as A_u varies. TRMM PF data are again used to study convection within the ascent region, while Moderate Resolution Imaging Spectroradiometer (MODIS) level 3 data (Hubanks et al. 2019) are used to study cloud variability within both the ascent and descent regions. The use of A_u as a metric for ITCZ variability enables global analysis, reducing the influence of any one region on the results and allowing for more consistent comparison to climate model predictions. Based on the results from observational and modeling studies discussed above, the following hypotheses are tested in Chapter 4:

H2. Convection within ascent areas will become stronger (weaker) when tropical ascent area fraction is low (high).

H3. In subsidence regions, cloud-top heights will increase and cloud fraction and liquid water path (LWP) will decrease with low tropical ascent area fraction

Strengthening of convection consists of convective feature and cloud characteristics shifting to larger areal extents and increased stratiform area fractions, RRs, cloud fractions, LWPs, and ice water paths (IWPs). As the strength of subsidence is hypothesized to decrease as A_u decreases

(Held and Soden 2006; Lu et al. 2007; Su et al. 2019), clouds and convection will be able to grow out of the boundary layer, leading to the hypothesized changes in the subsidence regions (Myers and Norris 2013; Su et al. 2014).

Convection in the ascent regions of the tropics is found to become stronger and more organized, with larger stratiform area fractions and increased RRs as A_u decreases. Cloud fraction also increases, along with IWP, as A_u decreases, adding more support to a strengthening of convection with narrowing ascent. These result support the **H2** hypothesis. The descent regions are a bit more complicated, with evidence of stronger subsidence in descent regions as A_u decreases. There are also large regional variations in the relationship between cloud properties and A_u across the descent region, with stratocumulus cloud regions showing increased cloud amounts while shallow cumulus regions show decreased cloud amounts with narrowing. While the results are similar to long-term observationally-based studies (Su et al. 2020; Lau and Tao 2020), there seems to be differences between variability in the current climate and those projected by climate models. These differences may be the result of the aforementioned difficulty climate models have with accurately representing cloud radiative feedbacks (Bony and Dufresne 2005), or that the long-term warming signal has not yet become larger than the internal variability of the current climate; i.e., the time of emergence has not yet occurred (Hawkins and Sutton 2012).

2. VARIATIONS IN PRECIPITATING CONVECTIVE FEATURE POPULATIONS WITH ITCZ WIDTH IN THE PACIFIC OCEAN*

2.1 Introduction

The accurate prediction of changes in the hydrologic cycle is of great importance as water is essential for life. Shifts in the locations of the world's deserts and rain belts could spell disaster through loss of crops, property, and even life. In the tropics and extra tropics, changes in the hydrologic cycle can broadly be linked to changes in the Hadley and Walker circulations. Numerous studies have aimed to quantify changes in the Hadley circulation in a warming climate using data from reanalyses (e.g., Mitas and Clement 2005; Stachnik and Schumacher 2011; Nguyen et al. 2013), general circulation models (e.g., Mitas and Clement 2006; Lu et al. 2007; Lau and Kim 2015; Su et al. 2014), and observations (e.g., Hu and Fu 2007; Seidel et al. 2008; Hu et al. 2011). There is disagreement between studies as to how the strength of the Hadley circulation has changed in recent decades (Hu et al. 2018); however, the general consensus is that the Hadley circulation has expanded poleward. While studies of changes in the future climate generally agree that the Hadley circulation will become weaker, Su et al. (2014) noted that the circulation goes through complex structure changes as the climate warms. Similar studies of the Walker circulation also disagree on the change of the circulation's strength; some found weakening and westward shift (e.g., Tanaka et al. 2004; Vecchi et al. 2006; Power and Smith 2007; Schwendike et al. 2015), while others found strengthening (e.g., Meng et al. 2012; L'Heureux et al. 2013; Sohn et al. 2013). As the ITCZ is the main driver of the Hadley circulation and influences the Walker circulation, changes in the intensity of convection within the ITCZ impacts both of these circulations (Hack et al. 1989; Hou and Lindzen 1992; Dodd and James 1997; Webster 2004). Therefore, it is important to understand the link between broader ITCZ characteristics and the convective systems within the ITCZ.

One of the first major studies of the ITCZ's climatological location and seasonal migration

*Reprinted with permission from "Variations in precipitating convective feature populations with ITCZ width in the Pacific ocean" by Kyle R. Wodzicki and Anita D. Rapp, 2020. *J. Climate*, **33**, 4391–4401, © Copyright [21 April 2020] by American Meteorology Society.

used observations of highly reflective clouds to identify the ITCZ (Waliser and Gautier 1993), while more recent studies have applied statistical models to observations (Bain et al. 2011) and thresholding techniques to reanalysis data (Berry and Reeder 2014) to study the ITCZ. Building off the methods of Berry and Reeder (2014), Wodzicki and Rapp (2016) quantified the ITCZ width and precipitation intensity and determined that the ITCZ has been narrowing and intensifying over the past 30+ years, possibly due to an increase in the frequency of mid-tropospheric dry layers (Bartos et al. 2018). Their findings are in line with other observational studies that noted long-term increases in tropical precipitation rate, mainly in the ITCZ region (Lau and Wu 2007; Zhou et al. 2011), and lend support to climate model predictions of further narrowing and intensification in the future (Lau et al. 2013; Lau and Kim 2015; Su et al. 2017, 2019). While the aforementioned studies focused on long-term trends in ITCZ characteristics, many studies have also noted a link between convective systems and ITCZ width variations at other timescales, from synoptic to interseasonal.

At synoptic timescales, Straub and Kiladis (2002) and Serra and Houze (2002) found that as Kelvin waves passed over a region, convection rapidly initiated and organized along the central axis of the ITCZ. This increase in organized convection widened the ITCZ, with the increase in ITCZ width propagating with convection associated with the Kelvin waves as they moved across the ocean basin. Serra and Houze (2002) also noted that the passage of Kelvin waves initiated hurricane development after which the ITCZ tends to completely break down, with deep convection disappearing and ITCZ width decreasing to near zero. A more recent study by Dias and Pauluis (2011) found a relationship between ITCZ location and width and the speed of convectively-coupled Kelvin waves (CCKWs). They suggest that the meridional circulation associated with the CCKWs modulates ITCZ width and precipitation, indicating a link between the broader ITCZ width and the characteristics of the convective systems within.

Dias and Pauluis (2011) also noted that the ITCZ is abnormally wide during El Niño events in the central Pacific ($180° - 130°$W), consistent with the observational findings of Wodzicki and Rapp (2016, 160°E–160°W). Simple Walker circulation models (e.g., Bretherton and Sobel 2002) also show a wider zone of convection when the SST gradient across the Walker circulation weak-

ens during El Niño. Insomuch as the ITCZ tends to be wide during El Niño and narrow during La Niña, some studies have indirectly looked at variations in characteristics of convection in different ITCZ width regimes. Masunaga et al. (2005) used TRMM satellite data to show that during El Niño events, deep stratiform and convective systems became much larger and more frequent, taking the place of shallow convection, when compared to La Niña. Henderson et al. (2018) found very similar changes from deep isolated systems in the La Niña phase to large, organized systems with increased stratiform rain area during El Niño. This is further supported by Stephens et al. (2018), who found evidence for the Bjerknes feedback in observations that show large positive latent and radiative heating perturbations with super-Clausius–Clapeyron precipitation responses in the warming, moistening ITCZ region during El Niño. However, it remains unclear how the population and character of convective clouds within the ITCZ vary to produce the observed precipitation and heating rate perturbations that feedback on these large-scale circulations as similar radiative and latent heating perturbations could come from very different cloud populations. There are some indications that the character of convective systems in the tropics may be shifting as the convective zones narrow at longer, decadal, timescales (Tan et al. 2015), but this has not been specifically analyzed in the context of expansion and contraction of the ITCZ at shorter, annual or seasonal, timescales.

The aim of the present study is to better understand the relationship between the variations in large-scale ITCZ width and characteristics of convection (e.g., RR, maximum height, and stratiform/convective partitioning). This will be done through the analysis of convective features located within the ITCZ based on the Pacific ITCZ identifications from Wodzicki and Rapp (2016). While previous studies have focused on long-term changes in ITCZ precipitation intensity and location, the relatively short TRMM data record limits the present study to shorter timescales. Thus, features in two different ITCZ width regimes (wide and narrow based on the upper and lower quartiles of the width distribution, respectively) are compared to understand the relationship between the distribution of convection characteristics and variations in ITCZ width.

2.2 Data and Methods

Wodzicki and Rapp (2016) created an ITCZ climatology that provides information about the location, width, and RRs within the Pacific ITCZ (160°E–100°W) on a monthly-mean timescale. To identify the ITCZ they used monthly 1000–850 hPa layer mean *u*- and *v*-wind components to compute divergence, gradient of divergence, and Laplacian of divergence. Locations where the gradient of divergence equaled zero were taken as the first guess ITCZ center, with the divergence and Laplacian of divergence fields used to mask out regions of divergence and relative minima in the divergence field, respectively. The 850-hPa wet-bulb potential temperature was used as a final mask, limiting identifications to tropical regions. After the ITCZ center was identified, ITCZ boundaries were located by iterating from the ITCZ center to the north and south to find the latitude where RR fell below a threshold of 2.5 mm day^{-1}. While their work focused on long-term trends in ITCZ characteristics using long time-series GPCP RRs (Adler et al. 2003), the present study utilizes TMI RRs for boundary identifications. The two major benefits of using TMI-based ITCZ identification over GPCP are 1) the TMI ITCZ climatology is already available from Wodzicki and Rapp (2016) and 2) the TMI sensor is on the TRMM satellite with the precipitation radar (PR), which is used to define convective features.

The TRMM satellite was launched in 1997 to further the understanding of precipitation in the tropics (Simpson et al. 1988; Kummerow et al. 1998). As the first satellite to feature a PR, TRMM provided invaluable information about internal precipitation structures, allowing for improved characterizations of precipitating convection in the tropics. However, with over 16 years of data, studying the distributions and morphology of precipitating systems using pixel-level data can be cumbersome. The work of Nesbitt et al. (2000) and Liu et al. (2008) greatly reduced data processing requirements through the development of a precipitation feature (PF) database. The current study uses their radar PF definition, defined as a single or contiguous group of PR pixels that have RRs greater than 0 mm hr^{-1}, because the convective characteristics used here to quantify convective intensity (i.e., maximum height reached by the PF, RR, area, and stratiform and convective partitioning) are all derived from the PR. It is worth noting that the spatial and temporal resolutions

of radar PFs are highly variable as they are limited by the presence of rain and the spatial and temporal resolutions of TRMM. The relatively narrow swath width ($\sim$ 215–km) of TRMM also limits the maximum size of PFs that can be sampled; however, Nesbitt et al. (2000) found that only 17% of PFs are affected and noted that while this does cause some truncation in the area distribution of PFs, other characteristics remain unbiased. As convection can be greatly influenced by its environment (Derbyshire et al. 2004; Rapp et al. 2011; Hohenegger and Stevens 2013), it is advantageous to consider changes in convective characteristics with changes in the ITCZ environment.

To do this, PFs are matched to RSS TMI version 7 (Wentz 1997; Hilburn and Wentz 2008) data on a 0.25°x0.25° grid at daily resolution. PFs are matched to the closest possible TMI time and the nearest grid box using a nearest neighbor method based on the center latitude and longitude of an ellipse fitted to the PF (Liu 2013). Using the monthly ITCZ center and boundary locations, each PF and TMI grid box are assigned an ITCZ flag and a distance from the ITCZ center; PFs within the ITCZ are hereafter referred to as ITCZ PFs. The variables of interest in the present study are PF area, RR, stratiform fraction, and maximum height, and TMI columnar water vapor (CWV) and SST. PF area is calculated by multiplying the number of pixels in the feature by the size of each pixel and the RR is average RR over the entire feature. To reduce bias, PFs with fewer than four pixels are excluded from the analysis as these very small, very frequent features can introduce noise (Nesbitt et al. 2000).

As previously discussed, modeling studies suggest a link between the width of the ITCZ and the characteristics of convection within the ITCZ (Chou and Neelin 2004; Neggers et al. 2007). Thus, we partition our data into wide and narrow ITCZ regimes where a wide (narrow) ITCZ is any ITCZ that has a deseasonalized zonal-mean width anomaly (%) above (below) the 75th (25th) percentile of the ITCZ width anomaly distribution for the 17-year period from December 1997 through September 2014. All analysis is also performed across the bulk of the Pacific basin from 160°E-100°W. The far eastern Pacific and far western Pacific are excluded to reduce the influence of spurious ITCZ identification in the North American monsoon region and the South Pacific Convergence Zone (SPCZ), respectively. While continental areas may be present in the

northern and southern regions of the domain, any PFs over such areas are excluded so that only PFs over the ocean are considered.

Using the matched PF database, monthly zonal median values for PF area, maximum height, and RR are computed for 2.5° bins centered on the ITCZ center. Median values are used as there tends to be many small and very few large PFs, which skews the mean values. These data are then deseasonalized to calculate percent anomalies. Using the deseasonalized anomalies from months above the upper and below the lower quartiles of the ITCZ width distribution, the average deviations from the mean state of the PF characteristics are determined. The significance of anomalies throughout the analysis are determined using a simple bootstrapping method wherein all deseasonalized anomalies are randomly resampled, with replacement, 10,000 times. A sampling size of 50 is used because that is roughly one quarter the number of months analyzed, giving a sample size equal to the number of months above (below) the upper (lower) quartile of the ITCZ width distribution. The average of each resample is computed, giving 10,000 realizations of the mean anomalies. An anomaly is determined to be significant if it falls in the top or bottom 2.5% of the bootstrapped distribution, giving a two-tailed test at the 95% confidence level.

2.3 Results

2.3.1 PF Populations

To gain a general understanding of the changes in convection in different ITCZ width regimes, Figure 2.1 shows the average zonal anomalies with wide ITCZ months (above upper quartile) in red and narrow ITCZ months (below lower quartile) in blue. Anomalies that are significantly different from the mean at the 95% level are indicated with an 'X'. From Figures 2.1a and b, PFs tend to be larger and deeper when the ITCZ is wide, with maximum heights 5-14% higher than average across the ITCZ. RR shows a more interesting picture (Figure 2.1c), with wide months having below average RRs across the ITCZ region while narrow months have above average RRs. While this seems at odds with previous studies that have shown RRs increasing as convection becomes larger and deeper (DeMott and Rutledge 1998; Nesbitt et al. 2006), this result is due to the use of

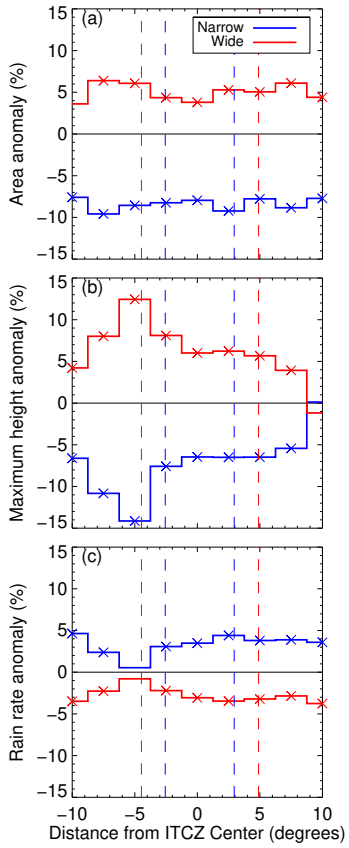

Figure 2.1: Means of zonal median percent anomalies for (a) PF area, (b) maximum height reached by the PF, and (c) RR. Blue (red) lines correspond to months below the lower (above the upper) quartile of the ITCZ width distribution. Xs indicate anomalies that are significantly different from zero at the 95% level. Distances are relative to the center of the ITCZ (positive north) and are in units of degrees. Vertical dashed lines show the mean location of the northern and southern ITCZ boundaries for the narrow and wide regimes.

conditional PF-averaged RR, not area-averaged RR, in the present study. As PFs become larger they will contain larger stratiform areas that tend to have a much lower instantaneous RR than small cumulus dominated by convective RRs. This acts to suppress the storm-averaged RR, while area-averaged RR would still be above normal.

To gain a better sense of how the PF population differs between the narrow and wide ITCZ regimes, PFs are partitioned into cumulus, congestus, and cumulonimbus regimes, based on maximum height of the PF, using a slightly modified version of the definitions from Johnson et al. (1999) with bins of 0–5 km for cumulus, 5–10 km for congestus, and 10–20 km for cumulonimbus. Figure 2.2 shows the zonal distribution of clouds by fractional occurrence for cumulus, congestus, and cu-

mulonimbus for narrow and wide months. It is worth noting that, on average, cumulus, congestus, and cumulonimbus clouds generate roughly 7%, 27%, and 67% of all rain, respectively, across the ITCZ. From this figure it is clear that most of the anomalies observed in Figure 2.1 are due to differences in cumulus and congestus clouds, with cumulus (congestus) clouds occurring more frequently when the ITCZ is narrow (wide). Figure 2.2c shows that cumulonimbus are roughly 30-50% more frequent in the wide regime than the narrow across the ITCZ; however, cumulonimbus account for a small percentage (<10%) of all clouds. What is perhaps more interesting is that there are roughly the same number of clouds across the ITCZ during wide and narrow months (not shown), which means that as the ITCZ narrows cumulonimbus clouds become less frequent and there is a shift from congestus to cumulus, indicating a shift to shallow, weaker convection. Along with this shift in cloud frequency is a shift in the percent contribution to total rain in the wide (narrow) regime to 5% (10%) for cumulus, 24% (31%) for congestus, and 71% (59%) for cumulonimbus.

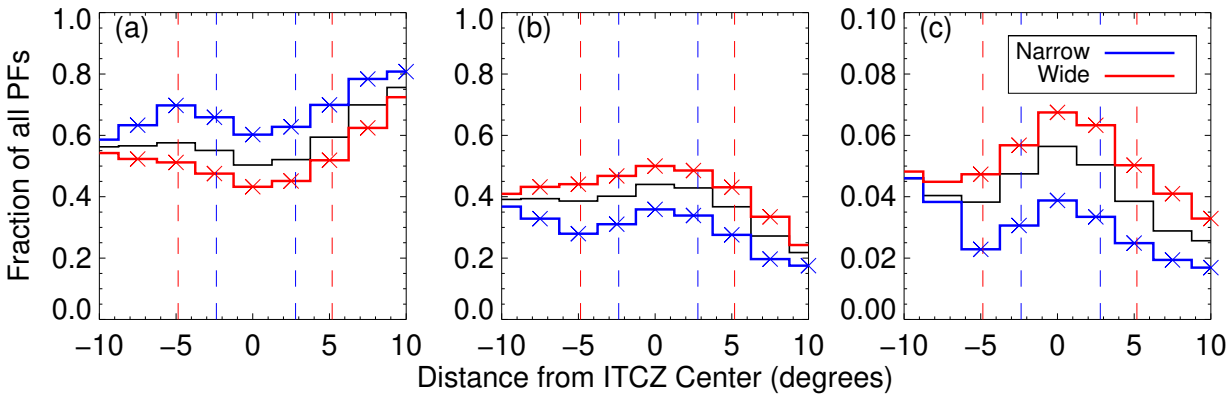

Figure 2.2: Zonal fractions of PFs by type for (a) cumulus, (b) congestus, and (c) cumulonimbus. Blue (red) lines correspond to months below the lower (above the upper) quartile of the ITCZ width distribution. Xs indicate anomalies that are significantly different from the mean at the 95% level. Distances are relative to the center of the ITCZ (positive north) and are in units of degrees. Vertical dashed lines show the mean location of the northern and southern ITCZ boundaries for the narrow and wide regimes. The sum of all three histograms is unity.

2.3.2 PF Convection Characteristics

To further study the changes in PF characteristics in different ITCZ width regimes, joint histograms of PF characteristics are used. Figures 2.3 and 2.4 show joint histograms for PF maximum height and area, respectively. To create these figures, monthly joint histograms are generated for the entire TRMM period (Dec. 1997 through Sep. 2014), showing the frequency of PFs with a given characteristic (e.g., maximum height of 5 km) at a given distance from the ITCZ center (e.g., $\pm 1.25°$). Each monthly histogram is then scaled to show the percentage of PFs with a given attribute. Figure 2.3a shows the average distribution for all months where, as an example, 10–15% of PFs that are $\pm 1.25°$ from the ITCZ center have maximum heights of 5–5.5 km. The monthly joint histograms are then deseasonalized and converted to percent anomalies using data from the full TRMM period. These anomalies are then averaged for months that fall above the upper (wide) and below the lower (narrow) quartiles of the ITCZ width distribution, with the average anomalies shown in panels b and c, respectively, of Figures 2.3 and 2.4. Vertical gray lines show the average

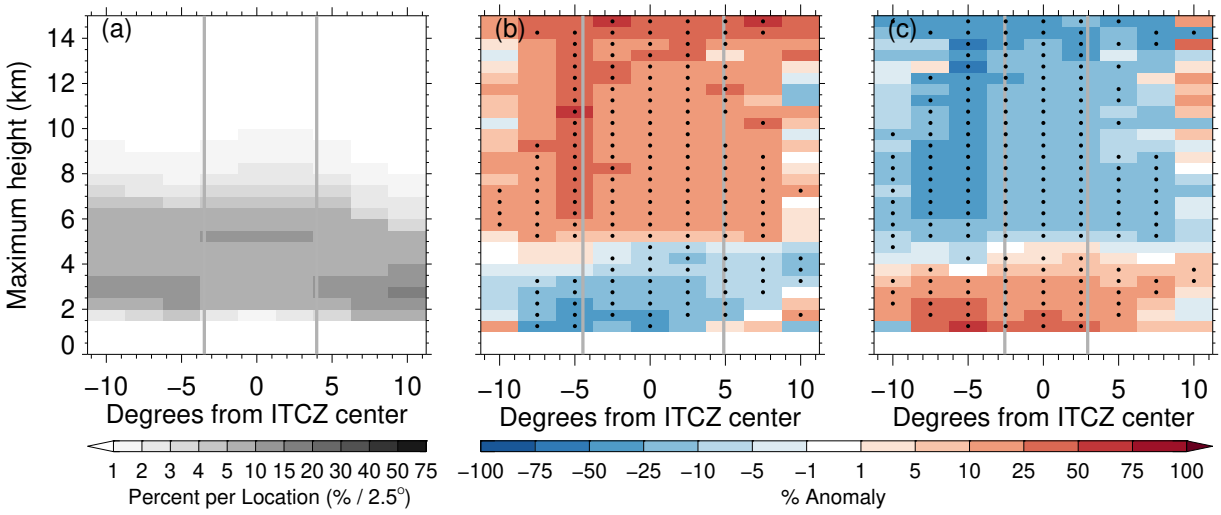

Figure 2.3: Joint histograms of PF maximum height and distance from the center of the ITCZ for (a) climatology, (b) mean of monthly percent anomalies in wide ITCZ months, and (c) mean of monthly percent anomalies in narrow ITCZ months. Distances are relative to the center of the ITCZ (positive north) and are in units of degrees. The vertical gray lines in all panels represent the location of the ITCZ boundaries for each data subset. Stippling indicates anomalies that are significantly different from zero at the 95% level.

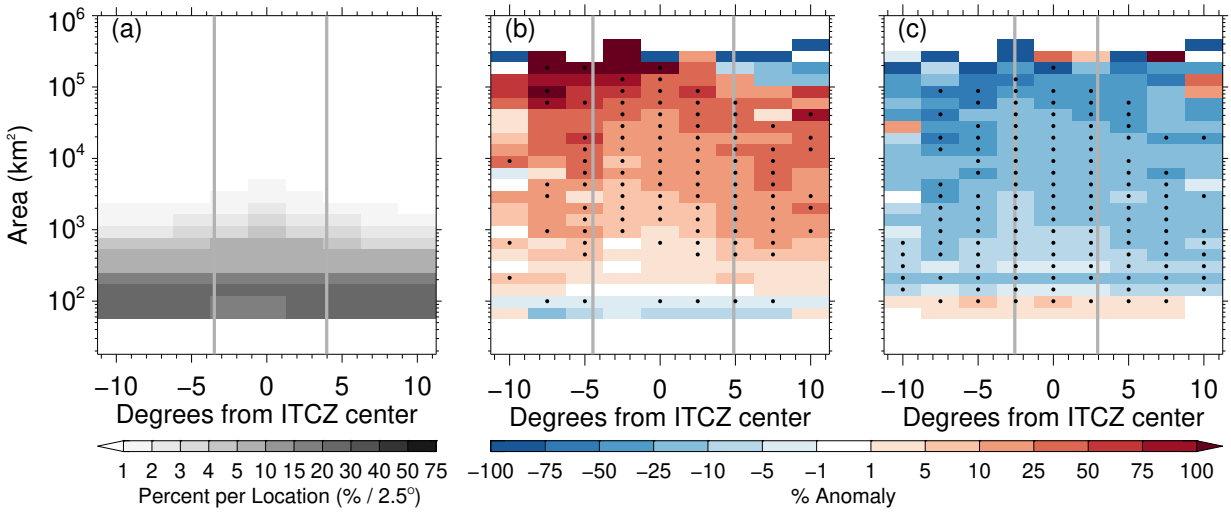

Figure 2.4: As in Figure 2.3, but for PF area. Area bins are logarithmic. Note that only data before August 2001 are included in the smallest area bin ($\sim$ 55–81 km^2).

locations of the ITCZ boundaries over the respective months of each panel and stippling in panels b and c indicate significant departures from the mean state at the 95% level. Note that in Figure 2.4, only data before August 2001 are included in the smallest area bin ($\sim$ 55–81 km^2) when computing means and anomalies because of the difference in pre- and post-boost pixel sizes.

From Figure 2.3a it is clear that the majority of PFs have heights between 2–8 km, with the frequency of deeper storms (i.e., heights greater than 8 km) increasing slightly towards the center of the ITCZ. On the northern edge of the ITCZ the distribution shifts to shallower PFs (i.e., heights less than 5 km), with 20–30% of PFs having heights around 3 km at 10° north of the ITCZ center. This is indicative of shallow cumulus in the subtropics; the ITCZ is typically located around 8°N, placing the PFs around 15–20°N. At the southern edge of the ITCZ, the picture is similar to that north of the ITCZ; however, PFs with heights greater than 6 km become more frequent, likely due to the SPCZ, or double ITCZ.

Looking at the anomalies in PF maximum height distribution for wide ITCZs (Figure 2.3b) PFs with heights less than 4 km become less frequent across the domain, with increases in PFs taller than 4 km. Note that some of the large increases occur near the southern boundary of the ITCZ. This suggests that when the ITCZ is wide, shallower convection is less common within the ITCZ

and deep convection is more common, especially near the edges. For narrow ITCZs (Figure 2.3c), PFs with heights below 4 km become much more frequent across the domain, with all PFs with heights greater than 4 km becoming less frequent. This indicates a general shift toward shallower convection when the ITCZ is narrow. Note that most of the bins within the ITCZ are stippled, indicating high confidence in these changes. However, outside of the ITCZ confidence diminishes (no stippling) suggesting a large spread in the anomalies observed.

Focusing now on variability in PF frequency based on PF area, Figure 2.4 shows the joint histograms of PF area and distance from ITCZ center. While the orbital boost of TRMM did cause a reduction in the frequency of very light rain detected by the PR (Liu et al. 2012), RRs greater than 1 mm hr^{-1} are not significantly affected. As the current study neglects very small PFs, many PFs with very low RRs have already been excluded. PFs with RRs less than 1 mm hr^{-1} actually make up a larger percentage of PFs after the boost ($\sim 20\%$) than before the boost ($\sim 18\%$) and so the impact of the orbital boost is small. With PFs that have areas greater than 1,000 km^2 making up a small portion of the total distribution ($\sim 20\%$), small changes in the frequency of larger PFs lead to large percent changes; e.g., if a PF of a given area appears only once in a given month's climatology but twice when the ITCZ is wide, a 100% increase in frequency will be observed.

Figure 2.4b shows that when the ITCZ is wide, PFs with areas greater than $\sim$100 km^2 become more frequent while PFs with areas less than $\sim$100 km^2 become less frequent. Note that because the majority of PFs have areas less than 500 km^2 a small percentage change in frequency can equate to a large number of PFs. From these anomalies a shift from cumulus (small and shallow) to congestus (moderately large and deep) and cumulonimbus (large and deep) features is apparent; however, the increases in the frequency of PFs with areas between 100–1,000 km^2 are not significant, indicating a large amount of variability in the frequency of PFs of this size. In contrast to the wide ITCZs, narrow ITCZs (Figure 2.4c) show a reduction in PFs with areas greater than $\sim$100 km^2, with increases in smaller PFs. This signifies a distinct shift toward smaller PFs in narrow ITCZs. To understand how PFs grow in the wide ITCZ regime, joint histograms of stratiform area fraction are created.

Stratiform area fraction is defined here as the number of PR pixels within a PF that are identified

as stratiform rain by the 2A23 algorithm (Steiner et al. 1995; Awaka 1998) divided by the total number of PR pixels in the feature. Figure 2.5a shows the climatology of joint histograms of stratiform area fraction and distance from ITCZ center. PFs with very low stratiform area (< 5%) account for over 50% of all PFs across the entire ITCZ. This is expected as congestus and cumulus type systems (i.e., convection that has little to no stratiform component) account for nearly all PFs (Figure 2.2). As expected based on the shifts shown in PF area under wide ITCZs (Figure 2.4b), Figure 2.5b shows a shift toward PFs with predominantly stratiform rain when the ITCZ is wide, with Figure 2.5c showing a shift toward predominantly convective rain when narrow. While it is not surprising that the stratiform area increases as PFs get larger, it is not immediately obvious why a wider ITCZ should be associated with larger, more organized individual storms.

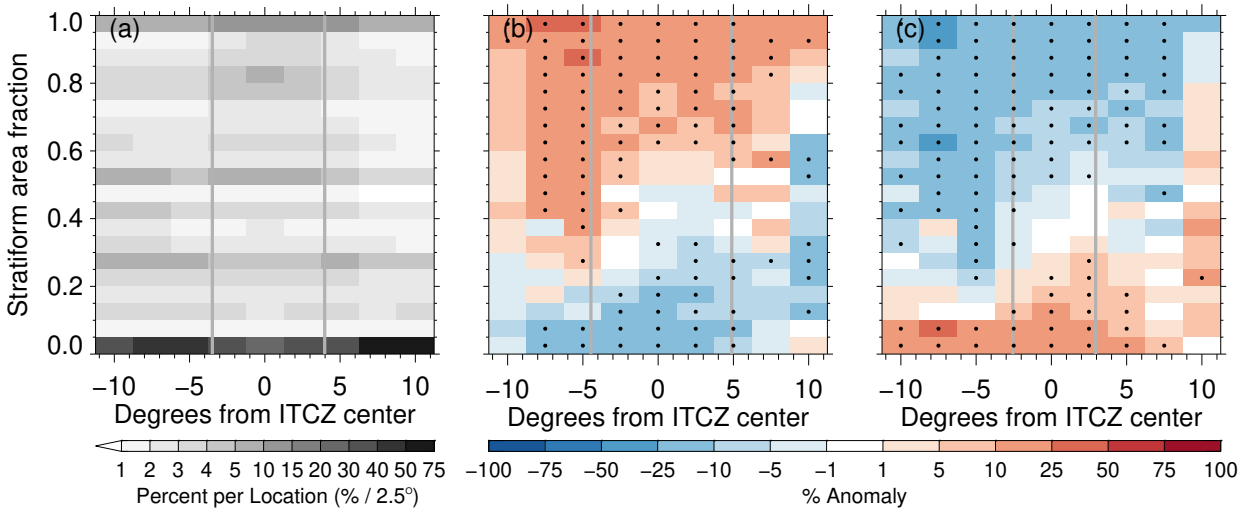

Figure 2.5: As in Figure 2.3, but for PF stratiform area fraction.

2.3.3 Environmental Influences on PF Populations

Recent studies have shown a strong relationship between thermodynamics and precipitation over the ocean, with stratiform rain intensity and area being highly sensitive to water vapor above a critical value (Bretherton et al. 2004; Ahmed and Schumacher 2015). Therefore, it is possible that these different ITCZ regimes correspond to different large-scale thermodynamic variability associated with ENSO or other large-scale drivers. As SST, CWV, and convection are all interconnected (Graham and Barnett 1987; Stephens 1990; Zhang 1993), TMI SST and CWV data are compared across the ITCZ for anomalously wide and narrow months.

All TMI grid boxes that contain at least one PF are used to create zonal median plots of SST and CWV for wide and narrow ITCZs (Figure 2.6). While the differences are not large, both CWV and SST are significantly higher than average (at the 95% level) across the ITCZ region when

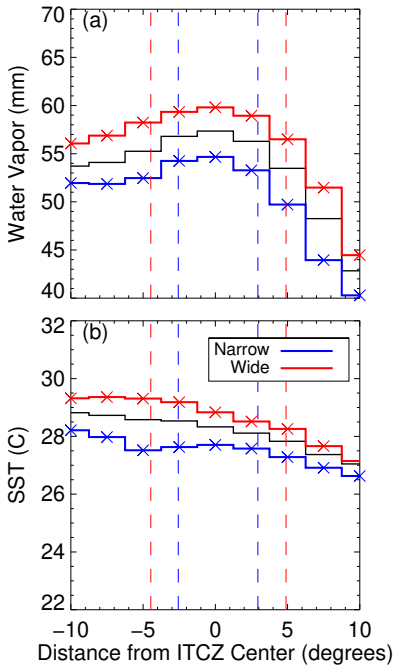

Figure 2.6: Zonal median values of TMI (a) CWV and (b) SST. Blue (red) lines correspond to months below the lower (above the upper) quartile of the width distribution. Xs indicate anomalies that are significantly different from zero at the 95% level. Distances are relative to the center of the ITCZ (positive north) and are in units of degrees. Vertical dashed lines show the mean location of the northern and southern ITCZ boundaries for the narrow and wide regimes.

the ITCZ is wide. Bretherton et al. (2004, their Figure 2a) shows that precipitation rates begin to pickup quickly above 50 mm water vapor path, with rapid increases occurring above 55 mm. While Ahmed and Schumacher (2015) used column saturation fraction, a similar increase in stratiform RR was observed for very moist columns. Ahmed and Schumacher (2015) also noted that RR increases driven by changes in stratiform area were more pronounced than precipitation intensity changes. Thus, the changes in the morphology of PFs under the wide ITCZ regime are likely a result of increased moisture and SST over the tropics, either through increased evaporation locally, or increased moisture convergence from remote sources. It is worth noting that near the northern boundary of the ITCZ CWV decreases rapidly, falling below the 48 mm threshold defining the moist tropics (Mapes et al. 2018) north of the ITCZ. However, at the southern boundary, CWV does not fall below 50 mm, which we attribute to SPCZ influence in the central Pacific region. With ENSO being a major source of both SST and CWV variability in the Pacific (Rasmusson and Carpenter 1982; Trenberth et al. 2005), the relationship between ENSO on ITCZ width is examined.

Using the Multivariate ENSO Index (MEI; Wolter and Timlin 1993, 1998), the influence of ENSO on ITCZ width and PFs is determined by regressing MEI against the ITCZ width anomalies. As the MEI is a two-month index, the value for a single month is computed by averaging the two surrounding 2-month values; i.e., the MEI value for December is the average of the November/December and December/January values. Figure 2.7 indicates a strong relationship between monthly ITCZ width anomalies and ENSO, with a correlation coefficient of 0.63. Defining El Niño (La Niña) events as any month where the MEI is greater than 0.5 (less than -0.5) shows that 41 of the 50 anomalously wide ITCZ months occurred during an El Niño with 36 of the 50 anomalously narrow ITCZ months during a La Niña. However, we note that the patterns shown above also hold when we attempt to mitigate the ENSO influence by excluding ENSO events using the MEI thresholds defined above; general patterns remain similar, although the magnitude and significance of anomalies is greatly reduced.

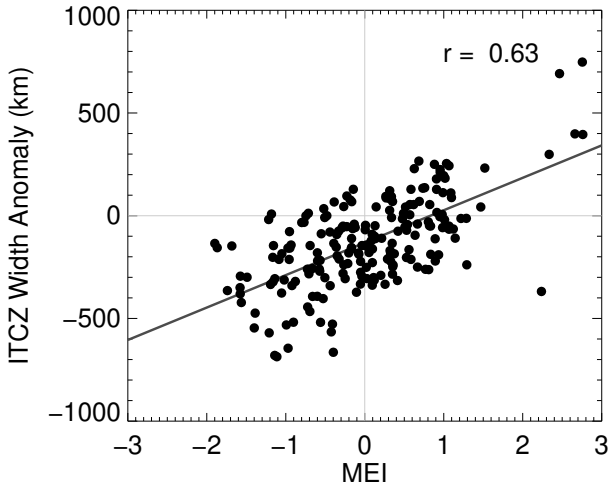

Figure 2.7: Deseasonalized ITCZ width anomalies plotted against MEI for the entire TRMM period of Dec. 1997 – Sep. 2014. Dark gray line is the least-squares linear regression.

2.4 Summary and Discussion

TRMM PFs are used to study changes in the characteristics of convection within the ITCZ in the Pacific Ocean. Using the ITCZ climatology of Wodzicki and Rapp (2016), monthly ITCZ widths are partitioned into anomalously wide and narrow regimes, with the wide (narrow) regime consisting of months where percent anomalies of ITCZ width are above the upper (below the lower) quartile of the ITCZ width distribution.

PFs tend to be larger and deeper when the ITCZ is wide, with large increases in stratiform areas. While PF RRs are lower when the ITCZ is wide, this was determined to be a result of using conditional-average PF RR because PFs with large areas consist of mainly weakly raining stratiform clouds, which act to suppress storm-average RR. The large increases in PF and stratiform area in the wide ITCZ regime may be linked to deep convection changes associated with SST and CWV increases based on a strong correlation between ITCZ width and the MEI and the anomalously high (low) SSTs and CWV in the wide (narrow) ITCZ width regime. This indicates a strong link between ITCZ width and PF characteristics to ENSO and the Walker circulation. While this may seem to be discrepant with model studies of the Walker circulation indicating that convection should be

more intense during the contraction of the deep convection area (e.g., Bretherton and Sobel 2002), this analysis composites convection across the full longitudinal extent of the Pacific ITCZ. When the east-west temperature gradient is strong during La Niña, the ITCZ is narrow and the deeper, more intense convection is confined to a small portion of the averaging domain, so the composite convection is weaker when averaged across the longitudinal ITCZ extent. When the ITCZ is wide during El Niño as the east-west temperature gradient breaks down, the deep convection covers a larger fractional area of the ITCZ averaging domain. Studies of the relation between the strength of the Hadley circulation and the phases of ENSO also lend support to the current study's findings, with many studies (e.g., Oort and Yienger 1996; Stachnik and Schumacher 2011; Nguyen et al. 2013; Hu et al. 2018) showing an anticorrelation between the Hadley circulation and ENSO. This means that under El Niño (La Niña), when the ITCZ is wide (narrow), the Hadley circulation is narrow (wide).

The observed shift from shallow to deep convection between La Niña and El Niño coupled with the modulation of the Walker circulation also provides a mechanism for the large latent and radiative heating perturbations shown in models and observations (Rädel et al. 2016; Stephens et al. 2018). The increase in upper level cloud is the result of the shift from congestus across the bulk of the ITCZ in the narrow regime to larger systems with more widespread stratiform areas in the wide ITCZ regime. The expansion of more organized systems with large stratiform rain regions across the ITCZ during El Niño provide the large positive latent heating anomalies in the warming and moistening regions of the tropics that can feedback on the large-scale circulation.

It is clear from this analysis that variations in ITCZ width and PFs at interseasonal and interannual timescales may not be a good proxy for examining the relationship between convection characteristics and long-term ITCZ width variations due to changes in the Hadley circulation. This is likely due to the differences in the spatial and temporal scales as well as the complex balance of net energy input, atmospheric energy transport, ENSO, and Hadley and Walker circulation influences that drive changes in the Pacific ITCZ at different timescales (Adam et al. 2016).

More work is needed to unravel the connections between the convection distribution and the

large-scale ITCZ state. Further efforts will also be focused on determining a proxy for the changes in convective characteristics observed in the present study that can be applied to long-time series reanalysis and model data sets to determine whether the relationship between the large-scale ITCZ characteristics and the convective systems within the ITCZ hold at longer timescales.

3. LIMITATIONS AND IMPROVEMENTS TO PRECIPITATION FEATURE ANALYSIS

3.1 Discussion of Limitations in Previous Analysis

The analysis of differences in PF characteristics in wide and narrow Pacific ITCZ width regimes in Chapter 2 showed that intense convection, with higher maximum heights and larger stratiform areas, is more frequent when the Pacific ITCZ is wide, while the opposite was found for narrow ITCZs. This indicates that variability in Pacific ITCZ width and associated convection at the short, seasonal to interannual, timescales studied differs from our hypothesized changes based on global, long-term narrowing and intensification of the ITCZ and associated precipitation, both in the Pacific and globally (Zhou et al. 2011; Wodzicki and Rapp 2016; Lau and Kim 2015; Su et al. 2017, 2019). However, the reasons for the differences between timescales are not obvious as there are many sources of variability included in the previous analysis that must be accounted for to determine exactly what drives the observed variability. While not an exhaustive list, a few large sources of Pacific variability have been identified: double ITCZs, seasonal variability, and regional effects. It is worth noting that these three sources of variability are not necessarily independent; double ITCZs tend to occur during boreal spring and are typically found in the eastern Pacific, making them both a seasonal and regional phenomena. However, it is important to consider all these influences as they all play a role in shaping the climate of the Pacific basin.

3.1.1 Double Intertropical Convergence Zones

One of the first major studies of double ITCZs in the eastern Pacific was performed by Zhang (2001) who used monthly mean Climate Prediction Center Merged Analysis of Precipitation (CMAP) data to define ITCZs and double ITCZs and Tropical Atmosphere-Ocean (TAO) mooring array data to study the environment of the two flavors of ITCZ. They defined a double ITCZ as the occurrence of longitudinally elongated bands of precipitation to the north and south of the equator, with a minimum in precipitation at the equator. From the four domains studied (Atlantic, Indian, and western and eastern Pacific Oceans), they only found evidence of double ITCZs in the Pacific and Indian

Oceans. In the eastern Pacific Ocean, double ITCZs can occur from February to May, but usually occur during March and April. In the central Pacific, double ITCZs were much more common, occurring in almost every month of the year; however, due to the subjective identification criteria, it is not clear if the SPCZ was misidentified as a double ITCZ in the central Pacific region.

A more robust, objective analysis of ITCZ variability during boreal summer in the eastern Pacific was performed by Yu and Zhang (2018) wherein an asymmetric index (I_a) and double ITCZ index (I_d) were defined using GPCP RRs in three domains; the northeastern equatorial Pacific, eastern equatorial Pacific, and southeastern equatorial Pacific. Extended Reconstructed Sea Surface Temperature (ERSST) and European Centre for Medium-Range Weather Forecasts (ECMWF) Reanalysis Interim (ERA-Interim) data were also used to determine sources of the observed ITCZ variability. They found that SST gradients across the Pacific Ocean can cause remote changes in wind convergence and precipitation in the eastern Pacific through changes to the surface pressure distribution. From this, it is clear that there are many sources, and a large amount, of variability in the ITCZ in the eastern Pacific during boreal spring.

The work of Huaman and Takahashi (2016) further illustrates the differences between typical and double ITCZs. They performed a thorough analysis of the dynamics of the eastern Pacific ITCZ using data from the TRMM satellite, the Eastern Pacific Investigation of Climate (EPIC) field campaign, and the ERA-Interim. Their Figure 4 (shown below as Figure 3.1) illustrates the very different meridional circulations that appear in September-October and March-April. In boreal fall, there is a single ITCZ north of the equator, with meridional flow closely matching an ideal Hadley circulation; low-level winds flowing into the ITCZ and upper-level winds flowing out of the ITCZ toward the poles. But in boreal spring when double ITCZs are common, the flow becomes much more complex, with overturning circulations on both sides of the equator. Including instances of both of these distinct flavors of ITCZ, which have very different dynamics, in any analysis in the tropical eastern Pacific will introduce large sources of variability that will be difficult to account for. One major way these differences may have impacted the study presented in Chapter 2 is through the apparent competing influence of the northern and southern branches.

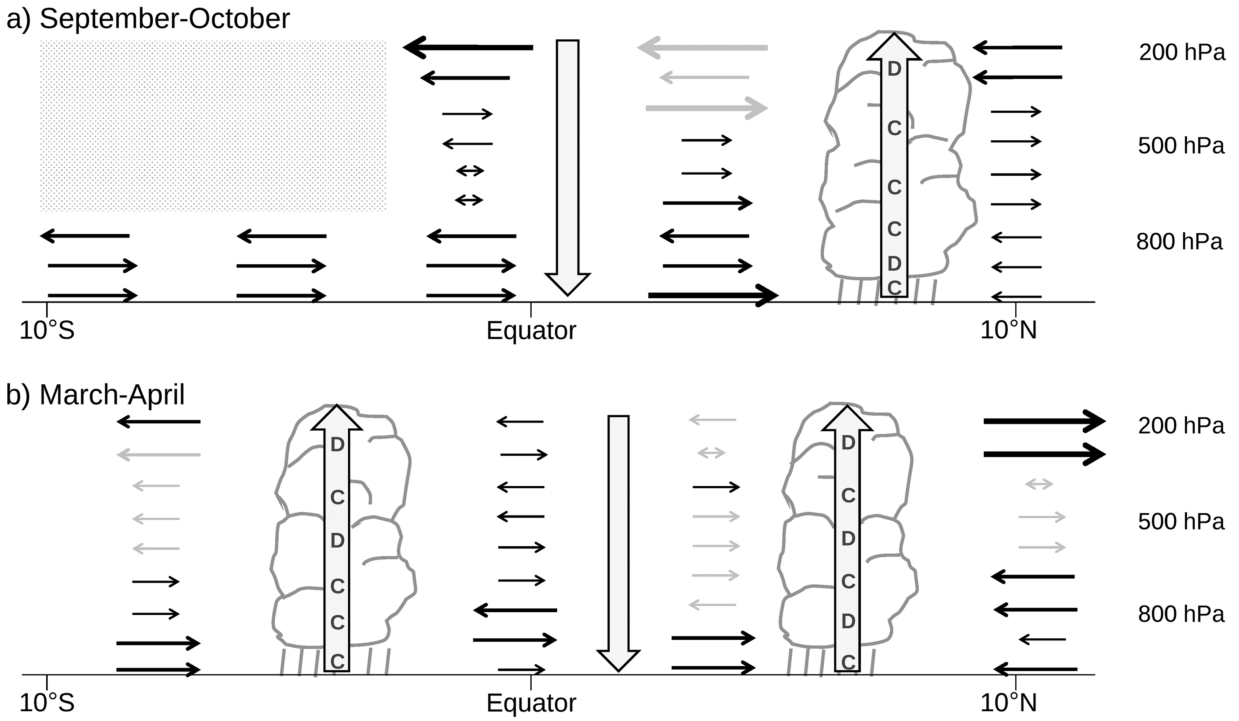

Figure 3.1: Sketch of the climatological meridional circulation in the eastern Pacific (95° – 85°W) in (a) September–October and (b) March–April. Horizontal arrows indicate mean meridional wind (small: 0–2 m/s; medium: 2–6 m/s; large: > 6 m/s; double headed: variable), with gray arrows and shading indicating weak observational constraint. (c and d) Horizontal convergence and divergence, respectively. Reprinted from Huaman and Takahashi (2016, their Figure 4).

Using data from TRMM and RRs from GPCP, Gu et al. (2005) found that the total integrated precipitation across both branches of the eastern Pacific double ITCZ does not vary much year to year; however, the amount of precipitation in each branch can vary greatly. This means that an anomalously strong southern branch can cause the northern branch to be anomalously weak, and vice versa. As our previous study only analyzed the northern branch of the Pacific ITCZ when a double ITCZ was present, large variability in the sorting of boreal spring months into the wide and narrow regimes likely occurred due to the competition between the branches. This source of variability is eliminated here by analyzing only boreal summer months, removing the influence of double ITCZs in the analysis.

3.1.2 Seasonal Variability

Many studies have shown the variability of the ITCZ at the seasonal timescale (e.g., Waliser and Gautier 1993; Bain et al. 2011; Wodzicki and Rapp 2016), which is mainly driven by variability in solar insolation. Figure 3.2, adapted from Wodzicki and Rapp (2016), shows the seasonal cycle of three ITCZ metrics; latitudes of ITCZ center and boundaries, extents of the northern, southern, and full ITCZ, and RRs across the full ITCZ width and near the center of the ITCZ. Figure 3.2a shows that the ITCZ is farthest north in September, indicating a roughly 2 month lag behind the change in solar insolation. The width of the ITCZ also changes with the seasons, going from its narrowest in February (Figure 3.2b, black) to its widest in August-October. These changes have large impacts on the amount and location of rainfall in the tropics (Figure 3.2c) and the dynamics of the Hadley circulation (Webster 2004). Thus, it is important to control for, as best as possible, these seasonal differences. The previous analysis attempted to mitigate the seasonal variations in ITCZ width by using percent anomalies in width when partitioning months into wide and narrow regimes; raw anomalies would have almost certainly ensured that wide months all occurred during boreal fall, with narrow months during boreal spring. While this approach did create a more even sampling of months in the wide and narrow regimes, small changes in ITCZ width during clima-

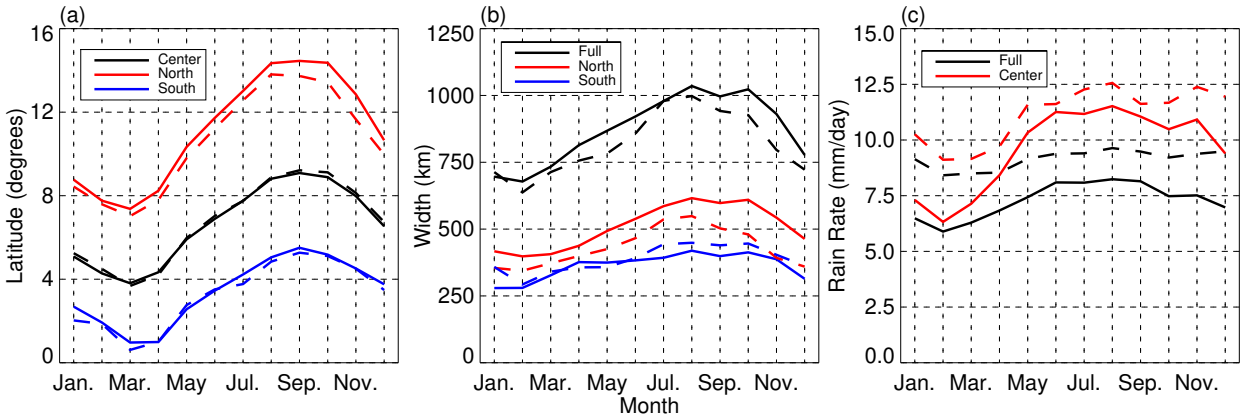

Figure 3.2: Mean annual cycle of ITCZ (a) latitudes, (b) extents, and (c) precipitation rates with colors corresponding to different locations. Solid lines represent GPCP derived values and dashed lines represent TMI derived values. Adapted from Wodzicki and Rapp (2016, their Figure 7).

tologically narrow months can lead to large percent anomalies in width, potentially resulting in an over-sampling of narrow months for the anomalously wide regime and vice versa for the narrow regime. To mitigate the seasonal influence, boreal summer is analyzed separately.

3.1.3 El Niño-Southern Oscillation

A recent study by Henderson et al. (2018) aimed to understand differences between TMI and PR rainfall retrievals in the warm and cool phases of ENSO. They found organized convective systems to be more frequent during El Niño than La Niña. The convective systems were also found to have larger areal and vertical extents with greater RRs in the warm phase. Examination of water vapor data revealed that the atmosphere is 'pre-moistened' during El Niño compared to La Niña, with positive anomalies in water vapor existing before the occurrence of convection. While they suggest the increase in water vapor may be due to increased vertical transport of moisture under El Niño, the exact cause is not clear. However, they do find that these differences in water vapor between ENSO phases leads to deep, isolated convection under La Niña and organized convective systems under El Niño. These differences in water vapor and convection align with the results of Wodzicki and Rapp (2020), providing further evidence of the strong influence of ENSO on convective populations in the Pacific.

It is clear that there are many sources of variability in the Pacific basin impacting both the ITCZ and associated convection. While the above is not an exhaustive list of all possible sources of variability, the largest sources have been highlighted. It is important to remember that these sources of variability are not mutually exclusive. For example, double ITCZs have a distinct seasonality, occurring mainly in boreal spring when the SSTs to the north and south of the equatorial cold-tongue are roughly balanced. The impacts of ENSO are also highly seasonal as warm and cool phases of ENSO are most pronounced from boreal late fall to early spring. As such, it is best to account for all of the sources at the same time rather than try to determine how they impact each other as well as their impact on ITCZ width and associated convection. To do this, analysis is limited to only boreal summer, eliminating the influence of both the seasonal cycle in ITCZ characteristics and

double ITCZs in the eastern Pacific. Limiting analysis to only boreal summer will also remove most of the variability introduced by ENSO; however, to fully account for ENSO, the Multivariate ENSO Index (MEI; Wolter and Timlin 1993, 1998) is used to further restrict analysis to only neutral months during the season of interest. Through controlling these sources of variability, we hope to reach a better understanding of the differences between short and long-term variability in ITCZ width and associated convection.

3.2 Data and Methods

The TRMM PF and ITCZ characteristic databases are used to partition features into wide and narrow ITCZ width regimes using boreal summer (June-August, JJA hereafter) months above (below) the upper (lower) quartile of the width distribution as wide (narrow) months. Only PFs with at least 4 raining pixels are considered as the distribution of features is dominated by these very small objects, which can skew statistics (Liu et al. 2008). Restricting the analysis to this limited time period reduces, or completely eliminates, the sources of variability discussed above. Multiple domains in the Pacific are also tested to better determine regional differences in convection across the ITCZ. These domains include 160°E-160°W, 150°W-110°W, and 160°E-100°W for comparison to previous work. Effects of ENSO are further mitigated by using the MEI (Wolter and Timlin 1993, 1998) to exclude months where the $|\text{MEI}| \geq 0.5$ (Physical Sciences Laboratory 2021; Bain et al. 2011). While such cases are not expected to be frequent during JJA, they are removed to limit the influence of this large source of variability.

Another large difference between this analysis and that of Wodzicki and Rapp (2020) is that PF frequency histograms are scaled by the number of pixels in each PF. This is done to counteract the skew introduced by the plethora of very small PFs in the distribution. For example, Figure 2.3 shows the joint histogram of PF maximum height and distance from ITCZ center. One would expect features with high echo tops to become more frequent when moving from the poles to the center of the ITCZ. However, the figure shows that there is little change in the frequency of PFs with heights > 5 km. This is an artifact of the scaling used in the figure, where the frequencies are scaled to

their locations, which was meant to depict local shifts in convective populations at a given distance from ITCZ center. However, because all clouds become more frequent moving toward the ITCZ, the relative frequency of deep convective PFs does not appear to change. To better represent the impacts of these convective systems, the total number of pixels is now calculated for every joint histogram bin instead of the total number of PFs before normalization to location is performed. This produces much more intuitive histograms (i.e., high topped cloud frequency increases toward ITCZ center) than the previous method with little to no impact on the general patterns in frequency anomalies (see below).

Another difference between the current and previous analysis is the reference to ITCZ center. The original reason for referencing PFs to the center of the ITCZ was to compensate for the seasonal variations in ITCZ location. This allowed comparison of the differences in PF characteristics across the ITCZ between seasons; 5 degrees from ITCZ center is the same distance no matter the location of the ITCZ. However, as the current analysis focuses on just boreal summer, PFs are now simply referenced to latitude. The meridional domain of the analysis is also expanded to 40°S-40°N, allowing for the study of features in the subsidence regions of the overturning circulation that can be affected by changes in the ITCZ through the overturning circulation.

For all joint histograms, deseasonalized values are used to compute mean anomalies in all figures. The statistical significance of anomalies is tested in the same manner as in Wodzicki and Rapp (2020) using a simple bootstrapping method wherein all deseasonalized anomalies are randomly resampled, with replacement, 10,000 times. The sampling size for each resample is roughly one quarter the number of months being analyzed; for JJA excluding ENSO there are 6 months in each resample. The average of each resample is computed, giving 10,000 realizations of the mean anomalies. An anomaly is determined to be significant if it falls in the top or bottom 2.5% of the bootstrapped distribution, giving a two-tailed test at the 95% confidence level. Unless otherwise stated, all time series plots have been low-pass filtered using a 4^{th} order Butterworth filter with a cutoff frequency of one cycle per year. The low-pass filtered data are then deseasonalized removing the mean seasonal cycle to convert to anomalies.

3.3 Results

3.3.1 Precipitation Features across the Tropical Pacific

We again use joint histograms to show differences in the frequency of PFs across the ITCZ width regimes; however, a different scaling is used in this analysis. Figure 3.3 shows the joint histogram with distance from ITCZ center and PF maximum height similar to that of Figure 2.3 (i.e., it contains the same months and is over the same domain of 160°E-100°W), except bins are scaled by PF pixel counts before normalization is performed, and the meridional and height domains are expanded. The new scaling in Figure 3.3a creates a more intuitive picture, with cumulonimbus more frequent within the ITCZ relative to outside of the ITCZ. Cumulus convection appears as the dominant PF type in the subsidence regions, with a transition to congestus moving toward ITCZ center. At the edges of the domain (20°N and 30°S from the center of the ITCZ) congestus type features are most frequent, which is attributed to the Pacific frontal zone north of the ITCZ (Nakamura and Kazmin

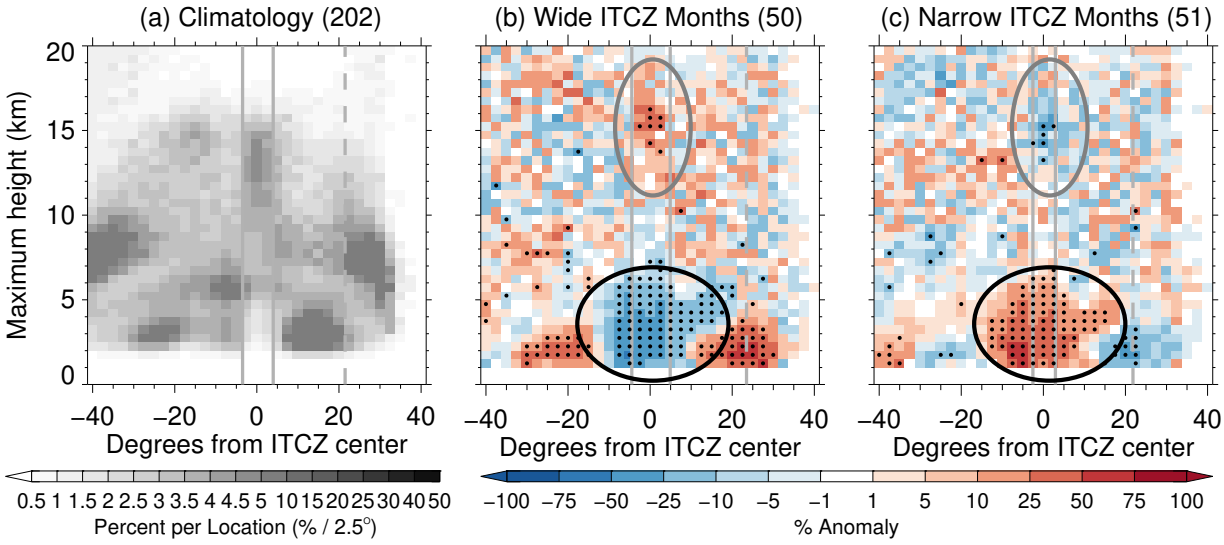

Figure 3.3: Joint histograms of PF maximum height and distance from the center of the ITCZ for (a) climatology, (b) mean of monthly percent anomalies in wide ITCZ months, and (c) mean of monthly percent anomalies in narrow ITCZ months with bin counts scaled by PF pixels. Data spans Dec. 1997 - Sep. 2014 in the domain 160°E-100°W. The vertical solid and dashed lines in all panels represent the location of the ITCZ and Hadley circulation boundaries, respectively, for each data subset. The number of months contained in each plot is also shown in parentheses.

2003) and the SPCZ south of the ITCZ (Vincent 1994). Note that both of these regions are located at roughly 30° latitude in each hemisphere as the ITCZ is, climatologically, located at 8°N (Waliser and Gautier 1993; Wodzicki and Rapp 2016). The general patterns of anomalies for wide and narrow ITCZs in Figures 3.3b and 3.3c match those of Figure 2.3, with cumulonimbus (heights $\geq$ 10 km) more (less) frequent under the wide (narrow) regime within the ITCZ (gray ellipses), while cumulus features (heights $<$ 5 km) are less (more) frequent (black ellipses). However, differences in congestus (heights between 5-10 km) are more variable compared to the old scaling, with no clear increase or decrease in this cloud type in the wide or narrow regimes. While Figure 3.3 is scaled relative to the ITCZ for comparison with Figure 2.3, the rest of this analysis is performed relative to latitude since we are no longer comparing changes across seasons as the ITCZ moves with solar insolation (see Section 3.1.2).

Figure 3.4 shows joint histograms of PF maximum height during JJA with $|\text{MEI}| < 0.5$ between 160°E-100°W. The general distribution of PF pixels (Figure 3.4a) is similar to that of the full data period, with cumulus the dominant type in the subsidence region, a transition to congestus moving toward the ITCZ and at the ITCZ margins, and cumulonimbus dominating within the ITCZ. Note

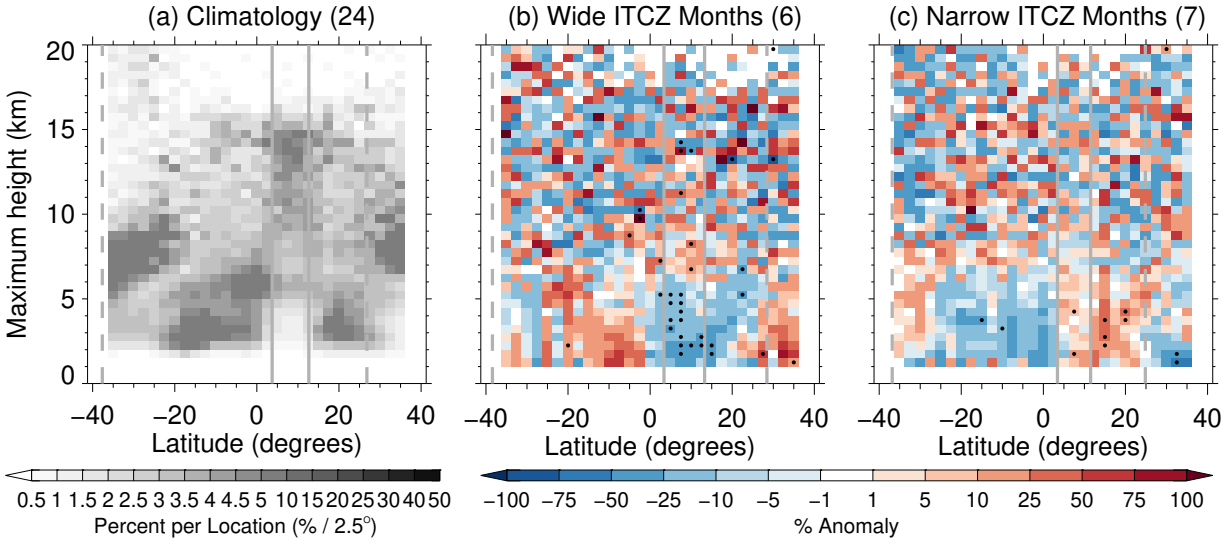

Figure 3.4: As in Figure 3.3, but for JJA, $|\text{MEI}| < 0.5$, and relative to latitude (160°E-100°W).

that large pixel frequencies at the boundaries of the domain (40°N and 40°S) are a result of the TRMM orbit; the satellite samples these latitudes more frequently than others. Looking at the wide (Figure 3.4b) and narrow (Figure 3.4c) regimes, almost no discernible pattern appears in deep convection, the result of very few samples; only 6 wide months and 7 narrow months. However, the differences in the more frequent cumulus-type convection do appear, with fewer (more) cumulus within the ITCZ (subsidence region) under the wide regime and more (less) in the narrow.

A quick look at PF maximum height in the eastern Pacific (EPAC; Figure 3.5) shows similar patterns to the full Pacific, but with added noise due to a further reduction in sample size due to the small zonal domain. The sparse sampling in the plot is apparent as the bootstrapping begins to fail, with regions that show, essentially, zero percent anomalies identified as significant differences.

Stratiform area fraction within the full Pacific domain (Figure 3.6a) shows PFs with high stratiform area fractions are fairly uniformly distributed across the tropics, with fractions between 0.4-0.7 present across the entire Hadley circulation. Within the ITCZ, stratiform area fractions greater than 0.7 occur frequently, with fractions of 0.5-0.7 being the most frequent. Differences in stratiform area fraction in the wide regime (Figure 3.6b) further support shifts in cumulus convection indicated by the analysis of PF maximum height, with low area fraction PFs (<0.3) less (more)

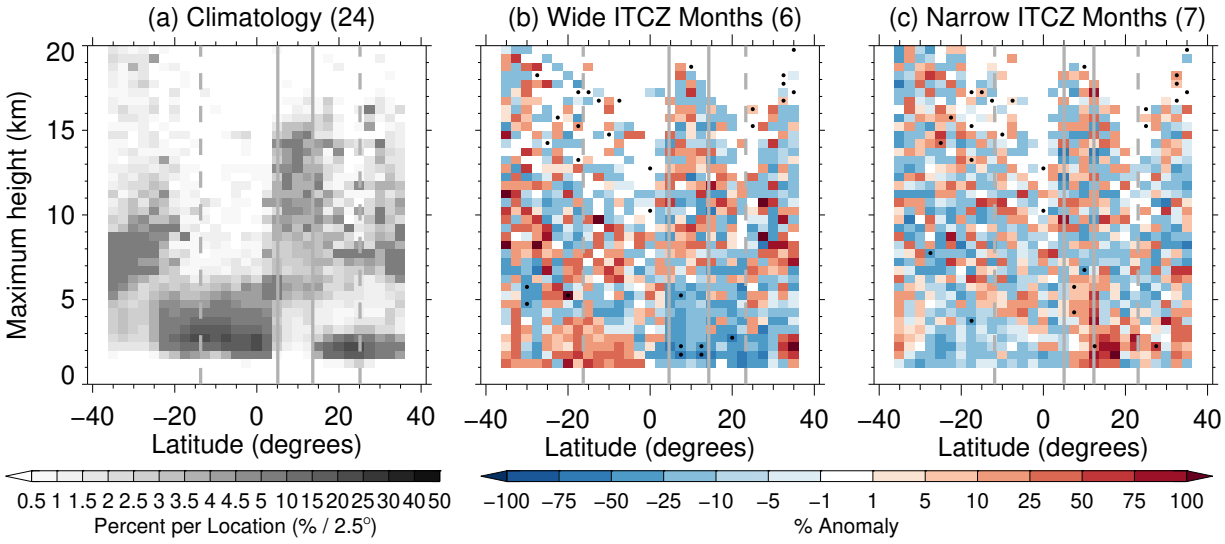

Figure 3.5: As in Figure 3.4, but for 110°-150°W.

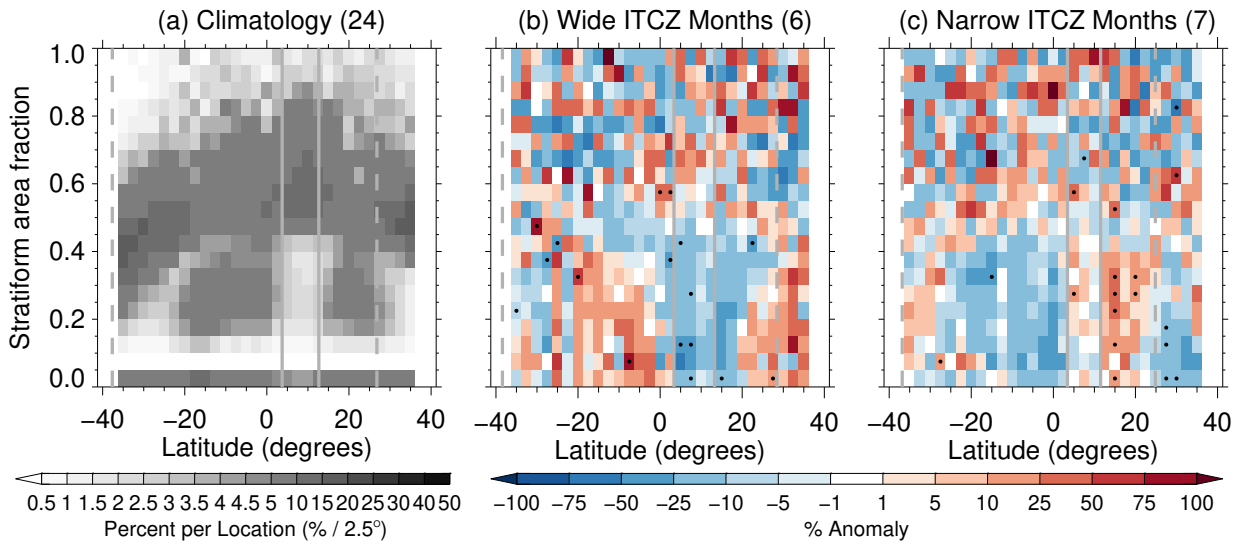

Figure 3.6: As in Figure 3.4, but for stratiform area fraction (160°E-100°W).

frequent within the ITCZ (subsidence region). Congestus and cumulonimbus regimes are harder to delineate in the stratiform area fraction framework, so they are discussed together. In the subsidence regions of the wide regime, reductions in the frequency of high stratiform area fractions ($>$0.6) appear to be the dominant signal, but the large variability makes identification of a clear signal impossible. A reduction in the frequency of congestus and cumulonimbus in the subsidence regimes, however, is expected based on the increased strength of the overturning circulation in the region. Generally, patterns opposite of the wide regime exist in the narrow regime (Figure 3.6c), with cumulus type clouds less frequent in the subsidence regions and, albeit slightly, more frequent within the ITCZ. While patterns in congestus and cumulonimbus PFs are noisy, there appears to be a pattern of increased frequency in the subsidence region in the narrow regime, likely the result of weaker overturning in the regime, allowing the development of systems with larger stratiform areas.

In the EPAC (Figure 3.7a), PFs with stratiform area fractions greater than 0.6 are infrequent in the Southern Hemisphere subsidence region, likely due to the lack of any SPCZ influence in the region. Patterns are again similar to those of the larger Pacific domain in both the wide and narrow regimes, with cumulus (area fractions less than 0.4) less (more) frequent within the ITCZ

(subsidence region) in the wide regime and more (less) in the narrow.

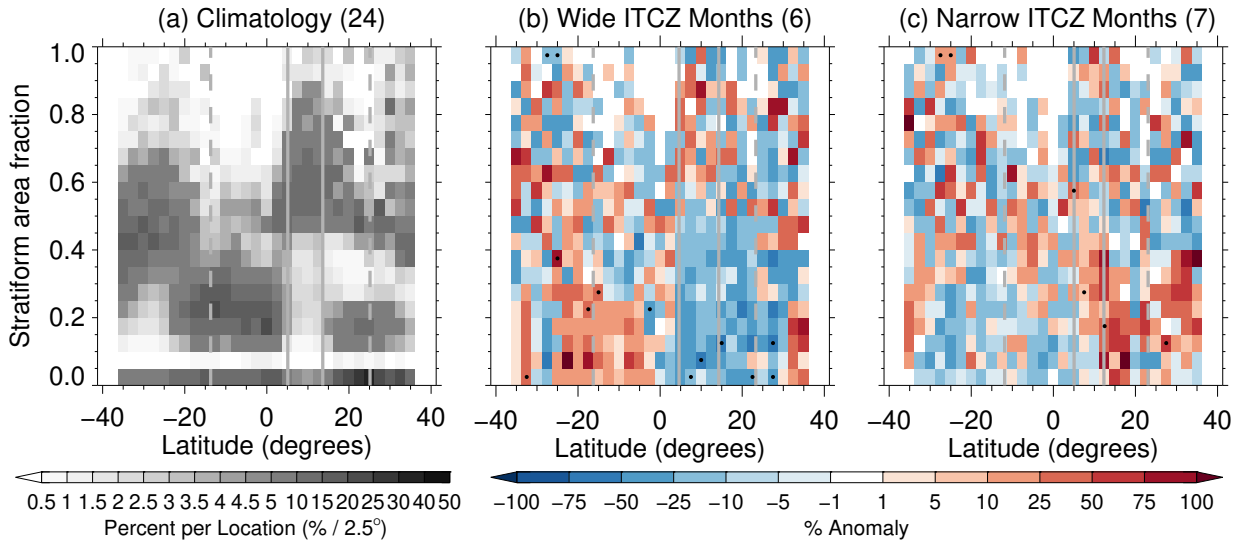

Figure 3.7: As in Figure 3.6, but for 110°-150°W.

After accounting for double ITCZ, seasonal cycle, and ENSO variability, results show patterns similar to those of the previous analysis in Wodzicki and Rapp (2020). A comparison of the Hadley circulation characteristics between the two regimes is also performed for a more complete understanding of the forcings that may be leading to the observed variations. As mentioned above, under the wide regime there is evidence of increased overturning strength, as deep convection within the ITCZ becomes more frequent (increased ascent), while deep convection outside of the ITCZ, namely in the subsidence regions, becomes less frequent (increased descent).

3.3.2 Hadley Circulation Variability

The Hadley circulation is a thermally direct circulation responsible for transporting energy from the tropics toward the mid latitudes. The circulation is driven by convection associated with the ITCZ, with the ascending branch near the equator and subsidence branches extending to roughly 30° latitude in both hemispheres (Webster 2004). As changes in convection within the ITCZ can lead to changes in the overturning circulation through adjustments to the latent heating profile (Hack

et al. 1989; Hou and Lindzen 1992; Dodd and James 1997), it is important to understand how the Hadley circulation varies with the variations in PFs observed in the previous analyzes. An analysis of the impact of ENSO on the Hadley circulation is also warranted as ENSO was determined to be responsible for much of the differences observed between the wide and narrow ITCZ width regimes in Chapter 2 (Wodzicki and Rapp 2020).

The Hadley circulation is characterized through the zonal-mean meridional stream function (Ψ; Oort and Yienger 1996; Lu et al. 2007; Hu and Fu 2007; Stachnik and Schumacher 2011), which is

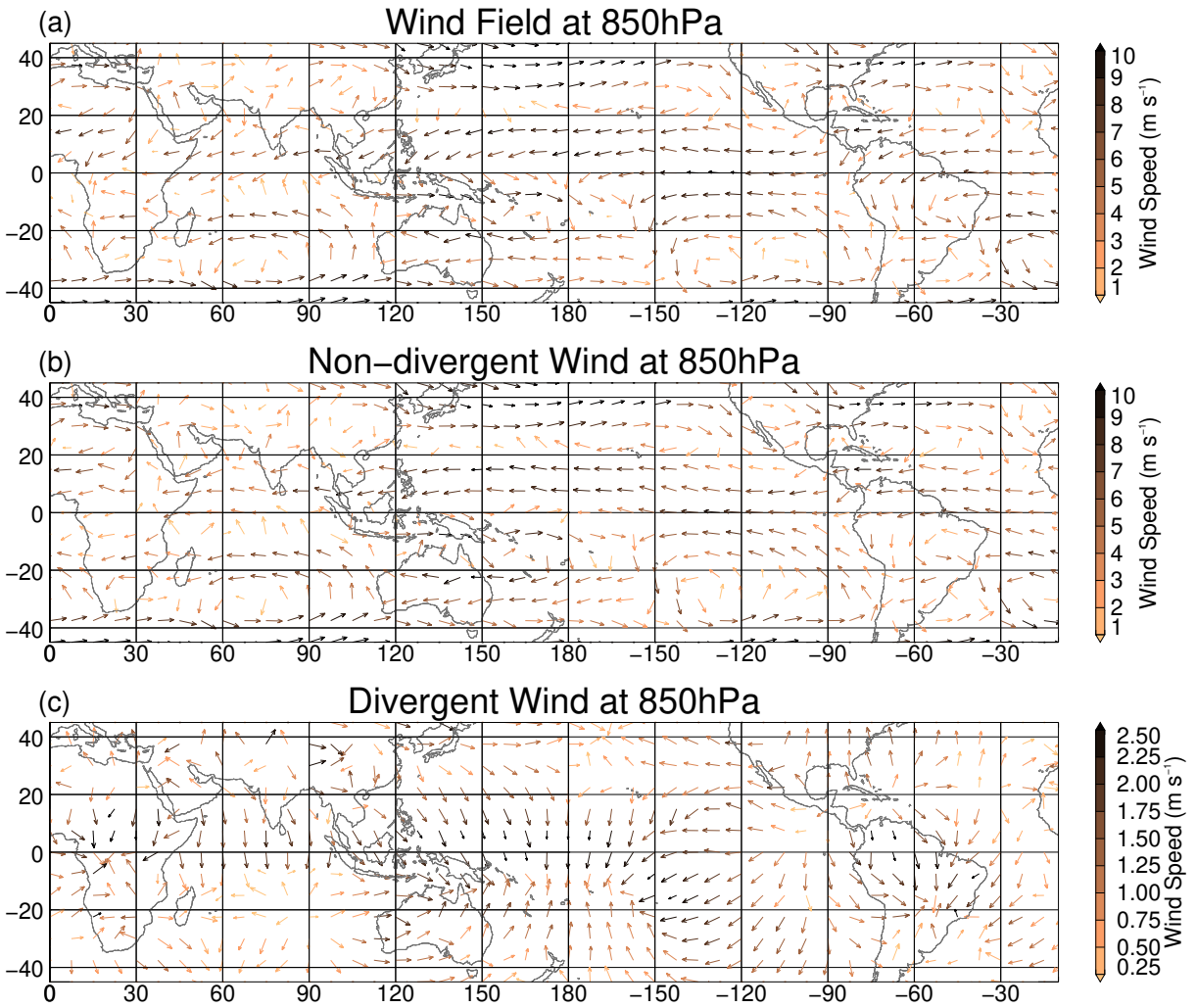

Figure 3.8: Example of Helmholtz decomposition of ERA-Interim 850 hPa monthly mean winds for Jan. 1979 with (a) mean wind field, (b) non-divergent component of the wind, and (c) divergent component of the wind.

computed from ERA-Interim data, using the methods of Stachnik and Schumacher (2011). However, it is not possible to directly apply these methods of characterization to the smaller longitudinal domains of the current study because the assumption of mass continuity at the global scale does not hold for regional domains. Thus, the approach of Zhang and Wang (2013) is used, wherein a Helmholtz decomposition is performed on the horizontal wind to obtain the divergent and non-divergent $u-$ and $v-$components of the wind. From these, it is possible to study vertical motion from the divergent wind and the curl, or rotation, from the non-divergent wind. The meridional component of the divergent wind is used to study the Hadley circulation; the zonal component can be used to study the Walker circulation. The boundary identification method of Stachnik and Schumacher (2011) is used to determine the poleward edges of the Hadley circulation, along with other metrics such as the strength of the overturning. Decomposition of the wind field was done using the windspharm Python package (Dawson 2016) and an example of the decomposition is shown in Figure 3.8.

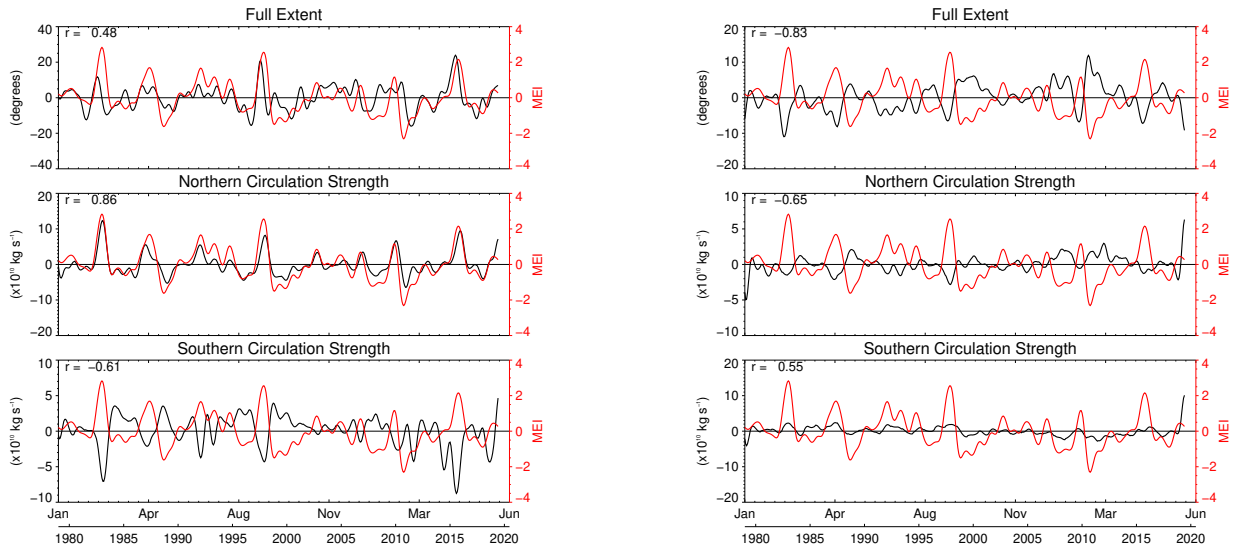

(a) Hadley cell characteristics for Pacific Basin (160°E-100°W)

(b) Hadley cell characteristics for rest of the world (100°W-160°E)

Figure 3.9: Time series of (top) Hadley cell extent, (middle) northern branch circulation strength, and (bottom) southern branch circulation strength, with MEI plotted in red, for two longitudinal domains spanning the (left) Pacific basin and (right) reset of the globe. The correlation coefficient between each variable and the MEI are shown in the top-left of each panel.

With the results from Wodzicki and Rapp (2020) indicating that ENSO is the driving force behind the differences in PF variability in the Pacific ITCZ width regimes and the present analysis' aims to study cloud populations across the Hadley circulation, we first look at the relationship between ENSO and the Hadley circulation. Figure 3.9a shows two metrics (extent and circulation strength) for the Hadley circulation in the Pacific along with the MEI. The strength of the circulation in the northern (southern) hemisphere is the maximum (minimum) value of Ψ in the northern (southern) hemisphere, with the latitude of of this value being the center of the circulation. To define the extent of the circulation, the distance between the subtropical edges of the circulation is computed where edges are the first poleward latitudes of the circulation centers where the 700-400 hPa averaged value of Ψ equals zero in each hemisphere (Stachnik and Schumacher 2011). From the top panel of Figure 3.9a it is clear that the Pacific Hadley circulation expands during El Niño and contracts during La Niña (r = 0.48). There is an even stronger correlation between MEI and the strength of the northern (middle) and southern (bottom) circulations (r = 0.86 and r = -0.61, respectively). This finding is slightly at odds with the results of Stachnik and Schumacher (2011), which showed a narrowing and intensification of the circulation under El Niño. However, their study was performed using the global mean circulation, not a regional domain. Thus, the same Hadley

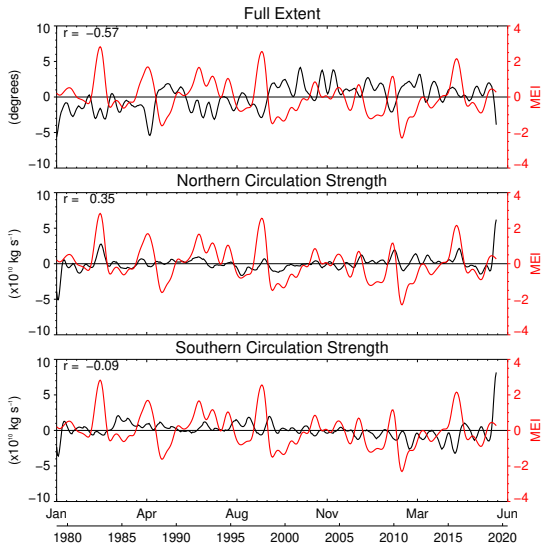

Figure 3.10: As in Figure 3.9, but for the entire globe.

circulation characteristics for the counter-part of the Pacific basin (i.e., the rest of the globe) are shown in Figure 3.9b. Outside of the Pacific, the circulation undergoes the exact opposite response to ENSO, with the circulation extent and strength negatively correlated with MEI; i.e., contracting and weakening during El Niño. It is worth noting that when looking at the circulation characteristics for the entire globe (Figure 3.10), results are similar to that of Stachnik and Schumacher (2011) with a strengthening and contracting of the global circulation under El Niño.

To obtain a clearer picture of exactly what signals may be driving Hadley cell variability in the Pacific, and around the world, coherency spectra between the MEI and Hadley cell characteristics are computed. The coherency spectra are computed using Welch's method, with Hann windowed

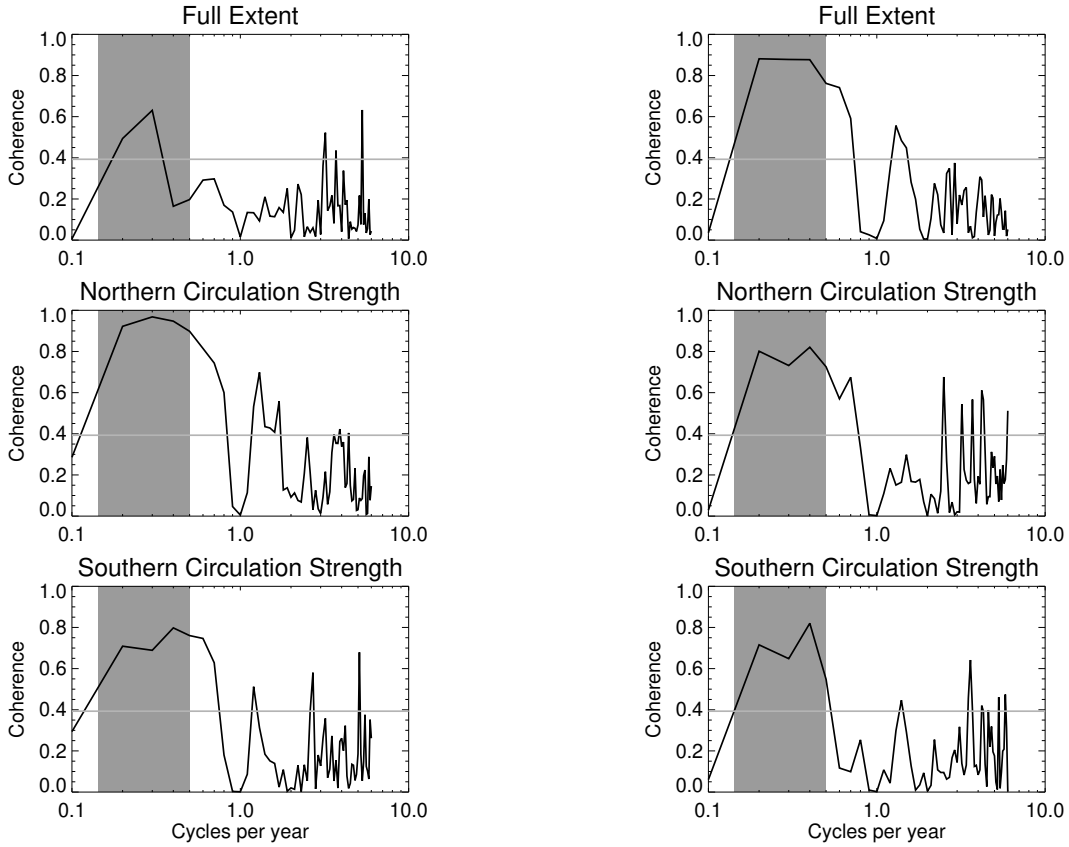

(a) Pacific Basin (160°E-100°W)

(b) Reset of world (100°W-160°E)

Figure 3.11: As in Figure 3.9, but for coherence of MEI and Hadley circulation characteristics. The dark-gray box highlights the period range of ENSO (2-7 years per cycle), with the light-gray horizontal line showing the 95% confidence level for coherence.

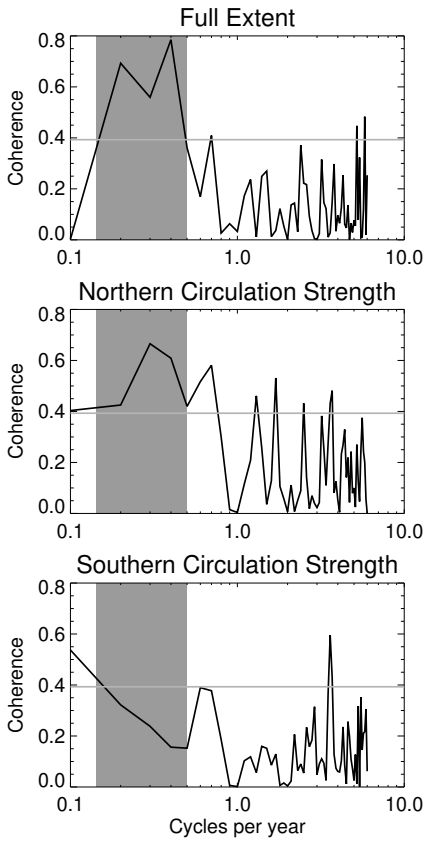

Figure 3.12: As in Figure 3.11, but for the entire globe.

segments of 120 months (10 years) with 50% overlap. Data are demeaned and detrended before computing coherence; there is no low-pass filtering or deseasonalization performed. Figure 3.11a shows the coherence between MEI and Hadley cell characteristics in the Pacific basin (160°E–100°W). The coherence spectra for the complementary portion of the globe (100°W–160°E) and for the entire globe are shown in Figures 3.11b and 3.12, respectively. The gray box highlights the typical range of ENSO frequency (2-7 years per cycle) and the light-gray horizontal line signifies the 95% confidence level. It is clear that the low frequency variability in the MEI, especially at ENSO timescales, is significantly correlated with changes in Hadley circulation width and strength in both domains of interest. As the MEI is designed to capture the ENSO signal, the contribution of other forcings to the index should be minimal. This fact provides a high degree of confidence that ENSO and variability in the Hadley circulation are very closely linked, with an expansion

and strengthening of the circulation in the Pacific basin and a contraction and weakening of the circulation around the rest of the globe during El Niño. These competing factors balance at the global scale resulting in a strengthening and narrowing during El Niño. This supports the decision to exclude warm and cool ENSO phases and focus on the boreal summer months in the Pacific analysis as a means to better understand the short-term, interseasonal to interannual, variability of cloud populations. More insight into changes in the Hadley circulation, such as the exact regions of strengthening and expansion in each hemisphere, can be gleaned from the zonal-mean mass stream function over our Pacific domains.

We plot the zonal-mean mass stream function for only JJA where the $|\text{MEI}| < 0.5$ during the PF data period (Dec. 1997 – Sep. 2014). Figure 3.13a shows the climatological mass stream function for this period with positive values indicating counter-clockwise rotation. The $\Psi = 0$ contour is highlighted in thick-black, with ITCZ center and boundaries in solid and dashed gray, respectively. It is clear that the northern branch of the circulation is much weaker than the southern

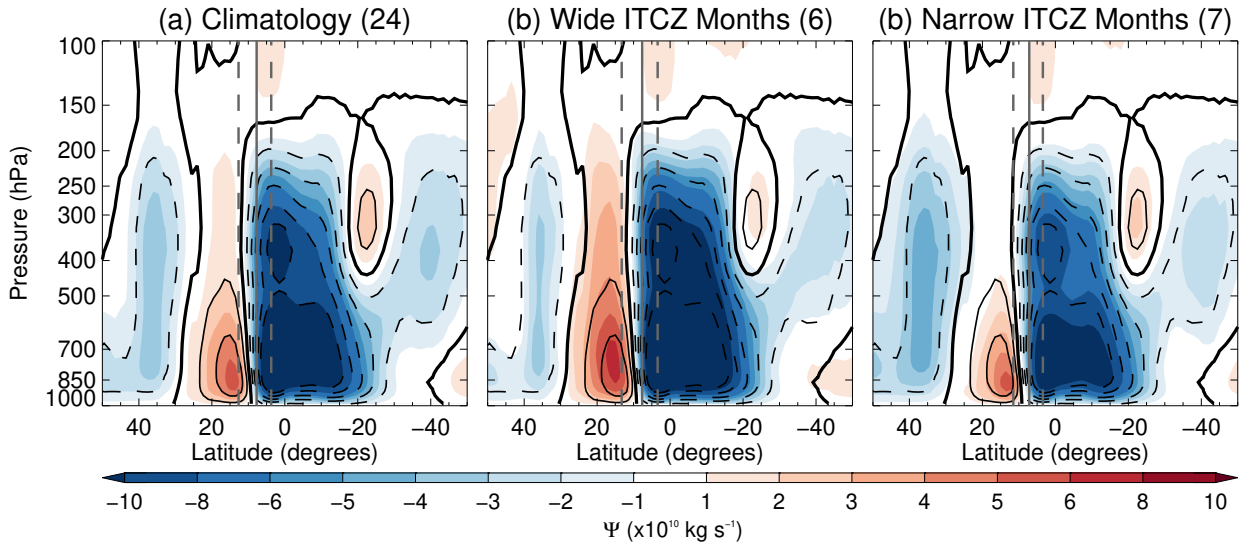

Figure 3.13: Zonal-mean mass stream function for 160°E-100°W during JJA with $|\text{MEI}| < 0.5$ for (a) climatology, (b) wide ITCZ, and (c) narrow ITCZ. Contours are solid (dashed) for positive (negative) values of Ψ, with thick solid contours highlighting values where $\Psi = 0$. Contour interval is 2×10^{10} kg s^{-1}. Vertical gray lines show the (solid) ITCZ center and (dashed) ITCZ boundaries for the respective periods. The number of months contained in each plot is shown in the title in parentheses. Note that positive values of Ψ signify counter-clockwise rotation.

branch during JJA, which is to be expected as the summer hemisphere typically has the weaker branch of the circulation (Tucker 1959; Lorenz 1967; Oort and Rasmusson 1970; Webster 2004). The ascent region of the circulation is near 8°N, matching the ITCZ identification very well, with the terminus of the northern (southern) branch of the circulation at roughly 30°N (35°S), making the northern branch of the circulation much narrower than the southern branch.

Figures 3.13b and 3.13c show the zonal-mean mass stream function in the wide and narrow ITCZ width regimes, respectively. Note that the contours on these plots are the climatological contours, giving a reference for differences in the circulation between the regimes. Somewhat surprisingly, both the northern and southern branches of the circulation are stronger in the wide regime (relative to climatology). The opposite is true for the narrow regime, with both branches weaker in the narrow regime. As warm and cool ENSO events are excluded from these figures, and the other sources of variability discussed above have been mitigated as much as possible, these differences between the width regimes still indicate a Walker circulation influence on convection due to variability in SSTs across the Pacific Ocean.

In the EPAC (110°-150°W), Figure 3.14a shows that the northern and southern branches of the circulation are narrower, with terminus of roughly 25°N and 15°S, respectively. While not a perfect proxy for Hadley circulation extent, this narrowing of the circulation is similar to the findings of Martin et al. (2020), who found the tropics to be much narrower in the EPAC using a tropopause break method to identify the tropics. The Ferrel cell is also visible in the Southern Hemisphere in this region. We again see an intensification of the overturning circulation in the wide ITCZ regime (Figure 3.14b) with a weakening in the narrow regime (Figure 3.14c).

The lack of a clear Ferrel cell in the larger Pacific domain is likely due to SPCZ influence, which would act to expand the Hadley circulation through its broad area of ascent. As a check for SPCZ influence, the circulation is plotted over the central Pacific (CPAC; 160°E-160°W) in Figure 3.15. The southern branch of the circulation in the CPAC is very expansive, extending beyond 50°S, providing clear evidence of SPCZ influence as there is no other significant feature in this region that could cause such an expansive area of ascent and associated descent. The same intensification

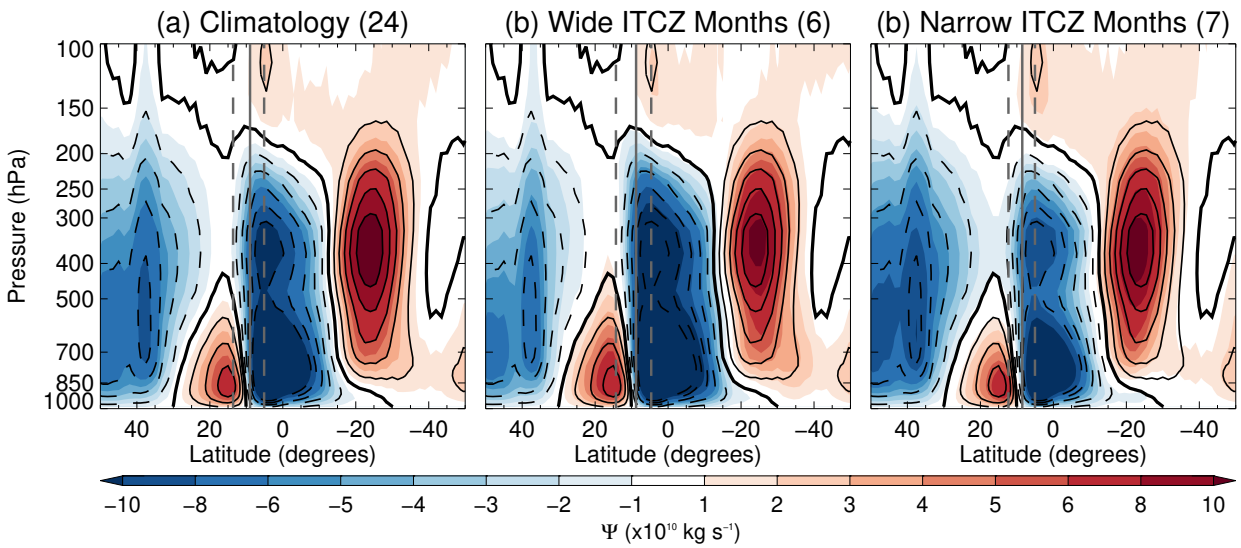

Figure 3.14: As in Figure 3.13, but for 110°-150°W.

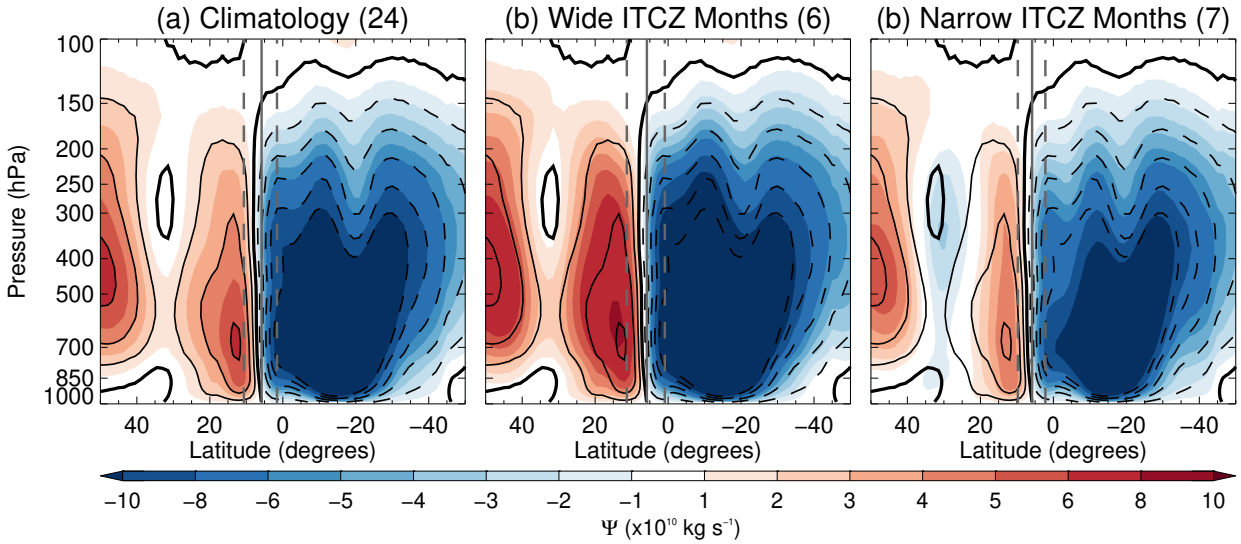

Figure 3.15: As in Figure 3.13, but for 160°E-160°W.

and weakening of the circulation in the wide and narrow regimes found in the full Pacific and EPAC domains are found in Figures 3.15b and 3.15c, respectively.

With consistent signals of intensification (weakening) of the overturning circulation in the wide (narrow) ITCZ regime across various domains in the Pacific basin during JJA in the absence of ENSO influence, it is clear that variability at these short, interseasonal to interannual, timescales in

the Pacific basin do not match expected global signals of long-term changes in the Hadley cell with increasing temperature. As partitioning the mass stream function into ITCZ width regimes shows a Walker circulation influence even when adjusting for ENSO, the internal variability of the Pacific system seems to be that of a wide (narrow) ITCZ simply increases (decrease) the circulation strength through, to first order, a wider area of ascent. This increased circulation strength in the wide regime is accompanied by a reduction in convection in the subtropics (shown above) as the increased subsidence acts to suppress convection. The opposite response is shown in the narrow regime, wherein weaker subsidence seems to allow for more convection. Figure 3.16 further illustrates the Walker circulation influence, showing the difference between ERA-Interim vertical pressure velocity at 500 hPa (ω_{500}) in the wide and narrow ITCZ regimes for the same time period and a similar domain to that of Figure 3.13. Negative values across much of the Pacific (150°E-120°W) mean the ascent in the wide ITCZ regime is greater than the narrow, while in the western Pacific warm pool (120°E-150°E), ascent is greater in the narrow ITCZ regime than in the wide. This indicates that the Walker circulation is relatively weak (strong) in the wide (narrow) ITCZ width regime.

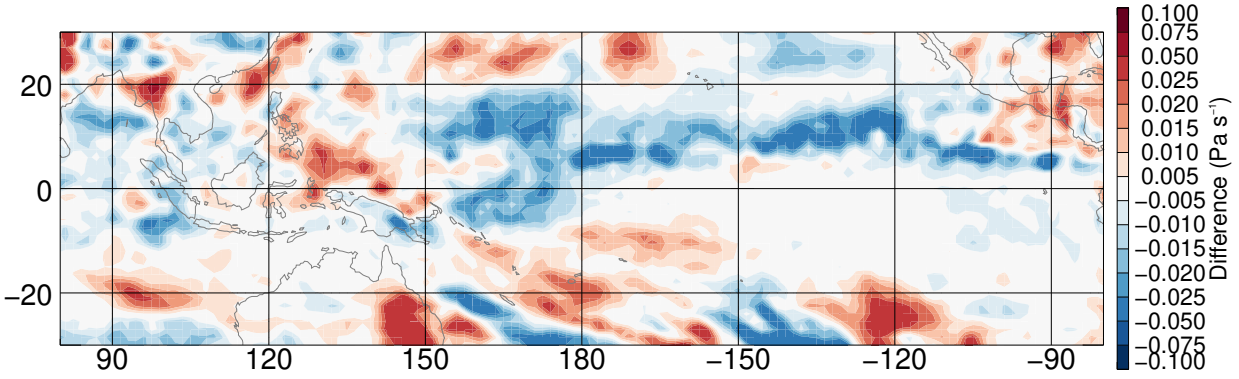

Figure 3.16: Difference in ERA-Interim ω_{500} during JJA with $|\text{MEI}| < 0.5$ over the period Dec. 1997 - Aug. 2014 between wide and narrow ITCZ months (wide-narrow).

3.4 Discussion and Future Work

Recent work by Wodzicki and Rapp (2020) showed that the variability of Pacific ITCZ width and associated convection at short, interseasonal to interannual, timescales is influenced mainly by ENSO. They concluded that regional wide and narrow ITCZ regimes in the Pacific are not representative of long-term observed changes in the ITCZ, as tall PFs with large areal extents and high stratiform rain fractions were more frequent in the wide ITCZ regime and less frequent in the narrow. These differences are opposite of those expected, with observational (e.g., Zhou et al. 2011; Wodzicki and Rapp 2016) and climate model (e.g., Lau and Kim 2015; Su et al. 2017) studies indicating a narrowing of the ITCZ with an intensification of associated convection. Through a better understanding of the relationship between ITCZ width, tropical convection, and the Hadley circulation in the Pacific Ocean at short timescales, the link between Pacific ITCZ width regimes and convection populations in the current climate is better understood.

As in Chapter 2, PF data were partitioned into wide and narrow ITCZ width regimes using the upper (lower) quartiles of the width distribution. Joint histograms of PF maximum height and stratiform area fraction were used to determine differences in raining cloud populations between wide and narrow ITCZs. These histograms are similar to those shown in Wodzicki and Rapp (2020); however, PF pixel counts are used instead of raw PF counts to give a more natural look to histograms. While sample sizes in the width regimes were very small, in general, cumulus convection (heights < 5 km) was less (more) frequent within the ITCZ under the wide (narrow) width regime. The inverse is true in the subsidence regions, with cumulus convection more (less) frequent under the wide (narrow) width regime. Differences in congestus (heights 5–10 km) and cumulonimbus (heights > 10 km) were highly variable across the tropics, with some indication of deep convection being more (less) frequent within the ITCZ in the wide (narrow) width regime. Stratiform area fraction provided support to the differences shown in maximum height, with cumulus convection (i.e., low stratiform area fractions) being less (more) frequent within the ITCZ in the wide (narrow) width regime. The inverse is again true in the subsidence regions, with cumulus convection more (less) frequent in the wide (narrow) width regime. Variability in deep convection (i.e., high strati-

form area fraction) was, again, unclear due mainly to the small sample size. To better understand large scale influences on convection in the tropical Pacific, Hadley circulation characteristics were also examined to determine how they vary with ITCZ width.

As the Hadley circulation and ITCZ are very closely linked, and ENSO is the largest source of variability in the Pacific basin at interannual timescales, time series and coherence analyzes were performed between the MEI and Hadley circulation characteristics. Strong, statistically significant, correlations between the Hadley circulation characteristics and ENSO in the Pacific basin were found, with warm (cool) phases leading to increased (decreased) circulation strength and a wider (narrower) circulation. To mitigate variability introduced by ENSO, along with others sources of variability such as double ITCZs and seasonal variability, only boreal summer months where $|\text{MEI}| < 0.5$ were used. Differences in the mass stream function between wide and narrow ITCZ width regimes for various regions of the Pacific showed a consistent ENSO-like response even with the restrictions described above. With an apparent relation between ITCZ width and overturning strength, variations in PFs were analyzed to understand how convection varies with the changes in ITCZ width and circulation strength.

From the analysis of the Pacific Hadley circulation and its relationship to ENSO and the Pacific ITCZ, it is very clear that the circulation is tightly linked to the Walker circulation and SST. Under El Niño (ENSO warm phase), anomalously warm SSTs are present across the central and eastern Pacific, leading to a decrease in the strength of the Walker circulation. The results from Chapter 2 show that this leads to increased ITCZ width, CWV, and frequency of deep, organized convection. Henderson et al. (2018) found similar changes in CWV and convection with El Niño, wherein SST anomalies drive CWV anomalies, aiding in the formation of organized convective systems within the ITCZ region. Through a study of ENSO's impact on the hydrologic cycle in the Pacific using observational and model data, Stephens et al. (2018) found a series of feedbacks that act to enhance, and ultimately reverse the impacts of SST anomalies associated with El Niño. The initial impacts match those of Henderson et al. (2018), with increases in moisture and convection, as shown by increased precipitation and latent heating in the ITCZ. These changes, through a reduction in solar

heating at the surface due to increased cloudiness, ultimately lead to the break down of the SST anomalies that initiated the increase in convection. The combination of all these factors clearly lead to an increase in the strength of the Pacific Hadley circulation in response to El Niño. The opposite is true for La Niña, with anomalously cool SSTs leading to an increase in Walker circulation strength acting to limit development of strong convection across the broad Pacific domain; decreases in CWV likely also inhibit convection. As a similar, albeit weaker, signal is found when controlling for ENSO and seasonal variations, the general impact of Walker circulation and SST variability persists at short timescales. Changes in the analysis region across the Pacific did not show much difference in the impact of Walker circulation and SST variability between the wide and narrow ITCZ width regimes. The combination of all these factors helps explain why convection in the Pacific does not vary with Pacific ITCZ width at short timescales as would be expected from long-term trends of narrowing and intensification.

Previous studies that showed a narrowing and intensification of the ITCZ analyzed changes at the global scale, which, as shown above and discussed by Stephens et al. (2018), do not necessarily reflect regional changes. We have shown competing regional responses in the Hadley circulation to ENSO forcing, with the circulation in the Pacific strengthening and widening under El Niño while the circulation outside of the Pacific weakens and narrows. As the global circulation response is a combination of these regional responses, and is consistent with studies of long-term changes in the Hadley circulation, a global analysis of convection and the ITCZ may be more consistent with our hypothesis. Another possible reason for the differences between timescales is that previous studies were focused on narrowing and intensification in response to global warming, especially in climate model studies such as Lau and Kim (2015) and Su et al. (2017). While the above work intended to use ITCZ width to gain a general understanding of the global changes analyzed in previous studies, this metric is insufficient. The failure of this metric is, perhaps, due to Pacific ITCZ width being a poor representation of global mean temperature; i.e., the ITCZ is not necessarily wide when global temperatures are anomalously warm.

To test this, global, area-weighted, means of SST are computed using version 1.1 Hadley Cen-

tre Sea Ice and Sea Surface Temperature (HadISST; Rayner et al. 2003) data and the probability density functions (PDFs) of global SST are plotted for the wide and narrow Pacific ITCZ width regimes over both the long-term (Jan. 1979-Aug. 2019) ERA-Interim and short-term (Dec. 1997-Sep. 2014) TRMM period. Figure 3.17a shows little difference in global mean SST between the Pacific wide and narrow ITCZs giving a clue to the differences between changes at the different timescales. For long-term studies, the main driver of ITCZ width changes is changes in SST, which are also related to phenomena such as the *upped-ante mechanism* (Chou and Neelin 2004), *deep-tropics squeeze* (Lau and Kim 2015), and *tightening of Hadley ascent* (Su et al. 2017) as the global atmosphere undergoes changes in the distribution of moisture. This warrants future analysis looking at global changes in convection and cloud populations using an ascent extent metric that more closely follows global SST. One such metric is ascent area fraction introduced by Su et al. (2019), wherein climate model grid boxes with $\omega_{500} < 0.0\,\mathrm{Pa\,s^{-1}}$ are taken as ascent, with the fractional area of ascent computed relative to all grid boxes between 30°S-30°N. This metric was well-correlated with SST and even precipitation across multiple climate models, with SST and precipitation increasing as ascent area fraction decrease; an intensification and tightening of ascent. Reanalysis data could be used to identify the ascent regions, with TRMM PF and MODIS data used to study convection and clouds within the ascent and descent regions. Such analysis could provide the insight into changes in cloud populations as the ascent region width varies that were initially sought through the Pacific ITCZ width regime metric.

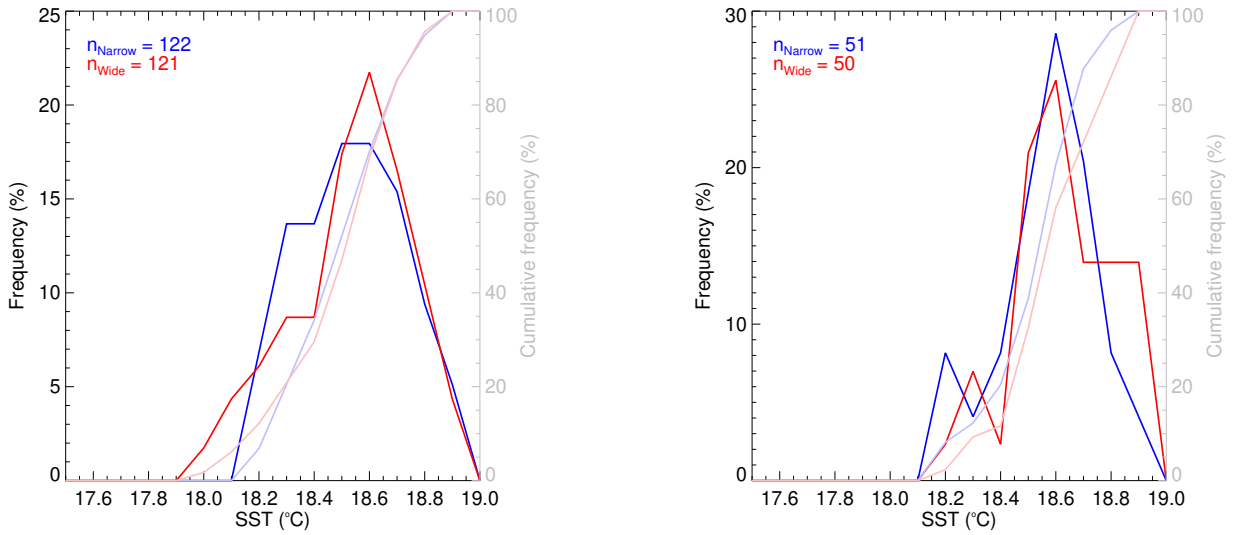

(a) ERA-Interim period 197901-201908

(b) TRMM PF period 199712-201409

Figure 3.17: Histogram of global mean HadISST for (blue) narrow and (red) wide ITCZ months over the (a) ERA-Interim and (b) TRMM PF time periods. Cumulative distributions shown in light colors.

4. VARIABILITY OF TROPICAL CLOUD AND CONVECTIVE POPULATIONS WITH VARIATIONS IN ASCENT AREA FRACTION

4.1 Introduction

The warming climate has many implications, with changes in the hydrologic cycle arguably being one of the most consequential impacts. Changes in the location and intensity of precipitation and convection, namely in the large-scale ascent region of the tropics where the ITCZ controls the wettest regions of the globe, can have negative impacts on crops, property, and water resources. These changes in the tropical ascent region of the overturning circulation can also impact subtropical descent regions of the circulation (Webster 2004; Hu and Fu 2007; Zhou et al. 2011), including a drying of the subtropics through increased subsidence and shifts in the location of the world's deserts through an expansion of the circulation (Hu and Fu 2007; Seidel et al. 2008; Hu et al. 2011; Zhou et al. 2011). These changes in the ascent and descent regions are accompanied by changes in cloud cover (Myers and Norris 2013; Tan et al. 2015; Lau and Tao 2020), which can further modify the location of the ITCZ through their radiative impacts (Voigt et al. 2014). However, clouds remain one of the largest uncertainties in climate models due to inaccuracies in the simulation of their radiative response to warming (Bony and Dufresne 2005). With all these various factors at play, it is important to further our understanding of the relationship between clouds, convection, and large-scale ascent regions.

Recent studies by Zhou et al. (2011), Wodzicki and Rapp (2016), and Byrne et al. (2018) showed that the ITCZ ascent regions in the Pacific and Atlantic have narrowed, and associated precipitation intensified, over the past few decades. These changes can have major implications for the strength of the overturning circulation (Hack et al. 1989; Hou and Lindzen 1992; Dodd and James 1997) and modeling studies indicate that these changes will continue into the future. Using Coupled Model Intercomparison Project Phase 5 (CMIP5) data to study the Hadley circulation in a warming climate, Su et al. (2014) found that the ascent in the ITCZ region strengthened, while ascent at the

margins of this region weakened indicating a narrowing and intensification of the ascending branch of the overturning circulation consistent with the *upped-ante mechanism* (Neelin et al. 2003). The modeled increase in the strength of ascent was accompanied by increases in precipitation and high cloud fraction, while descent in the subsidence regions of the circulation weakened. Su et al. (2019) reinforced the findings of Su et al. (2014) by looking at changes in the ascent and descent regions of the tropical overturning circulation across various CMIP5 model runs. They found subsidence in descent regions weakened with surface temperature increases along with decreases in tropical ascent area fraction (A_u) and increases in tropical ascent strength. However, the variability in cloud radiative effects in the ascent region between models lead to large variability in both ascent area and intensity between the models. It is clear that improving cloud radiative feedbacks in models is required to better forecast future changes in climate, but to do that a better understanding of convection and cloud variability in the current climate is required. Some recent studies have begun to further this understanding by analyzing trends in the frequency and types of clouds across the tropics using various observational datasets.

Using ISCCP data, Tan et al. (2015) identified various cloud regimes using cloud-top pressure and optical thickness in a *k*-means clustering algorithm. A total of three convective cloud regimes were identified, with one being linked to deep, organized convection; the other two regimes represented less organized, weaker convection. They noted that the two weaker convective regimes have become less frequent over the last few decades, with the deep, organized regime becoming more frequent. Tan et al. (2015) then used GPCP RR data to further understand how these changes in the frequency of convection impact precipitation by decomposing and attributing rain to the three different convective cloud types. Using the precipitation attributed to various regimes, they determined that the observed increase in precipitation rates within the ascent regions of the overturning circulation were driven primarily by increases in the frequency of the deep, organized convective regime. While their work provides some insight into changes in the frequency of convective populations, the use of ISCCP data inhibited the study of convective morphology as only basic cloud characteristics (i.e., optical thickness, cloud-top height, etc.) are available.

The work of Wodzicki and Rapp (2020) aimed to extend the results of Tan et al. (2015) by using the TRMM PF database (Nesbitt et al. 2000; Liu et al. 2008) and the ITCZ characteristics database (Wodzicki and Rapp 2016) to study changes in convection in different Pacific ITCZ width regimes. The ITCZ database was used to partition data into wide and narrow ITCZ months in an attempt to mimic the long-term ITCZ width variations, while the PF database provided information about the internal structure of convective features based on the TRMM PR. By studying the morphology of convection at the seasonal to interannual timescales in the Pacific basin, they hoped to infer how convection might change at longer, decadal timescales. However, they found that under the wide (narrow) ITCZ regime, features with large (small) areal extents and high (low) maximum echo-top heights and stratiform area fractions were more (less) frequent in the Pacific basin. These findings were seemingly at odds with the expected differences based on the long-term trends and were determined to be the result of the large influence of ENSO and the Walker circulation in the region, with a weak (strong) zonal SST gradient leading to a weak (strong) Walker circulation allowing (inhibiting) the formation of deep, organized convection across the anomalously wide (narrow) ITCZ in the Pacific basin. With the variability of convection in the Pacific basin dominated by SST variability in the region, it is clear a different metric is required to better understand the link between the extent of the tropical ascent region and cloud and convective populations using relatively short observational records.

To expand upon the work of Wodzicki and Rapp (2020), data from the TRMM PF database and MODIS level 3 data are used to sample the full population of clouds in the tropics. The large influence of regional variations is mitigated by using the tropical ascent area fraction metric defined by Su et al. (2019) to study variations in clouds and convection across the tropics with variations in the overturning circulation; i.e., widening and narrowing. Use of this metric also enables comparison of these observationally-based results in the context of climate model variability shown in Su et al. (2019). Based on results from prior observational and modeling studies discussed above, we hypothesize that *convection within tropical ascent areas will become stronger (weaker) when ascent area fraction is low (high).* With subsidence expected to become weaker with decreases in

ascent area fraction, we expect to see *increased cloud-top heights, with decreases in cloud fraction and LWP in subsidence regions* (Myers and Norris 2013; Su et al. 2014).

4.2 Data and Methods

To identify ascent regions and compute the ascent area fraction (A_u), Su et al.'s (2019) methods are applied to 500 hPa vertical pressure velocity (ω_{500}) data from ECMWF Reanalysis Interim (ERA-Interim; Dee et al. 2011). Using monthly mean data at 1.5° × 1.5° resolution, any grid box with $\omega_{500} < 0.0$ is identified as an area of ascent; other more stringent thresholds to define ascent area were tested and while absolute ascent area changes, there was little impact on the interpretation of the results of the current study (see Appendix). Figure 4.1 shows the frequency of occurrence of ascent at each grid box in the tropical domain over the full ERA-Interim time period (Jan. 1979 – Aug. 2019). As in Su et al. (2019), only data between 30°S-30°N are considered, with A_u computed as the total weighted area of ascent relative to the total weighted area of the domain. This framework is also used to define descent area fraction (A_d; $\omega_{500} \geq 0.0$). With ascent and descent areas defined, the variability of cloud and convective populations in the tropics can be studied as a function of A_u variability. Two datasets are used for the study of clouds and convection: the TRMM PF database (Nesbitt et al. 2000; Liu et al. 2008) and MODIS level 3 cloud retrieval products (Hubanks et al. 2019).

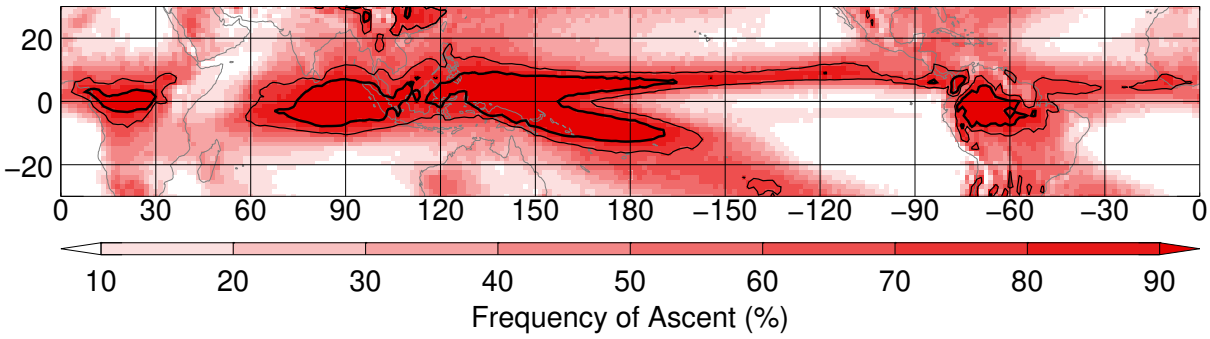

Figure 4.1: Frequency of occurrence of ascent ($\omega_{500} < 0.0$) from ERA-Interim over the period Jan. 1979 – Aug. 2019. Thin and thick contour lines highlight the 70% and 90% levels, respectively.

Carrying the first spaceborne precipitation radar, TRMM provided invaluable information about precipitating clouds across the tropics; however, the 17-years worth of pixel-level data produced by TRMM created quite a data processing challenge. Through the grouping of PR pixels with RRs greater than 0 mm hr^{-1} into contiguous regions, or features, and calculating statistics for various convective characteristics of each feature, the TRMM PF database (Nesbitt et al. 2000; Liu et al. 2008) was created to enable efficient analysis of raining systems observed by the TRMM satellite. The database spans from Dec. 1997 through Sep. 2014; however, the TRMM satellite underwent an orbital boost in August 2001 to extend its life. This change in orbit increased the PR's footprint size from 4.3 km to 5.0 km, which led to some discontinuities in parts of the current analysis, namely the analysis of PF areal extent and related variables such as volumetric RRs. While the inclusion of pre-boost data does not change the general trends shown below, only post-boost data are used to eliminate the influence of these discontinuities. The following convective characteristics are studied to better understand how the intensity of convection varies with A_u; areal extent, maximum echo-top height, volumetric rain, and convective/stratiform partitioning through area fractions and RRs. Using data solely from the PF databases limits the analysis to only raining features detected by the PR, so to study variability in the entire cloud population and across descent regions where there are few deep convective systems, MODIS level 3 data are used.

The MODIS instrument is an across track scanning sensor with 36-spectral bands ranging from 0.4 μm to 14.4 μm. The instantaneous field-of-view of the sensor depends on the spectral band, with the two highest frequency bands sampled at 250 m, the next five bands at 500 m, and the remaining 29 bands at 1000 m. The sensors has a scanning angle $\pm 55^\circ$ and is flown on both the Terra and Aqua polar orbiting, sun synchronous satellites at an altitude of 705 km, giving a swath width of 2,330 km and global coverage every one to two days.

Monthly level 3 MODIS data from both Terra and Aqua are used in the present study. The level 3 data consists of statistics, such as mean, standard deviation, minimum, and maximum, and histograms of pixel counts that are computed from MODIS level 2 data products that have been gridded to a $1^\circ \times 1^\circ$ equal-angle grid. While the level 3 data have limitations (i.e., errors in level 2

data propagate into level 3, limited to statistics provided, etc.), issues such as changes in pixel size across a given scan are mitigated when considering the monthly data (Hubanks et al. 2019). As the focus of the current study is on changes in cloud populations, the variables of interest from MODIS are cloud fraction, cloud height, and liquid and ice water paths (LWP and IWP, respectively). Cloud fraction is used to get a sense of the frequency, and size, of clouds, while cloud height is used as a proxy for convective intensity (Cheng and Houze 1979; DeMott and Rutledge 1998)

To partition the PFs into ascent and descent regions, all PFs are matched to the ERA-Interim grid using the longitude and latitude of fitted ellipses provided by the database (Liu et al. 2008). PFs are then assigned a binary mask to signify if they are in an ascent or descent region. To quantify changes in the intensity of convection, percentiles of convective intensity metrics for deep convective features are regressed onto A_u. Here, deep convection is defined by maximum echo-top height $\geq$ 10 km based on a modified version of the Johnson et al. (1999) criteria. Variability in the 95th percentile is shown to illustrate shifts in the distribution of the strongest convective features; lower percentiles (e.g., 80th percentile) produce similar signed, but weaker, correlations. MODIS data are also matched to the ERA-Interim grid, using a nearest neighbor method, for separation into ascent and descent regions. In ascent regions, the 95th percentile of MODIS grid box mean values is used to represent intense convection. While this is not an exact measure of storm intensity as these data are grid box means, larger grid box mean values can indicate a shift in the underlying cloud distribution or the presence of clouds in the tails of the distribution; either of which would lead to an increase in the grid box mean value. In descent regions, median values of MODIS grid box mean characteristics are used to gain insight into changes in general cloud characteristics.

For computation of local correlations between cloud and convection characteristics and A_u, PFs are gridded to a $2.5^\circ \times 2.5^\circ$ grid to increase the number of features in each grid box and reduce noise; PFs are only sampled when the TRMM satellite is overhead and there is precipitation. Monthly percentile values are then computed as above for each grid box. MODIS data are used at their native, $1.0^\circ \times 1.0^\circ$, resolution as MODIS can, generally, gather cloud information during every overpass; i.e., it is not limited to only seeing raining features.

Least-square linear regressions and Pearson r values are calculated to determine the relationships between cloud and convective characteristics and A_u. The statistical significance of correlation coefficients is determined using a standard 2-tailed *t*-test using the effective degrees of freedom (Thomson and Emery 2014) to reduce the influence of auto-correlations in the time series that can lead to type I errors. The effective degrees of freedom are also used when computing confidence intervals for slopes.

To determine the influence of ENSO on the results of the current analysis, a method similar to that of Bain et al. (2011) is used. Data are first converted to anomalies by removing the climatological mean (e.g., anomalies of PF maximum echo-top height) and then months where the Multivariate ENSO Index (MEI; Wolter and Timlin 1993, 1998) is greater (less) than 0.5 (-0.5) are regressed against their corresponding MEI values. This provides a mean anomaly for large ENSO events, which is then removed from the raw data to reduce the ENSO signal.

4.3 Results

4.3.1 Convection and Clouds Within Ascent Regions

Figure 4.2 shows the monthly, 95th percentile values of four PF characteristics for all cumulonimbus PFs (maximum echo-top heights $\geq$ 10 km) within ascent regions plotted against monthly A_u. The four characteristics are convective RR, stratiform RR, area, and stratiform area fraction. Least-squares linear regressions (solid black) and 95% confidence bounds on the regression (dashed-black) are also plotted. As deep convection is sensitive to columnar water vapor (CWV; Graham and Barnett 1987; Zhang 1993), ascent area averaged ERA-Interim CWV is also indicated by symbol color. The correlations of these variables with A_u are all negative, with the 95th percentile increasing (i.e., deep convection shifting to larger, more organized and vigorously raining systems) as A_u decreases, but only stratiform RR is statistically significant at the 95% level. Convective RR shows a weak negative correlation with A_u (Figure 4.2a), indicating that the convective RR of PFs within ascent regions increases as A_u decreases. This is in line with previous studies that indicate a narrowing and intensification of the ascending branch of the overturning circulation

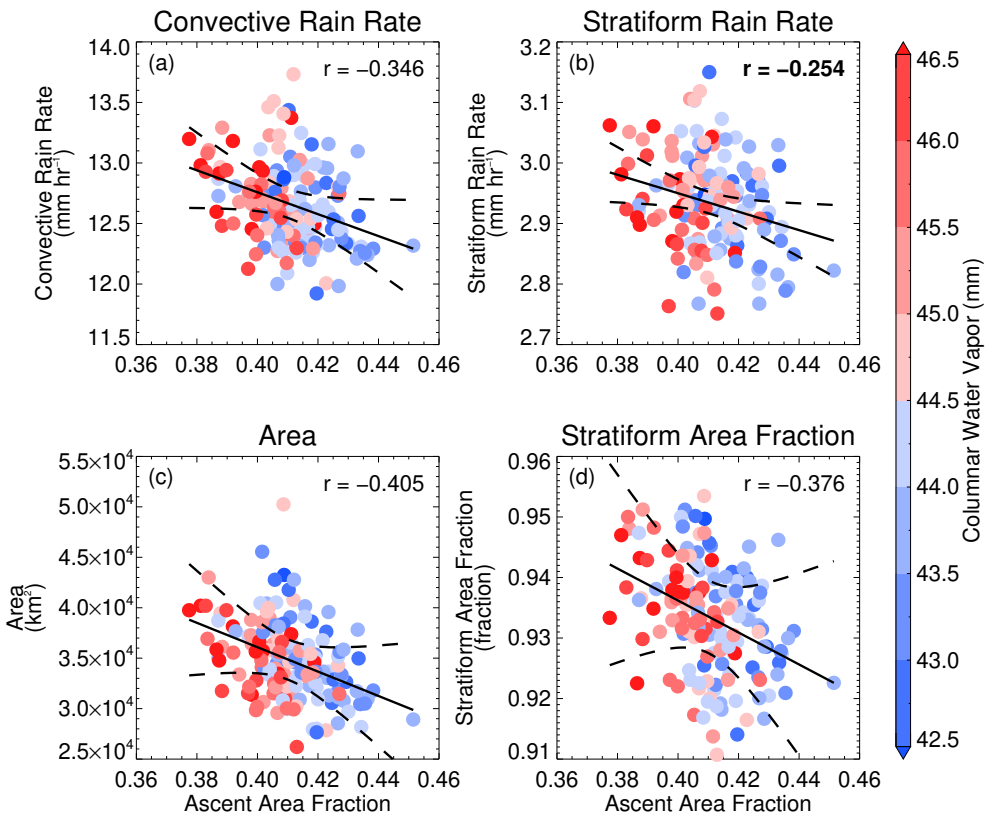

Figure 4.2: Monthly A_u versus the 95th percentile of (a) convective rain rate, (b) stratiform rain rate, (c) area, and (d) stratiform area fraction for cumulonimbus (maximum echo-top height $\geq$ 10 km) PFs within ascent regions. Correlation coefficients are shown at the top right of each panel with bold values being significantly different than zero at the 95% level. Solid black lines show the least-squares linear regression, with dashed lines showing the 95% confidence bounds for the regression. Symbols are colored to show the ERA-Interim mean columnar water vapor within the ascent region.

(Zhou et al. 2011; Wodzicki and Rapp 2016; Lau and Kim 2015; Su et al. 2019). The correlation between stratiform RR and A_u (Figure 4.2b) is also negative, and is significantly different from zero at the 95% level (bolded r value), with stratiform RRs increasing as A_u decreases. The relationships between A_u and PF area (Figure 4.2c) and stratiform area faction (Figure 4.2d) are both negative, indicating an increase in the areal extent and stratiform area of PFs as A_u decreases; however, the uncertainty in the relationship of A_u and stratiform area fraction is quite large. The relation between A_u and CWV shows a negative correlation, with CWV increasing as A_u decreases.

In a check of consistency between the PF and MODIS data, the 95th percentile of monthly grid

box means of cloud fraction, cloud-top height, LWP and IWP for all MODIS Terra grid boxes within ascent regions are plotted against A_u in Figure 4.3. Note that only results from Terra are shown as the general relationships between these variables and A_u are the same between Terra and Aqua data, but the Terra dataset is longer. First, the ascent area ERA-Interim mean CWV patterns are similar to those of Figure 4.2 with larger (smaller) CWV values tending to occur when A_u is low. Cloud fraction in the ascent region (Figure 4.3a) is negatively correlated with A_u indicating an increase in general cloud cover in the ascent region as it narrows. This is in line with the increases in PF areal extent and stratiform area fraction shown in Figures 4.2c and 4.2d, respectively, and is likely the

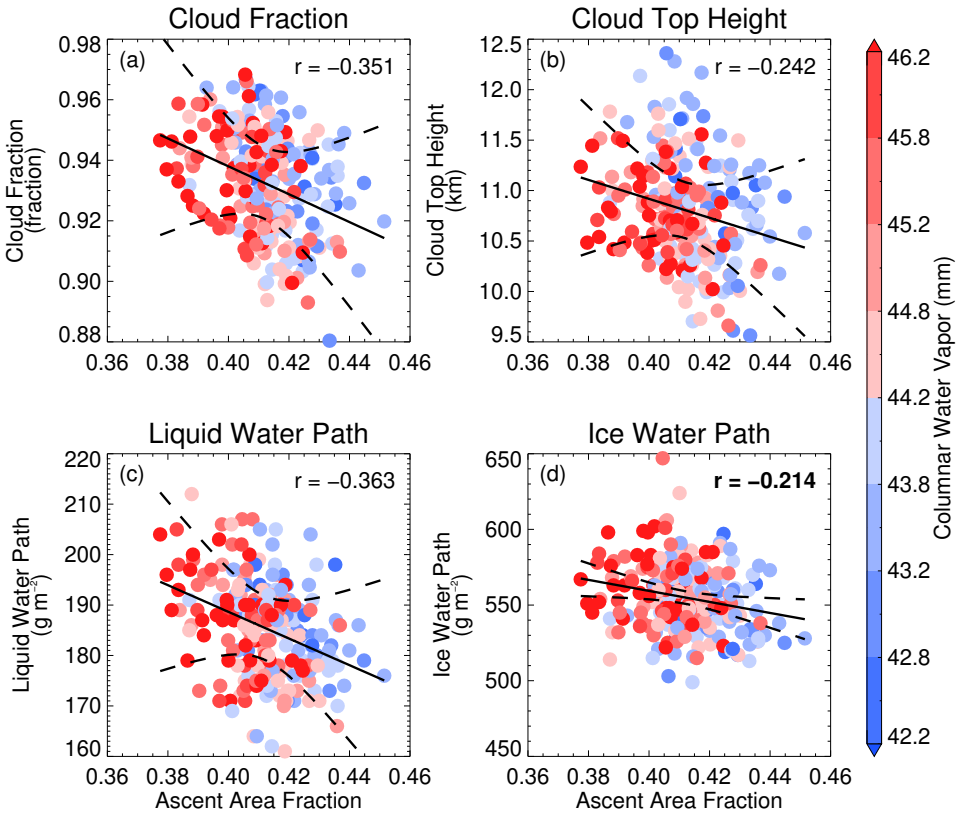

Figure 4.3: Monthly A_u versus the 95th percentile of (a) cloud fraction, (b) cloud-top height, (c) cloud water path, and (d) ice water path for all MODIS Terra grid boxes within ascent regions ($\omega_{500} < 0.0$). Correlation coefficients are shown at the top right of each panel with bold values being significantly different than zero at the 95% level. Solid black lines show the least-squares linear regression, with dashed lines showing the 95% confidence bounds for the regression. Symbols are colored to show the ERA-Interim mean columnar water vapor within the ascent region.

result of increased anvil cirrus as systems become larger and more organized. Cloud-top height also shows a negative correlation with A_u (Figure 4.3b), although the correlation is weaker as the 95th percentile of cloud-top height appears more variable than cloud fraction. LWP and IWP both show negative correlations with A_u (Figures 4.3c and 4.3d, respectively), with IWP having a correlation that is statistically different than zero at the 95% level. While the correlation is weak, increases in IWP as A_u decreases indicates an intensification of convection with narrowing of ascent, as IWP increases as convection becomes deep and/or anvil area increases. As with the PF data there is consistency in the sign of the relationships between MODIS data and A_u, indicating robustness in the general changes in convection and clouds as A_u varies; convection within ascent regions is more intense with larger, deeper, and more organized storms as A_u decreases.

Tests of the impact of ENSO as outlined in the Data and Methods section were performed for both the PF and MODIS data (not shown) and showed only very small changes in correlations between the various cloud and convective characteristics and A_u, indicating that ENSO does not have a significant impact on these tropical ascent area results.

4.3.2 Clouds Within Descent Regions

Analysis in the descent regions of the tropics is aimed at understanding the general characteristics of clouds, both raining and non-raining, with only MODIS data analyzed as the TRMM PR has difficulty sampling lightly raining systems and cannot sample the ubiquitous non-raining clouds in these regions. Figure 4.4 is similar to Figure 4.3, but shows the monthly median values of all grid box mean values within descent regions ($\omega_{500} \geq 0.0$). Symbols are colored based on the monthly mean ERA-Interim CWV in the descent region. Unlike in the ascent region, the relationships between cloud characteristics and A_u in the descent region are not all the same sign. While cloud fraction (Figure 4.4a) shows a negative correlation with A_u, indicating cloud fraction increases as A_u decreases, cloud-top height (Figure 4.4b) shows a positive correlation, with cloud tops reaching higher into the atmosphere as A_u increases. LWP and IWP (Figures 4.4c and d, respectively) also show different relations, with a negative correlation between LWP and A_u and a positive correlation

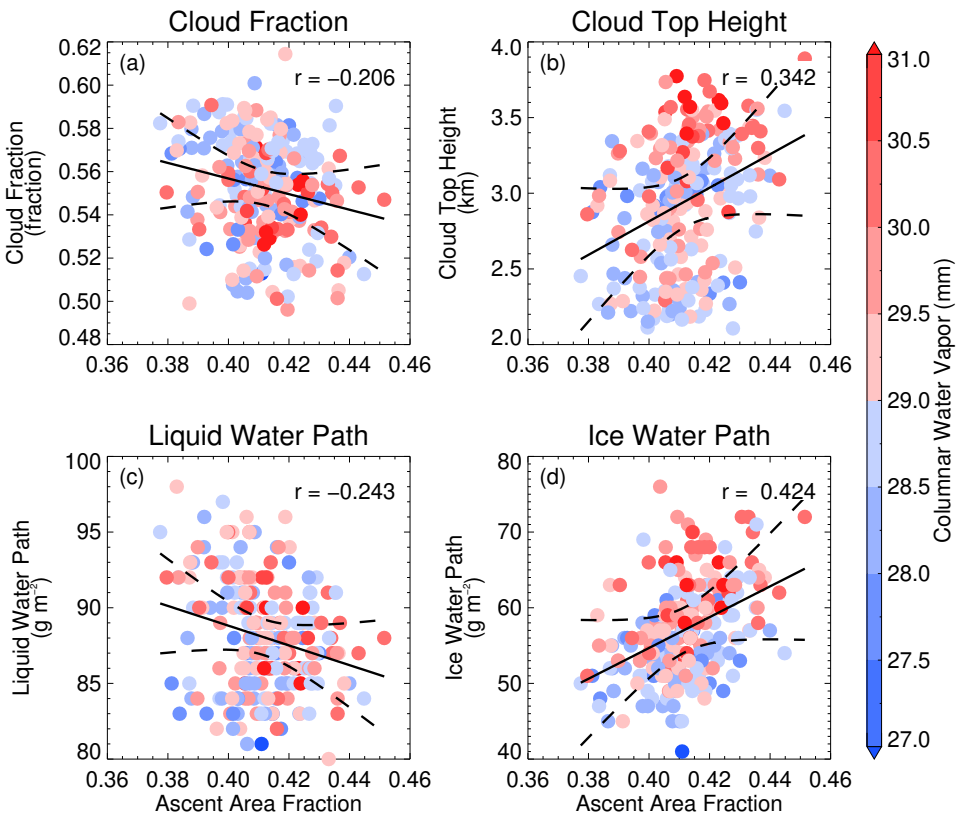

Figure 4.4: Monthly A_u versus the median values of (a) cloud fraction, (b) cloud-top height, (c) cloud water path, and (d) ice water path for all MODIS Terra grid boxes within descent regions ($\omega_{500} >= 0$). Correlation coefficients are shown at the top right of each panel with bold values being significantly different than zero at the 95% level. Solid black lines show the least-squares linear regression, with dashed lines showing the 95% confidence bounds for the regression. Symbols are colored to show the ERA-Interim mean columnar water vapor within the descent region.

between IWP and A_u. Although none of the correlations are significantly different from a zero correlation at the 95% level, the relationships point towards an increase in subsidence strength as A_u decreases. Myers and Norris (2013) showed that as subsidence strength increases in eastern subtropical ocean regions, convection is suppressed, reducing cloud height, cloud fraction and LWP. However, they also note that the increased inversion strength that accompanies stronger subsidence counteracts the reduction in cloud fraction and LWP.

Shifting to the link between A_u and CWV, there does appear to be some correlation between A_u and CWVs in the subsidence region. Lower values of CWV (cool colors) tend to occur when

A_u is relatively small, while higher values of CWV (warm colors) tend to occur when A_u is relatively large. This apparent drying of the subsidence region with reduced A_u further indicates a strengthening of subsidence in the descent region.

Tests of the impact of ENSO were again performed for MODIS data in the descent region (not shown) with no significant impact on the outcomes.

4.3.3 Local Trends in Convection and Clouds

With a general understanding of how clouds and convection vary across the tropics with A_u, how do these populations vary regionally? To study this, monthly PF data are gridded to a $2.5^\circ \times 2.5^\circ$ grid (see Data and Methods) and then the 95th percentile of various PF characteristics is computed using only the distribution of cumulonimbus PFs within a given grid box. These 95th percentile monthly grid box values are then regressed onto $-A_u$ so that positive correlations correspond to changes with narrowing; e.g., a positive correlation of PF area and $-A_u$ means that PF area increases at a given grid box as tropical ascent area fraction decreases. Figure 4.5 shows the correlations for PF area, stratiform area fraction, maximum echo-top height, and convective RR. The lack of correlations outside of the climatological ascent region (outlined by black contour) is due to the infrequency of deep convection (maximum echo-top heights $\geq$ 10.0 km) in those grid boxes. In general, the four PF characteristics have similar trends across regions, with all characteristics showing generally negative correlations over central Africa, the Amazon, and the Indian Ocean, mainly positive correlations over the Pacific ITCZ and warm pool regions, and mixed signs in the SPCZ region and Atlantic Ocean. Across the Pacific Ocean correlations tend to be positive, signifying increases in PF area, echo-top height, and convective RR as A_u decreases. Note that these findings are opposite of those of Wodzicki and Rapp (2020) because they studied the intensity of convection in the Pacific as the Pacific ITCZ varied, whereas the present results show regional variability related to tropics wide changes. At the margins of the climatological ascent region (black contour) in the Pacific, namely in the SPCZ, there tends to be negative correlations, while positive correlations exist near the center of the ascent regions. In the Atlantic Ocean a similar pattern is shown for PF area

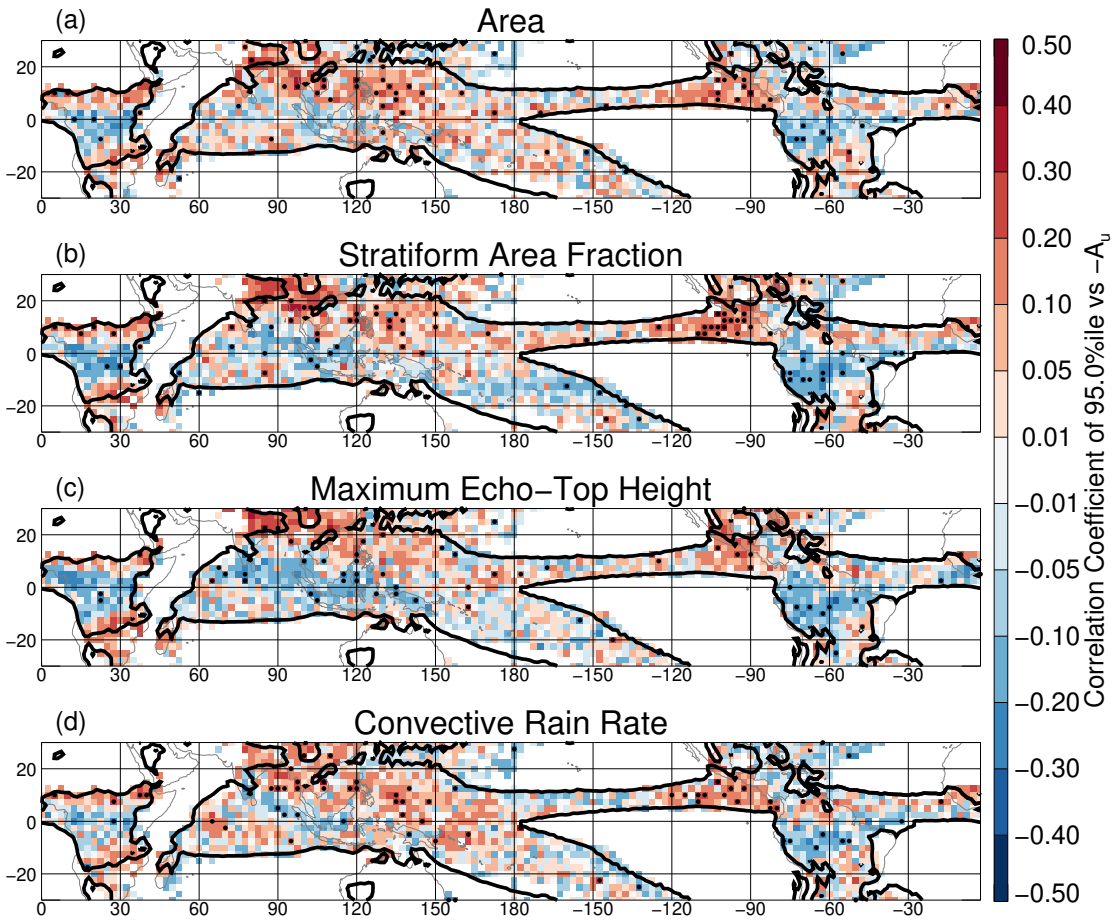

Figure 4.5: Correlation coefficients of the monthly 95th percentile of PF (a) area, (b) stratiform area fraction, (c) maximum echo-top height, and (d) convective rain rate for each grid box regressed onto monthly $-A_u$ values. $-A_u$ is used so that positive correlations correspond to an increase in the 95th percentile of a variable as A_u decreases; i.e., changes with narrowing. The black contour line shows the mean location of $\omega_{500} = 0$. Black dots in grid boxes indicate that the correlation is significantly different from zero at the 95% confidence level.

and maximum echo-top height, with positive (negative) correlations near the center (edges) of the ascent region. While the vast majority of correlations are not different from zero at the 95% level (i.e., no stippling), the general patterns match those expected from the results of Su et al. (2020) and Lau and Tao (2020), with strengthened (weakened) convection over ocean (land) with narrowing ascent.

Looking at the overall cloud population, Figure 4.6 shows MODIS low, mid, and high level cloud fractions regressed onto $-A_u$. In general, in the ascent regions, cloud fractions at all lev-

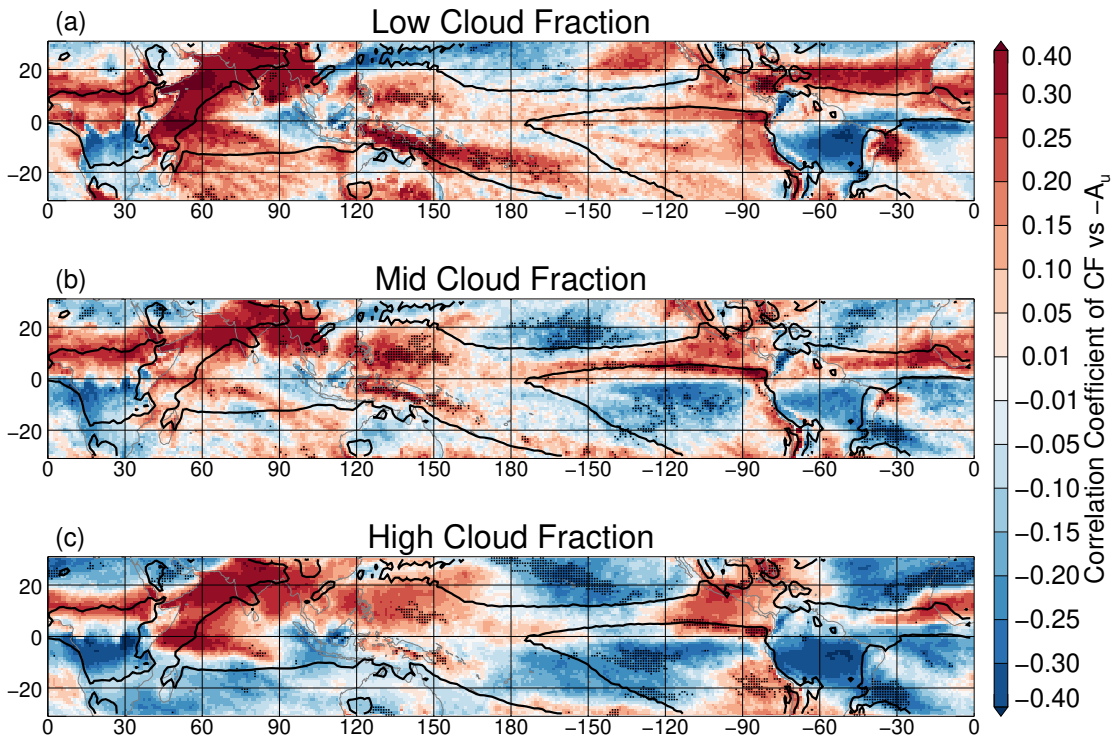

Figure 4.6: Correlation coefficients of MODIS (a) low, (b) mid-level, and (c) high cloud fraction onto monthly $-A_u$ values. Cloud types are defined as cloud-top pressures $>$ 680 hPa, 680 $-$ 440 hPa, and $<$ 440 hPa for low, mid, and high clouds, respectively. $-A_u$ is used so that positive correlations correspond to an increase in cloud fraction as A_u decreases; i.e., changes with narrowing. The black contour line shows the mean location of $\omega_{500} = 0$. Black dots in grid boxes indicate that the correlation is significantly different from zero at the 95% confidence level.

els tend to increase as A_u decreases (positive correlations), with Africa and the Amazon being the exception showing decreases in cloud fraction as A_u decreases (negative correlations). In descent regions, mid and high cloud fractions (Figures 4.6b and 4.6c, respectively) decrease as A_u decreases (negative correlations), while low cloud fraction (Figure 4.6a) is a bit more complicated. In stratocumulus regions (e.g., north and southeastern Pacific and Atlantic), positive correlations between low cloud fraction and $-A_u$ are found. Positive correlations are also found across the northern Atlantic and southern Pacific descent regions, with negative correlations spanning much of the northern Pacific and parts of the southern Atlantic. These opposite correlations in various regions are likely due differences in cloud types present in the various regions (Oreopoulos and Rossow 2011) responding differently to variability in subsidence strength. Myers and Norris (2013) studied

the influence of subsidence strength in eastern subtropical oceans and found increased subsidence leads to higher cloud fractions; these are the same regions that show mainly positive correlations in the present analysis.

Figure 4.7 shows the correlations for regressions of monthly mean MODIS Terra cloud properties onto $-A_u$. Generally, patterns match those of Figure 4.5, although there are some caveats. Figure 4.7a shows overall cloud fraction and is clearly a combination of the three cloud types in Figure 4.6. Decreases in cloud fraction are shown over central Africa, the Amazon, and parts of

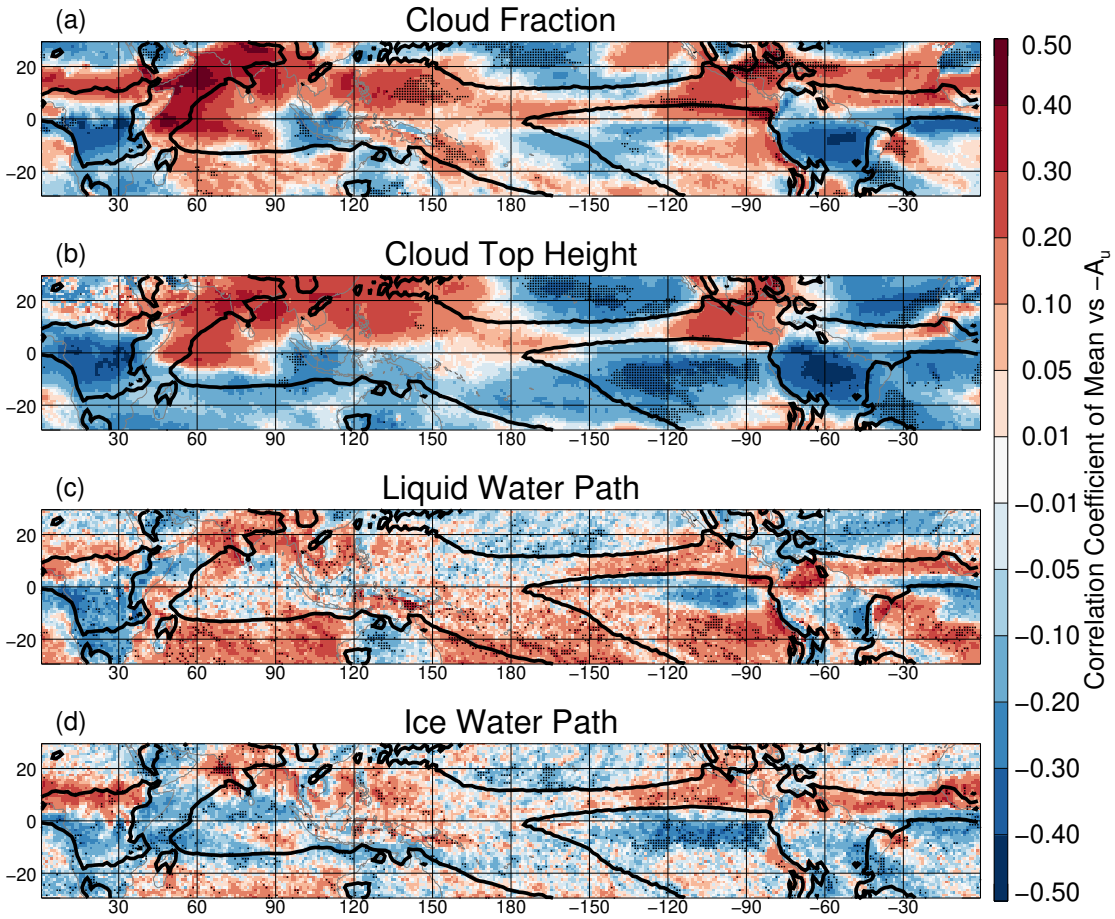

Figure 4.7: Correlation coefficients of MODIS Terra grid box means of (a) cloud fraction, (b) cloud-top height, (c), liquid water path, and (d) ice water path regressed onto monthly $-A_u$ values. $-A_u$ is used so that positive correlations correspond to an increase in the grid box mean as A_u decreases; i.e., changes with narrowing. The black contour line shows the mean location of $\omega_{500} = 0$. Black dots in grid boxes indicate that the correlation is significantly different from zero at the 95% confidence level.

the descent regions of the Pacific and Atlantic Oceans as A_u decreases (negative trend). Positive correlations appear in the stratocumulus regions of the Pacific and at the northern edge of the ascent region extending into the descent region in the Atlantic Ocean indicating that cloud fraction increases with decreasing A_u. Cloud-top height (Figure 4.7b) shows positive correlations across much of the Pacific ITCZ region and the northern portions of the western Pacific warm pool and the Indian and Atlantic Oceans. In all other regions (land, subsidence, and even the SPCZ), negative correlations are found indicating increases in cloud-top height as A_u increases. The spatial patterns in the correlations of cloud-top height and $-A_u$ are very similar to those of high cloud fraction (Figure 4.6c), showing consistent relationships between variables. From these two cloud properties, a general increase in cloudiness and cloud-top height is present across the Pacific Ocean ascent region, indicating a shift to deep organized convection, which consists of high clouds with large areal extents, as A_u decreases. The Atlantic Ocean ascent region is more complex, with positive correlations present near the northern boundary of the ascent region in cloud fraction and cloud-top height, but negative correlations across the southern half of the ascent region. In the subsidence region of the northern tropical Atlantic, low clouds seem to drive trends, especially in cloud fraction (Figure 4.6a), with cloud fraction increasing, and cloud-top heights decreasing, as A_u decreases. These trends in the northern tropical Atlantic match those of stratocumulus regions. Over the Amazon and central Africa, deep convection also seems to be suppressed, with negative correlations in those regions.

Figures 4.7c and d show LWP and IWP, respectively, with LWP showing a clear hemispheric influence while IWP is fairly similar to the patterns in cloud-top height. The most obvious pattern in LWP is that positive correlations are generally found in the Southern Hemisphere with negative correlations in the Northern Hemisphere. Manaster et al. (2017) found similar hemispheric asymmetry in long-term trends of LWP, which they conjectured to be related to a weakening of the Walker circulation. Over land, namely central Africa and the Amazon, negative correlations between LWP and $-A_u$ are found, with somewhat mixed correlations in the Indian Ocean and western Pacific warm pool. In the eastern Pacific and in the northern half of the climatological ascent region

in the Atlantic Ocean, positive correlations are found. For IWP, positive trends are found in the western Pacific warm pool and in the northern half of the ascent region in the Atlantic. Over land, as with LWP, negative correlations are shown between IWP and $-A_u$. Correlations in subtropical regions are largely negative, matching the patterns in cloud-top height well.

4.4 Discussion and Conclusions

Observational studies of the impact of climate change on the hydrologic cycle indicate that the ascent region of the overturning circulation (the ITCZ) has been narrowing in conjunction with an increase in the intensity of the associated precipitation (Zhou et al. 2011; Wodzicki and Rapp 2016; Lau and Tao 2020). This trend is predicted to continue in the future climate (Lau and Kim 2015; Su et al. 2017, 2019); however, how convective and cloud populations change along with this narrowing is not fully understood. Using TRMM PF, MODIS, and ERA-Interim data, along with tropical ascent area fraction (A_u) defined as in Su et al. (2019), the relationship between A_u variability and convective and cloud populations was studied. TRMM PFs and MODIS level 3 grid boxes were sorted into ascent and descent regimes and general statistics (i.e., median, 75th percentile, 95th percentile, etc.) were computed for various convective characteristics such as convective RR for PFs and IWP for MODIS data. In the case of PFs, only those features with maximum echo-top heights $\geq$ 10 km within the ascent regions were included to ensure only the most vigorous convection was studied as extreme precipitation has been shown to increase under global warming (Allan and Soden 2008; O'Gorman 2015). Analysis was also limited to deep convective features as there is evidence that organized deep convection is mainly responsible for the aforementioned long-term trends in precipitation (Tan et al. 2015).

Based on the general relationship between A_u and the various characteristics, our results support the hypothesis that *convection within tropical ascent areas will become stronger (weaker) when A_u is low (high)*, with increases in convective intensity metrics (e.g., greater RRs) when A_u is low. While many of these relationships are weak, the sign of the relationships are consistent across multiple different intensity metrics, helping to establish a broad pattern for changes. Clouds

and convection were found to have increased convective and stratiform RRs, areal extents, and stratiform regions, as well as slightly higher cloud-top heights within the ascent region as it narrowed. CWV was also found to increase within the ascent region under narrowing, consistent with the long-term changes noted by Lau and Tao (2020). These relationships are consistent with many mechanisms and phenomena used to explain observed, and predicted, changes.

The *rich-get-richer* or *wet-get-wetter* mechanisms (Chou and Neelin 2004; Chou et al. 2009) indicate that moisture and precipitation will increase in moist, convective regions where heavy precipitation is frequent (e.g., the ITCZ) as the climate warms, while moisture and precipitation in subsidence regions will be suppressed. As the ascent region has been narrowing with warming (Zhou et al. 2011; Wodzicki and Rapp 2016; Byrne et al. 2018), the present results appear similar to expected patterns associated with the aforementioned mechanism, with CWV increasing (decreasing) in the ascent (descent) regions as A_u decreases. Studies of climate model output have shown similar responses in precipitation and moisture.

Analyzing CMIP5 model output, Lau and Kim (2015) noted a decrease in moisture across the tropics, except in the ascent regions where precipitation was found to increase as the model climate warmed. They also noted a narrowing of the ascent region. Su et al. (2017) found a similar narrowing of ascent with a concurrent increase in precipitation intensity in the ascent region in CMIP5 model output. Both of these studies noted that changes in cloud radiative feedbacks could play a role in the narrowing and intensification of ascent, with Su et al. (2017) noting high correlations between ascent area, high cloud fraction variability, and longwave radiative cooling. With this study showing high cloud fraction decreasing across much of the tropics (except in the ascent region) and cloud-top heights decreasing within subsidence region as A_u decreases, longwave radiative cooling is expected to increase as A_u decreases, consistent with Su et al. (2019).

While still located in the climatological ascent regions, the Amazon and central Africa show relationships with A_u that are opposite to the rest of the ascent regions. Some of these differences are likely due to seasonal influences (A_u tends to be narrow during dry seasons); however, there are likely other mechanisms at play. Su et al. (2020) noted a similar relationship between precipitation

and A_u in the Amazon (i.e., reduction in convection as A_u decreases) at both interannual and seasonal timescales using observational datasets. They attributed these changes to a regional impact of the large-scale tropical circulation changes. Changes in wet season onset may also help explain the observed relationships. Yin et al. (2014) found that a poleward displacement of extratropical systems, and by extension cold fronts, could delay wet season onset by removing a dynamic trigger for convection. As extra tropical storm tracks tend to move poleward as ascent area decreases (Seidel et al. 2008; Lau and Tao 2020), decreasing A_u could delay wet season onset, reducing convection across the Amazon.

In the descent region, the relationships between A_u and cloud fraction, cloud-top height, and LWP were all opposite of the hypothesized relationships, with cloud fraction and LWP increasing (cloud-top height decreasing) as A_u decreased. This suggests the strength of subsidence actually increases as A_u decreases, as stronger subsidence acts to suppress the vertical growth of clouds and, through increasing the strength of the boundary layer inversion, can lead to increased cloud cover and LWP (Myers and Norris 2013). These changes fit with those in CWV, which indicates a decrease in moisture in the descent region as A_u decreases that acts to suppress the vertical growth of convection. However, maps of regional changes provide a clearer picture of changes in subsidence regions, highlighting the opposite changes in different cloud regimes. In regions where stratocumulus clouds are dominant (the north and southeastern regions of the Pacific, Atlantic, and Indian Oceans), low cloud fractions tend to increase, whereas in regions dominated by shallow cumulus type clouds (central regions of oceans), low cloud fraction decreases. These changes match long-term changes in OLR shown by Lau and Tao (2020), with OLR increasing in regions where this study shows decreasing low cloud fraction. But, why is some of the relatively short-term variability in the subsidence regions studied here, and the long-term trends of Lau and Tao (2020), that indicate a strengthening of descent with decreased A_u seemingly at odds with climate predictions of weakening descent?

One possible reason for the apparent differences is that natural SST variability is currently masking long-term trends in observational data in the subsidence regions; i.e., the time of emer-

gence has not yet been met in the current observational record (Hawkins and Sutton 2012). Another is that changes in the phase of teleconnections, namely the Pacific Decadal Oscillation, are responsible for the observed trends across the tropics (Gu et al. 2015). Su et al. (2014) outline a completely different mechanism by which weakened subsidence could lead to the decreases in clouds shown in model projections. They postulate that weaker subsidence would allow clouds to deepen, leading to increased mixing between the free troposphere and boundary layer. This increased mixing would act to dry the boundary layer and, ultimately, lead to reductions in clouds in the subsidence region.

The present study indicates that as the climate warms and ascent narrows, convection shifts toward more organized, deep convective storms with large stratiform area fractions and increased rain rates. Neelin et al. (2009) found that precipitation rates increase rapidly above a critical value of CWV, with Ahmed and Schumacher (2015) finding that most of the increase can be attributed to increased stratiform rain area not rain intensity. While the ascent area mean CWV is below the critical values noted in the aforementioned studies (around 55 mm) because we average the entire region not just where convection is occurring, the general trend of increasing CWV and stratiform fraction with decreasing A_u provides evidence of increased organized convection. These findings are in line with the idea of convective aggregation (Holloway et al. 2017), wherein convection acts to isolate itself into large, organized convective systems in relatively high CWV environments. A modeling study by Bony et al. (2016) even indicates that convective aggregation may enhance the narrowing of ascent regions in a warming climate through radiative and circulation feedbacks. The findings of Tan et al. (2015) also point to possible convective aggregation influence as they found deep, organized convection has become more frequent over recent decades as the ITCZ has narrowed.

General relationships of convection and cloud characteristics and A_u across ascent and descent regions are consistent with those of long-term observed trends; however, regional variations are quite significant. It is promising that some of the relationships, namely within the ascent regions, are consistent with those of predicted future climates (i.e., increase in convective intensity with a

narrowing of ascent), but some relationships are at odds (i.e., subsidence seems to strengthen while models predict weakening). Su et al. (2014) noted complex meridional structures in Hadley circulation changes under global warming that may help explain the apparent differences in variability between the present and future climate. Perhaps the climate has not yet reached the temperatures where aforementioned mechanisms (e.g., *upped-ante*) begin to have significant influence on circulation changes, or variability in cloud radiative feedbacks in models are leading to yet undiscovered biases (Bony and Dufresne 2005; Ceppi et al. 2017; Kolly and Huang 2018). More work is still required to understand the apparent differences between clouds in the current climate and projected future climate.

5. SUMMARY

Analysis of long-term trends in observations has shown a narrowing of the Intertropical Convergence Zone (ITCZ) and intensification of associated convection (Zhou et al. 2011; Wodzicki and Rapp 2016; Byrne et al. 2018; Su et al. 2020; Lau and Tao 2020). Lau and Tao (2020) also found a drying in the subsidence regions of the tropics, which has led to an increase in longwave cooling. Studies of climate model output (i.e., Lau and Kim 2015; Su et al. 2014, 2019) have shown that the ascent region of the overturning circulation, or ITCZ, will continue to narrow, and associated precipitation intensifies, as the climate warms. However, clouds are consistently a large source of errors in models (Bony and Dufresne 2005; Bony et al. 2015). Using various observational and reanalysis datasets the variability of clouds and convection with respect to variations in ITCZ width and ascent area in the current climate have been studied with the hope of inferring how clouds and convection may change in the future.

Based on the long-term trends of narrowing and intensification, the original hypothesis (Chapter 2) was that Pacific ITCZ convection would be more intense (i.e., greater rain rates, higher echo-top heights, and larger areal extents) when the ITCZ is narrow than when it is wide. Using data from the Tropical Rainfall Measuring Mission (TRMM) precipitation feature (PF) database (Nesbitt et al. 2000; Liu et al. 2008), convective feature characteristics (e.g., maximum echo-top height, areal extent, and stratiform area fraction) were studied to quantify the variability in convective intensity with variations in ITCZ width. To overcome the limitation of the relatively short data period provided by the PF database (roughly 17 years), PFs were partitioned into wide and narrow ITCZ width regimes using the ITCZ characteristics database from Wodzicki and Rapp (2016), which limited the analysis of convection to the central and eastern Pacific Ocean.

Results showed that deep, organized convection with large areal extents and stratiform area fractions is more frequent under the wide ITCZ width regime in the Pacific Ocean than the narrow, leading to the rejection of the hypothesis. Further analysis showed that both sea surface temperature (SST) and columnar water vapor (CWV) increased in the wide ITCZ regime relative to the

narrow. This, coupled with El Niño-Southern Oscillation (ENSO)'s influence on ITCZ width and the limited domain of study, indicated that a weakening of the Walker circulation, associated with ENSO variability, was likely the reason for increases in deep convective frequency in the wide ITCZ regime. However, it was possible that the ENSO signal was simply overwhelming a long-term-like signal of increased convective intensity under a narrow ITCZ width regime.

By addressing some limitations in the study presented in Chapter 2, such as removing the ENSO signal and testing other domains in the Pacific Ocean, Chapter 3 aimed to better understand convective variability in the Pacific. Although the signals became much weaker, the same increases in the frequency of intense convection under a wide ITCZ regime was found after reducing the influence of confounding signals. With patterns in changes similar between the two analyses, and the close relationship between the ITCZ and the Hadley circulation, a regional analysis of the Hadley circulation was performed in an attempt to understand the apparent discrepancies between observed long-term trends and the variability shown here. Through the meridional mass stream function, clear regional variations in the Hadley circulation were found, with the Pacific portion of the circulation being significantly coherent with the Multivariate ENSO Index (MEI), showing an increase in overturning strength and a widening of the circulation under El Niño. Over the reset of the globe, the opposite signal was found, with a contraction and weakening of the circulation. When considering the global, zonal mean circulation, these regional variations averaged out to show an increase in circulation strength and narrowing of meridional extent under El Niño. It became clear that further analysis of convection must consider the entire globe to reduce the influence of these regional variations.

To expand the analysis to the global tropics, the ascent area fraction (A_u) metric of Su et al. (2019) was used in Chapter 4 to study both convection and general cloud populations across the tropics (30°S-30°N) as A_u varies using the PF dataset and Moderate Resolution Imaging Spectroradiometer (MODIS) level 3 data. Two new hypotheses were tested; the first was similar to the original hypothesis in Chapter 2, with convection within ascent regions expected to become more intense as A_u decreases, while the second hypothesis stated clouds in the subsidence regions would

become more frequent as subsidence has been predicted to decrease as ascent decreases in future climates. Through partitioning of convective features and MODIS level 3 grid boxes into ascent and descent regions, it was determined that, globally, convection within ascent regions becomes more intense and organized, with increased rain rates and stratiform area as A_u decreases. This finding supports the first new hypothesis and is consistent with long-term observed changes (Su et al. 2020; Lau and Tao 2020) and predicted future changes (Lau and Kim 2015; Su et al. 2017, 2019). However, in the subsidence regions, the signal is a bit mixed due to regional variability between cloud regimes. Overall, clouds in the subsidence region were found to become more frequent (increased cloud fraction) and shallower (lower cloud-top heights) as A_u decreased. These changes are indicative of increased subsidence limiting the vertical development of clouds while increasing cloud cover as clouds are restricted to the boundary layer (Myers and Norris 2013). Analysis of regional trends indicated that increases in cloud fraction with decreases in A_u occurred primarily in stratocumulus regions at the eastern edges of ocean basins, while cloud fractions in shallow cumulus regions near the middle of ocean basins decreased. While these changes are consistent with increased subsidence, it is clear that current variability in subsidence regions does not match that of predicted trends.

The relationship between ITCZ width and ascent area fraction and deep convection with the ascending branch of the Hadley circulation has been thoroughly analyzed, with seasonal and interannual variability matching that of observed long-term trends and trends predicted by models as the climate continues to warm. As convective populations shift toward more intense convective systems with high cloud-top heights and large areal extents longwave radiative cooling in ascent regions of the overturning circulation is expected to decrease. However, some studies of convective aggregation indicate that longwave cooling may actually increase as convection organizes into relatively small, isolated areas that are separated by large, mostly cloud-free regions (Holloway et al. 2017, and references therein). These competing controls on longwave radiatve cooling in the ascending regions of the tropics makes determining the exact radiative impact of these convective changes extremely difficult. Arguably a larger concern is the direct impact of increased rain

intensity with shifts to these organized convective systems.

We have shown rain rates increase within the ascent region as it narrows, with studies of model output indicating further shifts to extreme precipitation in the future (Allan and Soden 2008; Pendergrass and Hartmann 2014). Coupled with more aggregated convection, it is possible that as rain rates within ascent regions continue to increase as A_u decreases, rain will become less frequent, but more extreme. That is to say, as convection is more aggregated, the frequency in which a given location receives rain will decrease; however, when it rains, the rain will be more intense. Pendergrass and Hartmann (2014) studied the response in rain frequency and intensity to global warming using Coupled Model Intercomparison Project Phase 5 (CMIP5) output and found dry-day frequency increased and heavy rain became more frequent. Such changes in the hydrologic cycle could lead to more frequent flooding and would be detrimental to agriculture that relies on consistent rainfall patterns, not extended periods without rain punctuated by extreme downpours.

Variability of clouds in subsidence regions is also consistent across time scales in the observational record, with changes indicating an increase in the strength of subsidence acting to suppress clouds. We found cloud-top heights decrease as A_u decreases along with reductions in CWV. These changes are further modifications to the hydrologic cycle, likely reducing rain in already climatologically dry regions. Reductions in clouds also act to increase both longwave cooling and shortwave warming. However, these changes are somewhat at odds with climate predictions that indicate a weakening of subsidence as the climate continues to warm. Weaker subsidence would imply increases in low clouds across descent regions, acting to reduce longwave cooling and shortwave warming; changes opposite of those observed. While Su et al. (2014) theorized a mechanism through which weakened subsidence could lead to decreases in clouds in the descent region, it is clear that cloud radiative impacts and feedbacks from subtropical clouds are still not fully understood, especially as the climate warms. Future work must also focus on the subsidence region to understand feedbacks between clouds, convection, and large-scale circulation across the Hadley Cell.

REFERENCES

Adam, O., T. Bischoff, and T. Schneider, 2016: Seasonal and interannual variations of the energy flux equator and ITCZ. Part II: Zonally varying shifts of the ITCZ. *J. Climate*, **29 (20)**, 7281–7293, doi:10.1175/JCLI-D-15-0710.1, URL https://doi.org/10.1175/JCLI-D-15-0710.1, https://doi.org/10.1175/JCLI-D-15-0710.1.

Adler, R. F., and Coauthors, 2003: The version-2 Global Precipitation Climatology Project (GPCP) monthly precipitation analysis (1979–present). *J. Hydrometeor.*, **4**, 1147–1167.

Ahmed, F., and C. Schumacher, 2015: Convective and stratiform components of the precipitation-moisture relationship. *Geophys. Res. Lett.*, **42 (23)**.

Allan, R. P., and B. J. Soden, 2008: Atmospheric warming and the amplification of precipitation extremes. *Science*, **321 (5895)**, 1481–1484, doi:10.1126/science.1160787, URL https://science.sciencemag.org/content/321/5895/1481, https://science.sciencemag.org/content/321/5895/1481.full.pdf.

Awaka, J., 1998: Early results on rain type classification by the Tropical Rainfall Measuring Mission (TRMM) precipitation radar. *Proc. 8th URSI Commission F Open Symp., Aveiro, Protugal*, 143–146.

Bain, C. L., J. De Paz, J. Kramer, G. Magnusdottir, P. Smyth, H. Stern, and C.-c. Wang, 2011: Detecting the ITCZ in instantaneous satellite data using spatiotemporal statistical modeling: ITCZ climatology in the east Pacific. *J. Climate*, **24**, 216–230.

Bartos, E. A., A. D. Rapp, and K. R. Wodzicki, 2018: Increasing frequency of midtropospheric dry layers in the Pacific intertropical convergence zone. *Geophys. Res. Lett.*, **45 (24)**, 13,523–13,529, doi:10.1029/2018GL080799, URL https://agupubs.onlinelibrary.wiley.com/doi/abs/10.1029/2018GL080799, https://agupubs.onlinelibrary.wiley.com/doi/pdf/10.1029/2018GL080799.

Berry, G., and M. J. Reeder, 2014: Objective identification of the intertropical convergence zone: Climatology and trends from the ERA-Interim. *J. Climate*, **27**, 1894–1909, doi:10.1175/JCLI-D-13-00339.1, URL https://doi.org/10.1175/JCLI-D-13-00339.1, https://doi.org/10.1175/

JCLI-D-13-00339.1.

Bony, S., and J.-L. Dufresne, 2005: Marine boundary layer clouds at the heart of tropical cloud feedback uncertainties in climate models. *Geophys. Res. Lett.*, **32 (20)**, doi:10.1029/2005GL023851, URL https://agupubs.onlinelibrary.wiley.com/doi/abs/10.1029/2005GL023851, https://agupubs.onlinelibrary.wiley.com/doi/pdf/10.1029/2005GL023851.

Bony, S., B. Stevens, D. Coppin, T. Becker, K. A. Reed, A. Voigt, and B. Medeiros, 2016: Thermodynamic control of anvil cloud amount. *Proc. Natl. Acad. Sci. (USA)*, **113 (32)**, 8927–8932, doi:10.1073/pnas.1601472113, URL https://www.pnas.org/content/113/32/8927, https://www.pnas.org/content/113/32/8927.full.pdf.

Bony, S., and Coauthors, 2015: Clouds, circulation and climate sensitivity. *Nat. Geosci.*, **8 (4)**, 261–268.

Bretherton, C. S., M. E. Peters, and L. E. Back, 2004: Relationships between water vapor path and precipitation over the tropical oceans. *J. Climate*, **17 (7)**, 1517–1528.

Bretherton, C. S., and A. H. Sobel, 2002: A simple model of a convectively coupled Walker circulation using the weak temperature gradient approximation. *J. Climate*, **15 (20)**, 2907–2920, doi:10.1175/1520-0442(2002)015<2907:ASMOAC>2.0.CO;2, URL https://doi.org/10.1175/1520-0442(2002)015<2907:ASMOAC>2.0.CO;2, https://doi.org/10.1175/1520-0442(2002)015<2907:ASMOAC>2.0.CO;2.

Byrne, M. P., A. G. Pendergrass, A. D. Rapp, and K. R. Wodzicki, 2018: Response of the intertropical convergence zone to climate change: Location, width, and strength. *Current Climate Change Reports*, **4 (4)**, 355–370, doi:10.1007/s40641-018-0110-5, URL https://doi.org/10.1007/s40641-018-0110-5.

Ceppi, P., F. Brient, M. D. Zelinka, and D. L. Hartmann, 2017: Cloud feedback mechanisms and their representation in global climate models. *WIREs Cli. Change*, **8 (4)**, e465, doi:https://doi.org/10.1002/wcc.465, URL https://onlinelibrary.wiley.com/doi/abs/10.1002/wcc.465, https://onlinelibrary.wiley.com/doi/pdf/10.1002/wcc.465.

Cheng, C.-P., and R. A. Houze, Jr., 1979: The distribution of convective and mesoscale precipita-

tion in GATE radar echo patterns. *Mon. Wea. Rev.*, **107**, 1370–1381.

Chou, C., and J. D. Neelin, 2004: Mechanisms of global warming impacts on regional tropical precipitation*. *J. Climate*, **17**, 2688–2701.

Chou, C., J. D. Neelin, C.-A. Chen, and J.-Y. Tu, 2009: Evaluating the "rich-get-richer" mechanism in tropical precipitation change under global warming. *J. Climate*, **22**, 1982–2005.

Dawson, A., 2016: Windspharm: A high-level library for global wind field computations using spherical harmonics. *J. Open Res. Software*, **4 (1)**, e31, doi:10.5334/jors.129, URL http://doi.org/10.5334/jors.129.

Dee, D., and Coauthors, 2011: The ERA-interim reanalysis: Configuration and performance of the data assimilation system. *Quart. J. Roy. Meteor. Soc.*, **137**, 553–597.

DeMott, C. A., and S. A. Rutledge, 1998: The vertical structure of TOGA COARE convection. Part I: Radar echo distributions. *J. Atmos. Sci.*, **55**, 2730–2747.

Derbyshire, S. H., I. Beau, P. Bechtold, J. Y. Grandpeix, J. L. Redelsperger, and P. M. M. Soares, 2004: Sensitivity of moist convection to environmental humidity. *Quart. J. Roy. Meteor. Soc.*, **130**, 3055–3079.

Dias, J., and O. Pauluis, 2011: Modulations of the phase speed of convectively coupled Kelvin Waves by the ITCZ. *J. Atmos. Sci.*, **68 (7)**, 1446–1459.

Dodd, J., and I. James, 1997: The impact of latent-heat release on the Hadley circulation. *Quart. J. Roy. Meteor. Soc.*, **123**, 1763–1770.

Fierro, A. O., J. Simpson, M. A. LeMone, J. M. Straka, and B. F. Smull, 2009: On how hot towers fuel the Hadley cell: An observational and modeling study of line-organized convection in the equatorial trough from TOGA COARE. *J. Atmos. Sci.*, **66**, 2730–2746.

Graham, N., and T. Barnett, 1987: Sea surface temperature, surface wind divergence, and convection over tropical oceans. *Science*, **238**, 657–659.

Gu, G., and R. F. Adler, 2013: Interdecadal variability/long-term changes in global precipitation patterns during the past three decades: global warming and/or pacific decadal variability? *Clim. Dynam.*, **40**, 3009–3022.

Gu, G., R. F. Adler, and G. J. Huffman, 2015: Long-term changes/trends in surface temperature and precipitation during the satellite era (1979–2012). *Clim. Dynam.*, 1–15, doi:10.1007/s00382-015-2634-x.

Gu, G., R. F. Adler, and A. H. Sobel, 2005: The eastern Pacific ITCZ during the boreal spring. *J. Atmos. Sci.*, **62 (4)**, 1157–1174, doi:10.1175/JAS3402.1, URL https://doi.org/10.1175/JAS3402.1, https://journals.ametsoc.org/jas/article-pdf/62/4/1157/3480863/jas3402_1.pdf.

Hack, J. J., W. H. Schubert, D. E. Stevens, and H.-C. Kuo, 1989: Response of the Hadley circulation to convective forcing in the ITCZ. *J. Atmos. Sci.*, **46**, 2957–2973.

Hawkins, E., and R. Sutton, 2012: Time of emergence of climate signals. *Geophys. Res. Lett.*, **39 (1)**, doi:https://doi.org/10.1029/2011GL050087, URL https://agupubs.onlinelibrary.wiley.com/doi/abs/10.1029/2011GL050087, https://agupubs.onlinelibrary.wiley.com/doi/pdf/10.1029/2011GL050087.

Held, I. M., and B. J. Soden, 2006: Robust responses of the hydrological cycle to global warming. *J. Climate*, **19 (21)**, 5686–5699.

Henderson, D. S., C. D. Kummerow, and W. Berg, 2018: ENSO influence on TRMM tropical oceanic precipitation characteristics and rain rates. *J. Climate*, **31 (10)**, 3979–3998.

Hilburn, K. A., and F. J. Wentz, 2008: Intercalibrated passive microwave rain products from the Unified Microwave Ocean Retrieval Algorithm (UMORA). *J. Appl. Meteor. Climatol.*, **47**, 778–794.

Hohenegger, C., and B. Stevens, 2013: Preconditioning deep convection with cumulus congestus. *J. Atmos. Sci.*, **70**, 448–464.

Holloway, C. E., A. A. Wing, S. Bony, C. Muller, H. Masunaga, T. S. L'Ecuyer, D. D. Turner, and P. Zuidema, 2017: Observing convective aggregation. *Surveys in Geophysics*, 1–38.

Hou, A. Y., and R. S. Lindzen, 1992: The influence of concentrated heating on the Hadley circulation. *J. Atmos. Sci.*, **49**, 1233–1241.

Hu, Y., and Q. Fu, 2007: Observed poleward expansion of the Hadley circulation since 1979. *Atmos. Chem. Phys.*, **7**, 5229–5236.

Hu, Y., H. Huang, and C. Zhou, 2018: Widening and weakening of the Hadley circulation under global warming. *Sci. Bull.*, **63 (10)**, 640–644, doi:https://doi.org/10.1016/j.scib.2018.04.020, URL http://www.sciencedirect.com/science/article/pii/S2095927318301919.

Hu, Y., C. Zhou, and J. Liu, 2011: Observational evidence for poleward expansion of the Hadley circulation. *Adv. Atmos. Sci.*, 33–44, doi:10.1007/s00376-010-0032-1.

Huaman, L., and K. Takahashi, 2016: The vertical structure of the eastern Pacific ITCZs and associated circulation using the TRMM precipitation radar and in situ data. *Geophys. Res. Lett.*, **43 (15)**, 8230–8239, doi:10.1002/2016gl068835, URL https://agupubs.onlinelibrary.wiley.com/doi/abs/10.1002/2016gl068835, https://agupubs.onlinelibrary.wiley.com/doi/pdf/10.1002/2016gl068835.

Hubanks, P. A., M. D. King, S. Platnick, and R. Pincus, 2019: MODIS atmosphere L3 gridded product algorithm theoretical basis document & users guide. MODIS Algorithm Theoretical Basis Document ATBD MOD 30, NASA MODIS Adaptive Processing System, Goddard Space Flight Center, USA, 129 pp. https://atmosphere imager.gsfc.nasa.gov/sites/default/files/ModAtmo/L3_ATBD_C6_C61_2019_02_20.pdf.

Huffman, G. J., R. F. Adler, D. T. Bolvin, and G. Gu, 2009: Improving the global precipitation record: GPCP version 2.1. *Geophys. Res. Lett.*, **36**.

Johnson, R. H., T. M. Rickenbach, S. A. Rutledge, P. E. Ciesielski, and W. H. Schubert, 1999: Trimodal characteristics of tropical convection. *J. Climate*, **94**, 2397–2418.

Kolly, A., and Y. Huang, 2018: The radiative feedback during the ENSO cycle: Observations versus models. *J. Geophys. Res. Atmos.*, **123 (17)**, 9097–9108, doi:https://doi.org/10.1029/2018JD028401, URL https://agupubs.onlinelibrary.wiley.com/doi/abs/10.1029/2018JD028401, https://agupubs.onlinelibrary.wiley.com/doi/pdf/10.1029/2018JD028401.

Kummerow, C., W. Barnes, T. Kozu, J. Shiue, and J. Simpson, 1998: The Tropical Rainfall Measuring Mission (TRMM) sensor package. *J. Atmos. Oceanic Technol.*, **15**, 809–817.

Lau, K.-M., and H.-T. Wu, 2007: Detecting trends in tropical rainfall characteristics, 1979–2003. *Int. J. Climatol.*, **27**, 979–988.

Lau, W. K., and K.-M. Kim, 2015: Robust Hadley circulation changes and increasing global dryness due to CO_2 warming from CMIP5 model projections. *Proc. Natl. Acad. Sci. (USA)*, **112**, 3630–3635.

Lau, W. K. M., and W. Tao, 2020: Precipitation–radiation–circulation feedback processes associated with structural changes of the ITCZ in a warming climate during 1980–2014: An observational portrayal. *J. Climate*, **33 (20)**, 8737–8749, doi:10.1175/JCLI-D-20-0068.1, URL https://doi.org/10.1175/JCLI-D-20-0068.1, https://journals.ametsoc.org/jcli/article-pdf/33/20/8737/4998534/jclid200068.pdf.

Lau, W. K.-M., H.-T. Wu, and K.-M. Kim, 2013: A canonical response of precipitation characteristics to global warming from CMIP5 models. *Geophys. Res. Lett.*, **40**, 3163–3169.

L'Heureux, M., S. Lee, and B. Lyon, 2013: Recent multidecadal strengthening of the Walker circulation across the tropical Pacific. *Nat. Clim. Change*, **3**, 571–576, doi:10.1038/nclimate1840.

Lindzen, R. S., and A. V. Hou, 1988: Hadley circulations for zonally averaged heating centered off the equator. *J. Atmos. Sci.*, **45**, 2416–2427.

Liu, C., 2013: University of Utah TRMM precipitation and cloud feature database description version 2.0. Tech. rep., University of Utah, Salt Lake City, UT, 33 pp.

Liu, C., E. J. Zipser, D. J. Cecil, S. W. Nesbitt, and S. Sherwood, 2008: A cloud and precipitation feature database from nine years of TRMM observations. *J. Appl. Meteor. Climatol.*, **47**, 2712–2728.

Liu, X., Y. Fu, and Q. Liu, 2012: Significant impacts of the TRMM satellite orbit boost on climatological records of tropical precipitation. *Chin. Sci. Bull.*, **57 (35)**, 4627–4634.

Lorenz, E. N., 1967: *The nature and theory of the general circulation of the atmosphere*. World Meteorological Organization, 161 pp.

Lu, J., G. A. Vecchi, and T. Reichler, 2007: Expansion of the Hadley cell under global warming. *Geophys. Res. Lett.*, **34**.

Manaster, A., C. W. O'Dell, and G. Elsaesser, 2017: Evaluation of cloud liquid water path trends using a multidecadal record of passive microwave observations. *J. Climate*, **30 (15)**,

5871–5884, doi:10.1175/JCLI-D-16-0399.1, URL https://doi.org/10.1175/JCLI-D-16-0399.1, https://journals.ametsoc.org/jcli/article-pdf/30/15/5871/4677956/jcli-d-16-0399_1.pdf.

Mapes, B. E., E. S. Chung, W. M. Hannah, H. Masunaga, A. J. Wimmers, and C. S. Velden, 2018: The meandering margin of the meteorological moist tropics. *Geophys. Res. Lett.*, **45 (2)**, 1177–1184.

Martin, E. R., C. R. Homeyer, R. A. McKinzie, K. M. McCarthy, and T. Xian, 2020: Regionally varying assessments of upper-level tropical width in reanalyses and CMIP5 models using a tropopause break metric. *J. Climate*, **33 (14)**, 5885–5903, doi:10.1175/JCLI-D-19-0629.1, URL https://doi.org/10.1175/JCLI-D-19-0629.1, https://journals.ametsoc.org/jcli/article-pdf/33/14/5885/4956229/jclid190629.pdf.

Masunaga, H., T. S. L'Ecuyer, and C. D. Kummerow, 2005: Variability in the characteristics of precipitation systems in the tropical Pacific. Part I: Spatial structure. *J. Climate*, **18 (6)**, 823–840.

Meng, Q., M. Latif, W. Park, N. S. Keenlyside, V. A. Semenov, and T. Martin, 2012: Twentieth century Walker circulation change: data analysis and model experiments. *Clim. Dynam.*, **38 (9)**, 1757–1773, doi:10.1007/s00382-011-1047-8, URL https://doi.org/10.1007/s00382-011-1047-8.

Mitas, C. M., and A. Clement, 2005: Has the Hadley cell been strengthening in recent decades? *Geophys. Res. Lett.*, **32**.

Mitas, C. M., and A. Clement, 2006: Recent behavior of the Hadley cell and tropical thermodynamics in climate models and reanalyses. *Geophys. Res. Lett.*, **33**, L01 810.

Myers, T. A., and J. R. Norris, 2013: Observational evidence that enhanced subsidence reduces subtropical marine boundary layer cloudiness. *J. Climate*, **26 (19)**, 7507–7524, doi:10.1175/JCLI-D-12-00736.1, URL https://doi.org/10.1175/JCLI-D-12-00736.1, https://journals.ametsoc.org/jcli/article-pdf/26/19/7507/4011136/jcli-d-12-00736_1.pdf.

Nakamura, H., and A. S. Kazmin, 2003: Decadal changes in the North Pacific oceanic frontal zones as revealed in ship and satellite observations. *J. Geophys. Res. Oceans*,

108 (C3), doi:https://doi.org/10.1029/1999JC000085, URL https://agupubs.onlinelibrary.wiley.com/doi/abs/10.1029/1999JC000085, https://agupubs.onlinelibrary.wiley.com/doi/pdf/10.1029/1999JC000085.

Neelin, J. D., C. Chou, and H. Su, 2003: Tropical drought regions in global warming and El Niño teleconnections. *Geophys. Res. Lett.*, **30 (24)**, doi:https://doi.org/10.1029/2003GL018625, URL https://agupubs.onlinelibrary.wiley.com/doi/abs/10.1029/2003GL018625, https://agupubs.onlinelibrary.wiley.com/doi/pdf/10.1029/2003GL018625.

Neelin, J. D., O. Peters, and K. Hales, 2009: The transition to strong convection. *J. Atmos. Sci.*, **66 (8)**, 2367–2384.

Neggers, R. A., J. D. Neelin, and B. Stevens, 2007: Impact mechanisms of shallow cumulus convection on tropical climate dynamics*. *J. Climate*, **20**, 2623–2642.

Nesbitt, S. W., R. Cifelli, and S. A. Rutledge, 2006: Storm morphology and rainfall characteristics of TRMM precipitation features. *Mon. Wea. Rev.*, **134**, 2702–2721.

Nesbitt, S. W., E. J. Zipser, and D. J. Cecil, 2000: A census of precipitation features in the tropics using TRMM: Radar, ice scattering, and lightning observation. *J. Climate*, **13**, 4087–4106.

Nguyen, H., A. Evans, C. Lucas, I. Smith, and B. Timbal, 2013: The Hadley circulation in reanalyses: Climatology, variability, and change. *J. Climate*, **26**, 3357–3376.

Oort, A. H., and E. M. Rasmusson, 1970: On the annual variation of the monthly mean meridional circulation. *Mon. Wea. Rev.*, **98 (6)**, 423–442, doi:10.1175/1520-0493(1970)098<0423:OTAVOT>2.3.CO;2, URL https://journals.ametsoc.org/view/journals/mwre/98/6/1520-0493_1970_098_0423_otavot_2_3_co_2.xml.

Oort, A. H., and J. J. Yienger, 1996: Observed interannual variability in the Hadley circulation and its connection to ENSO. *J. Climate*, **9 (11)**, 2751–2767, doi:10.1175/1520-0442(1996)009<2751:OIVITH>2.0.CO;2, URL https://doi.org/10.1175/1520-0442(1996)009<2751:OIVITH>2.0.CO;2, https://doi.org/10.1175/1520-0442(1996)009<2751:OIVITH>2.0.CO;2.

Oreopoulos, L., and W. B. Rossow, 2011: The cloud radiative effects of international satellite cloud climatology project weather states. *J. Geophys. Res. Atmos.*, **116 (D12)**, doi:https://doi.

org/10.1029/2010JD015472, URL https://agupubs.onlinelibrary.wiley.com/doi/abs/10.1029/2010JD015472, https://agupubs.onlinelibrary.wiley.com/doi/pdf/10.1029/2010JD015472.

O'Gorman, P. A., 2015: Precipitation extremes under climate change. *Curr. Clim. Change Rep.*, **1 (2)**, 49–59, doi:10.1007/s40641-015-0009-3, URL https://doi.org/10.1007/s40641-015-0009-3.

Pendergrass, A. G., and D. L. Hartmann, 2014: Changes in the distribution of rain frequency and intensity in response to global warming*. *J. Climate*, **27 (22)**, 8372–8383.

Physical Sciences Laboratory, 2021: Multivariate ENSO Index Version 2 (MEI.v2). Accessed 26 January 2021, https://www.psl.noaa.gov/enso/mei/.

Power, S. B., and I. N. Smith, 2007: Weakening of the Walker circulation and apparent dominance of El Niño both reach record levels, but has ENSO really changed? *Geophys. Res. Lett.*, **34 (18)**, doi:10.1029/2007GL030854, URL https://agupubs.onlinelibrary.wiley.com/doi/abs/10.1029/2007GL030854, https://agupubs.onlinelibrary.wiley.com/doi/pdf/10.1029/2007GL030854.

Rädel, G., T. Mauritsen, B. Stevens, D. Dommenget, D. Matei, K. Bellomo, and A. Clement, 2016: Amplification of El Niño by cloud longwave coupling to atmospheric circulation. *Nat. Geosci.*, **9**, 106–110, URL https://doi.org/10.1038/ngeo2630.

Rapp, A. D., C. D. Kummerow, and L. Fowler, 2011: Interactions between warm rain clouds and atmospheric preconditioning for deep convection in the tropics. *J. Geophys. Res.*, **116**, D23 210.

Rasmusson, E. M., and T. H. Carpenter, 1982: Variations in tropical sea surface temperature and surface wind fields associated with the Southern Oscillation/El Niño. *Mon. Wea. Rev.*, **110 (5)**, 354–384, doi:10.1175/1520-0493(1982)110<0354:VITSST>2.0.CO;2, URL https://doi.org/10.1175/1520-0493(1982)110<0354:VITSST>2.0.CO;2, https://doi.org/10.1175/1520-0493(1982)110<0354:VITSST>2.0.CO;2.

Rayner, N. A., D. E. Parker, E. B. Horton, C. K. Folland, L. V. Alexander, D. P. Rowell, E. C. Kent, and A. Kaplan, 2003: Global analyses of sea surface temperature, sea ice, and night marine air temperature since the late nineteenth century. *J. Geophys. Res. Atmos.*, **108 (D14)**, doi:10.1029/2002JD002670, URL https://agupubs.onlinelibrary.wiley.com/doi/abs/10.1029/2002JD002670,

https://agupubs.onlinelibrary.wiley.com/doi/pdf/10.1029/2002JD002670.

Riehl, H., and J. S. Malkus, 1958: On the heat balance in the equatorial trough zone. *Geophysica*, **6**, 503–538.

Schwendike, J., G. J. Berry, M. J. Reeder, C. Jakob, P. Govekar, and R. Wardle, 2015: Trends in the local Hadley and local Walker circulations. *J. Geophys. Res. Atmos.*, **120 (15)**, 7599–7618, doi:10.1002/2014JD022652, URL https://agupubs.onlinelibrary.wiley.com/doi/abs/10.1002/2014JD022652, https://agupubs.onlinelibrary.wiley.com/doi/pdf/10.1002/2014JD022652.

Seidel, D. J., Q. Fu, W. J. Randel, and T. J. Reichler, 2008: Widening of the tropical belt in a changing climate. *Nat. Geosci.*, **1**, 21–24.

Serra, Y. L., and R. A. Houze, Jr., 2002: Observations of variability on synoptic timescales in the east Pacific ITCZ. *J. Atmos. Sci.*, **59 (10)**, 1723–1743.

Short, D. A., P. A. Kucera, B. S. Ferrier, J. C. Gerlach, S. A. Rutledge, and O. W. Thiele, 1997: Shipboard radar rainfall patterns within the TOGA COARE IFA. *Bull. Amer. Meteor. Soc.*, **78**, 2817–2836.

Simpson, J., R. F. Adler, and G. R. North, 1988: A proposed Tropical Rainfall Measuring Mission (TRMM) satellite. *Bull. Amer. Meteor. Soc.*, **69**, 278–295.

Sohn, B. J., S.-W. Yeh, J. Schmetz, and H.-J. Song, 2013: Observational evidences of Walker circulation change over the last 30 years contrasting with GCM results. *Clim. Dynam.*, **40 (7)**, 1721–1732, doi:10.1007/s00382-012-1484-z, URL https://doi.org/10.1007/s00382-012-1484-z.

Stachnik, J. P., and C. Schumacher, 2011: A comparison of the Hadley circulation in modern reanalyses. *J. Geophys. Res.*, **116**.

Steiner, M., R. A. Houze Jr, and S. E. Yuter, 1995: Climatological characterization of three-dimensional storm structure from operational radar and rain gauge data. *J. Appl. Meteor.*, **34 (9)**, 1978–2007.

Stephens, G. L., 1990: On the relationship between water vapor over the oceans and sea surface temperature. *J. Climate*, **3 (6)**, 634–645, doi:10.1175/1520-0442(1990)003<0634:OTRBWV>2.0.CO;2, URL https://doi.org/10.1175/1520-0442(1990)003<0634:OTRBWV>2.0.CO;2, https:

//doi.org/10.1175/1520-0442(1990)003<0634:OTRBWV>2.0.CO;2.

Stephens, G. L., and Coauthors, 2018: Regional intensification of the tropical hydrological cycle during ENSO. *Geophys. Res. Lett.*, **45 (9)**, 4361–4370.

Straub, K. H., and G. N. Kiladis, 2002: Observations of a convectively coupled Kelvin Wave in the eastern Pacific ITCZ. *J. Atmos. Sci.*, **59 (1)**, 30–53.

Su, H., J. H. Jiang, C. Zhai, T. J. Shen, J. D. Neelin, G. L. Stephens, and Y. L. Yung, 2014: Weakening and strengthening structures in the Hadley circulation change under global warming and implications for cloud response and climate sensitivity. *J. Geophys. Res. Atmos.*, **119 (10)**, 5787–5805, doi:10.1002/2014JD021642, URL https://agupubs.onlinelibrary.wiley.com/doi/abs/10.1002/2014JD021642, https://agupubs.onlinelibrary.wiley.com/doi/pdf/10.1002/2014JD021642.

Su, H., L. Wu, C. Zhai, J. H. Jiang, J. D. Neelin, and Y. L. Yung, 2020: Observed tightening of tropical ascent in recent decades and linkage to regional precipitation changes. *Geophys. Res. Lett.*, **47 (3)**, e2019GL085 809, doi:10.1029/2019GL085809, URL https://agupubs.onlinelibrary.wiley.com/doi/abs/10.1029/2019GL085809, e2019GL085809 2019GL085809, https://agupubs.onlinelibrary.wiley.com/doi/pdf/10.1029/2019GL085809.

Su, H., C. Zhai, J. H. Jiang, L. Wu, J. D. Neelin, and Y. L. Yung, 2019: A dichotomy between model responses of tropical ascent and descent to surface warming. *npj Clim. Atmos. Sci.*, **2 (1)**, doi:10.1038/s41612-019-0066-8, URL https://doi.org/10.1038/s41612-019-0066-8.

Su, H., and Coauthors, 2017: Tightening of tropical ascent and high clouds key to precipitation change in a warmer climate. *Nat. Commun.*, **8**, 15 771.

Tan, J., C. Jakob, W. B. Rossow, and G. Tselioudis, 2015: Increases in tropical rainfall driven by changes in frequency of organized deep convection. *Nature*, **519 (7544)**, 451–454, URL http://dx.doi.org/10.1038/nature14339.

Tanaka, H. L., N. Ishizaki, and A. Kitoh, 2004: Trend and interannual variability of Walker, monsoon and Hadley circulations defined by velocity potential in the upper troposphere. *Tellus A*, **56 (3)**, 250–269, doi:10.3402/tellusa.v56i3.14410, URL https://doi.org/10.3402/tellusa.v56i3.14410, https://doi.org/10.3402/tellusa.v56i3.14410.

Thomson, R. E., and W. J. Emery, 2014: *Data analysis methods in physical oceanography*. Newnes.

Trenberth, K. E., J. Fasullo, and L. Smith, 2005: Trends and variability in column-integrated atmospheric water vapor. *Clim. Dynam.*, **24 (7)**, 741–758, doi:10.1007/s00382-005-0017-4, URL https://doi.org/10.1007/s00382-005-0017-4.

Tucker, G. B., 1959: Mean meridional circulations in the atmosphere. *Quart. J. Roy. Meteor. Soc.*, **85 (365)**, 209–224, doi:https://doi.org/10.1002/qj.49708536504, URL https://rmets.onlinelibrary.wiley.com/doi/abs/10.1002/qj.49708536504, https://rmets.onlinelibrary.wiley.com/doi/pdf/10.1002/qj.49708536504.

Vecchi, G. A., B. J. Soden, A. T. Wittenberg, I. M. Held, A. Leetmaa, and M. J. Harrison, 2006: Weakening of tropical Pacific atmospheric circulation due to anthropogenic forcing. *Nature*, **441 (7089)**, 73–76, doi:10.1038/nature04744, URL https://doi.org/10.1038/nature04744.

Vincent, D. G., 1994: The south pacific convergence zone (SPCZ): A review. *Mon. Wea. Rev.*, **122 (9)**, 1949–1970.

Voigt, A., S. Bony, J.-L. Dufresne, and B. Stevens, 2014: The radiative impact of clouds on the shift of the intertropical convergence zone. *Geophys. Res. Lett.*, **41 (12)**, 4308–4315, doi:10.1002/2014GL060354, URL https://agupubs.onlinelibrary.wiley.com/doi/abs/10.1002/2014GL060354, https://agupubs.onlinelibrary.wiley.com/doi/pdf/10.1002/2014GL060354.

Waliser, D. E., and C. Gautier, 1993: A satellite-derived climatology of the ITCZ. *J. Climate*, **6**, 2162–2174.

Webster, P. J., 2004: The elementary Hadley circulation. *The Hadley Circulation: Present, Past, and Future*, H. F. Diaz, and R. S. Bradley, Eds., Kluwer Academic Publisher.

Wentz, F., C. Gentemann, and K. A. Hilburn, 2015: Remote sensing systems TRMM TMI daily environmental suite on 0.25 deg grid, version 7.1. Remote Sensing Systems, Santa Rosa, CA, available online at www.remss.com/missions/tmi. Accessed June 2019.

Wentz, F. J., 1997: A well-calibrated ocean algorithm for Special Sensor Microwave/Imager. *J. Geophys. Res.*, **102**, 8703–8718.

Wodzicki, K., and A. Rapp, 2016: Long-term characterization of the Pacific ITCZ using TRMM,

GPCP, and ERA-Interim. *J. Geophys. Res. Atmos.*, **121 (7)**, 3153–3170.

Wodzicki, K. R., and A. D. Rapp, 2020: Variations in precipitating convective feature populations with ITCZ width in the Pacific ocean. *J. Climate*, **33 (10)**, 4391–4401, doi:10.1175/JCLI-D-19-0689.1, URL https://doi.org/10.1175/JCLI-D-19-0689.1, https://doi.org/10.1175/JCLI-D-19-0689.1.

Wolter, K., and M. S. Timlin, 1993: Monitoring ENSO in COADS with a seasonally adjusted principal component index. *Proc. of the 17th Climate Diagnostics Workshop*, Norman, OK, 52–7, [Available online at http://www.esrl.noaa.gov/psd/enso/mei/WT1.pdf].

Wolter, K., and M. S. Timlin, 1998: Measuring the strength of ENSO events: How does 1997/98 rank? *Weather*, **53**, 315–324.

Yin, L., R. Fu, Y.-F. Zhang, P. A. Arias, D. N. Fernando, W. Li, K. Fernandes, and A. R. Bowerman, 2014: What controls the interannual variation of the wet season onsets over the Amazon? *J. Geophys. Res. Atmos.*, **119 (5)**, 2314–2328, doi:https://doi.org/10.1002/2013JD021349, URL https://agupubs.onlinelibrary.wiley.com/doi/abs/10.1002/2013JD021349, https://agupubs.onlinelibrary.wiley.com/doi/pdf/10.1002/2013JD021349.

Yu, H., and M. Zhang, 2018: Explaining the year-to-year variability of the eastern Pacific intertropical convergence zone in the boreal spring. *J. Geophys. Res. Atmos.*, **123 (8)**, 3847–3856, doi:10.1002/2017JD028156, URL https://agupubs.onlinelibrary.wiley.com/doi/abs/10.1002/2017JD028156, https://agupubs.onlinelibrary.wiley.com/doi/pdf/10.1002/2017JD028156.

Zhang, C., 1993: Large-scale variability of atmospheric deep convection in relation to sea surface temperature in the tropics. *J. Climate*, **6 (10)**, 1898–1913, doi:10.1175/1520-0442(1993)006<1898:LSVOAD>2.0.CO;2, URL https://doi.org/10.1175/1520-0442(1993)006<1898:LSVOAD>2.0.CO;2, https://doi.org/10.1175/1520-0442(1993)006<1898:LSVOAD>2.0.CO;2.

Zhang, C., 2001: Double ITCZs. *J. Geophys. Res. Atmos.*, **106 (D11)**, 11 785–11 792, doi:10.1029/2001JD900046, URL https://agupubs.onlinelibrary.wiley.com/doi/abs/10.1029/2001JD900046, https://agupubs.onlinelibrary.wiley.com/doi/pdf/10.1029/2001JD900046.

Zhang, G., and Z. Wang, 2013: Interannual variability of the Atlantic Hadley circulation in boreal summer and its impacts on tropical cyclone activity. *J. Climate*, **26 (21)**, 8529–8544, doi:10.1175/JCLI-D-12-00802.1, URL https://doi.org/10.1175/JCLI-D-12-00802.1, https://doi.org/10.1175/JCLI-D-12-00802.1.

Zhou, Y., K.-M. Xu, Y. Sud, and A. Betts, 2011: Recent trends of the tropical hydrological cycle inferred from Global Precipitation Climatology Project and International Satellite Cloud Climatology Project data. *J. Geophys. Res.*, **116**.

APPENDIX A

ASCENT AREA FRACTION AND THE IMPACTS OF THE ω THRESHOLD

Impacts of changes to the definition of ascent area fraction (A_u) are tested to determine the sensitivity of the results to the definition. Three pressure levels are studied (700, 500, 200 hPa), with various percentiles based on the distribution of $\omega < 0.0$ used to define regions of ascent. For each pressure level, the distribution of monthly mean $|\omega|$ for all $\omega < 0.0$ between 30°S-30°N in a time period of interest are used to determine the ω threshold (ω_c) for ascent. Various percentiles of the distribution of ascent (e.g., 10th percentile, 20th percentile, etc.) are used to define ω_c. Using these cutoff values, the monthly A_u is computed by determining the fractional area of 30°S-30°N covered by grid boxes with $\omega < \omega_c$.

Figure A.1a shows ω_c as a function of ascent percentile for the three pressure levels, with Figure A.1b showing A_u as a function of ascent percentiles. The ω_c values (Figure A.1a) for the 700 hPa (black) and 500 hPa (dark gray) are nearly identical, with only slight differences between 10–40th percentile of ascent. At the 200 hPa level (light gray), however, ω_c is much weaker due to the lower

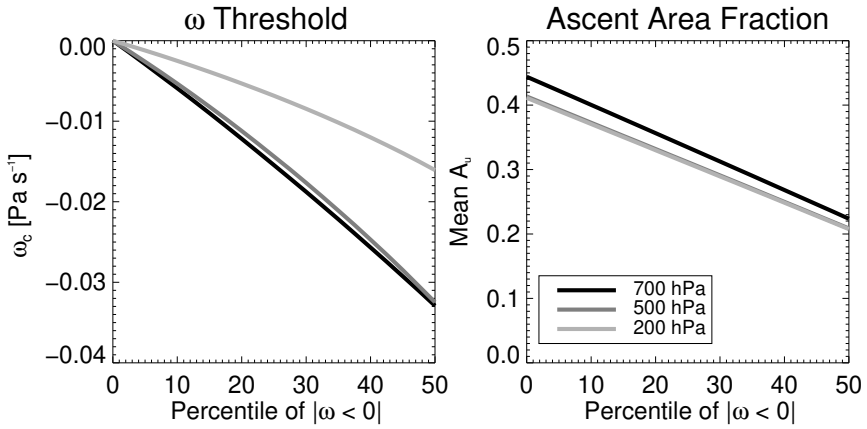

Figure A.1: Comparison of (left) cutoff values of ω used to define ascent area for various percentiles and (right) A_u for various percentiles at three pressure levels using the full ERA-Interim record.

likelihood of strong ascent at this level of the atmosphere. Comparison of mean A_u between the levels (Figure A.1b) shows that A_u for the 500 hPa (dark gray) and 200 hPa (light gray) levels are essentially identical, indicating that defining A_u using either level will produce very similar results. Defining A_u using the 700 hPa level (black) shows an increase in A_u for all ascent percentiles; ascent is much more frequent this low in the atmosphere.

To further understand the impact of pressure level and ω_c on A_u, scatter plots of monthly A_u values are created comparing A_u at 200 hPa and 700 hPa to 500 hPa. Figure A.2a-e shows monthly A_u at 500 hPa versus 200 hPa for various definitions of ω_c; correlation coefficients are shown at the top-right of each plot with correlations that are significantly different than zero at the 95% in boldface. While monthly A_u at the two levels are clearly correlated, there is some spread, with the 500 hPa level explaining only 20-40% of the variance across the different ω_c values. It is worth noting that values tend to stay close to the 1:1 line. Figure A.2f-j is similar to a-e, but for 500 hPa versus 700 hPa. The main difference between the bottom and top rows in the figure is that the 700 hPa A_u values almost always fall above the 1:1 line. However, the correlation coefficients are much

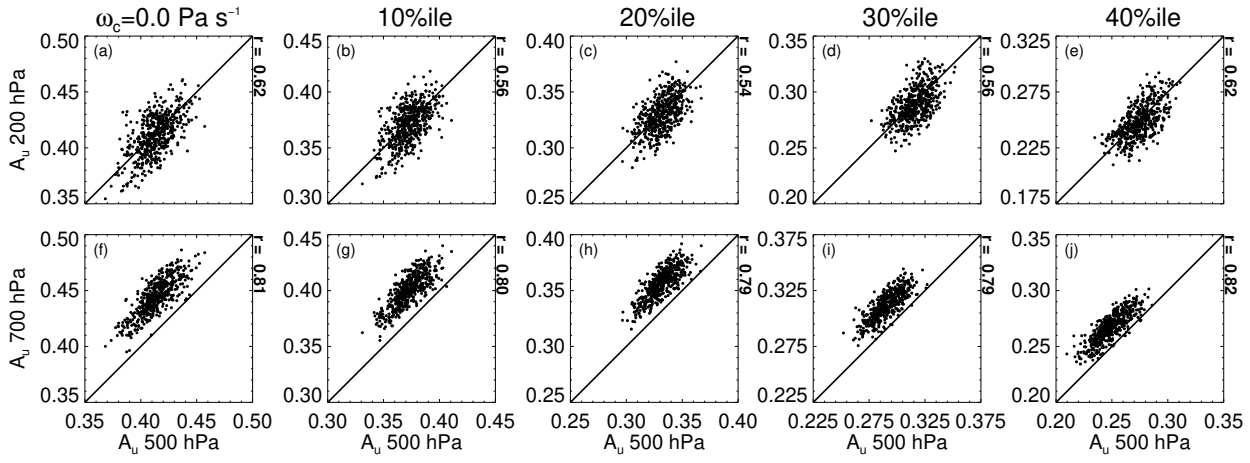

Figure A.2: Scatter plots of monthly A_u computed using (top) ω_{200} and (bottom) ω_{700} versus ω_{500}. Ascent is determined using the (a, f) Su et al. (2019) definition, (b,g) 10th percentile of ascent, (c, h) 20th percentile of ascent, (d, i) 30th percentile of ascent, and (e, j) 40th percentile of ascent. Correlation coefficients are shown at the top-right of each plot, with bold values being significantly different from zero correlation at the 95% level.

better than those of 500 hPa versus 200 hPa, with 500 hPa explaining roughly 60% of the variance in A_u at 700 hPa across the different ω_c values. The better correlation between 700 hPa and 500 hPa A_u compared to that of 500 hPa and 200 hPa is likely the result of increased correlation between the spatial patterns in ascent between the two levels. To test this, contour plots of the frequency of occurrence of ascent at each grid box are created.

Figure A.3 shows the frequency of ascent at each grid box based on ω_{700} for various ω_c values (Su et al. (2019), 10th percentile, 20th percentile, 30th percentile, and 40th percentile); Figures A.4 and A.5 show the 500 hPa and 200 hPa levels, respectively. ITCZ boundaries from the ITCZ characteristics database (Wodzicki and Rapp 2016) are also plotted on the maps for comparison. As ω_c increases moving down from panel a-e in Figure A.3, the fractional occurrence of ascent decreases everywhere, with some of the largest changes occurring over the oceans (namely the Pacific and Atlantic ITCZs). In regions where ITCZ identifications exist (Pacific and Atlantic Oceans) in Figure A.3a, there are a number of locations where ascent occurs $> 30\%$ of the time outside of the boundaries of the ITCZ, namely in the Atlantic basin, when using the Su et al. (2019) definition with $\omega_c = 0$. There also appears to be a double ITCZ signal in the eastern Pacific, with ascent occurring $> 10\%$ of the time at, and just south of, the equator. Figure A.3b shows ascent frequency if the 10th percentile of $|\omega_{700} < 0.0|$ is used to define ω_c. Panels a and b are very similar, with the most notable reductions in frequency occurring the Indian Ocean. Progressing through panels c to e shows ω_c defined using the 20th percentile, 30th percentile, and 40th percentile of ascent, respectively, indicating general reductions in the frequency of ascent throughout the domain. The influence of the double ITCZ appears at all ω_c values, with the frequency of occurrence decreasing as ω_c increases. A key finding in the analysis is that until the 20th percentile of ascent is reached for defining ω_c, ascent is fairly frequent outside of the ITCZ identifications ($> 30\%$), indicating a broader area of ascent in European Centre for Medium-Range Weather Forecasts (ECMWF) Reanalysis Interim (ERA-Interim) than may be present in reality. It is not until the 40th percentile (panel e) that frequency of ascent falls below 30% outside of the ITCZ identifications.

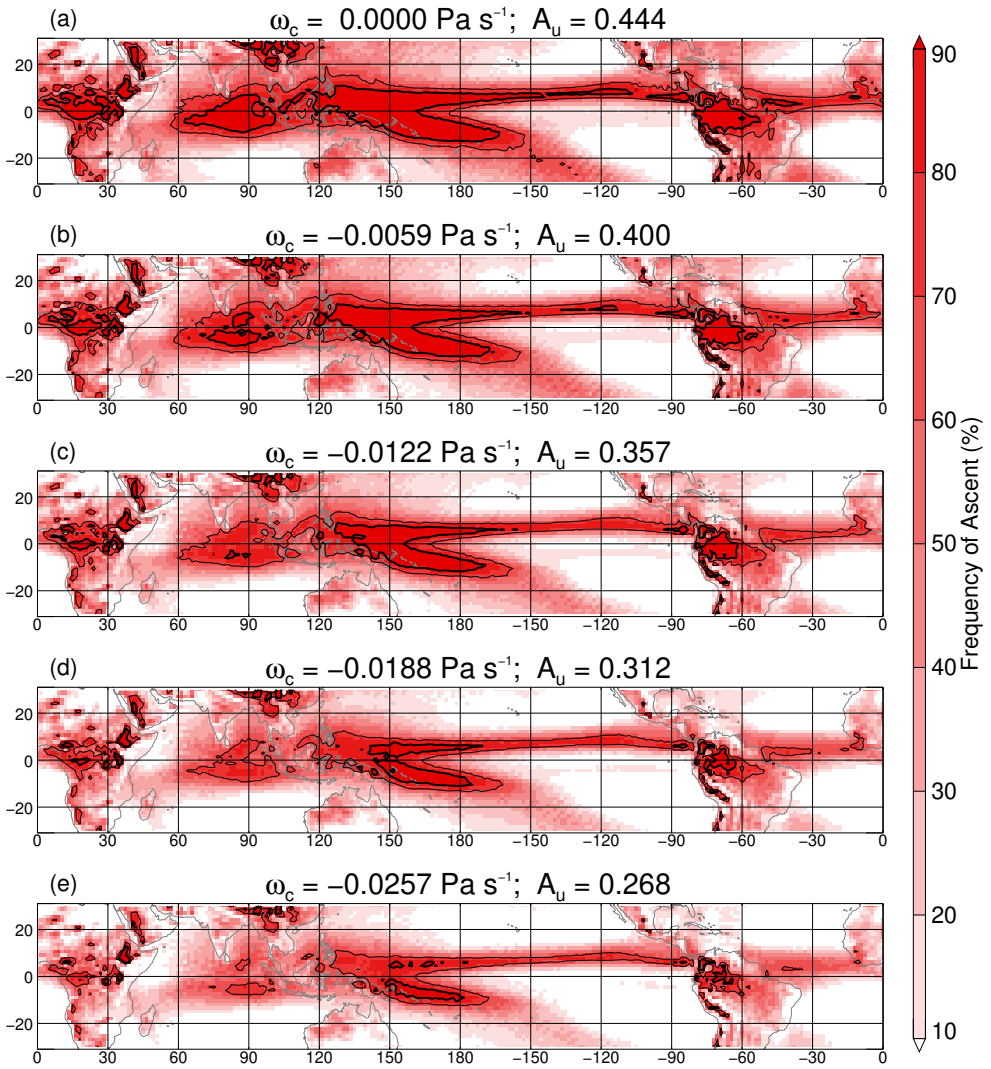

Figure A.3: Frequency of ascent at each ERA-Interim grid box over the entire ERA-Interim period (Jan. 1979-Aug. 2019) based on ω_{700}. Thin and thick contour lines highlight the 70% and 90% levels, respectively. The vertical pressure velocity threshold (ω_c) used to define ascent is determined using the (a) Su et al. (2019) definition, (b) 10th percentile of ascent, (c) 20th percentile of ascent, (d) 30th percentile of ascent, and (e) 40th percentile of ascent. ω_c and A_u are shown for each definition.

At 500 hPa, Figure A.4 shows very similar patterns to that of Figure A.3, with ascent outside of the ITCZ boundaries occurring at small $|\omega_c|$ values and a clear double ITCZ. Again, frequent ascent (occurring $>$ 40 of the time) is not really constrained to the ITCZ until the 20th percentile (Figure A.4c) is reached, with double ITCZ being present until the 40th percentile of the ascent distribution is used to define ω_c. Figure A.5 shows the 200 hPa level, which is fairly similar to 500

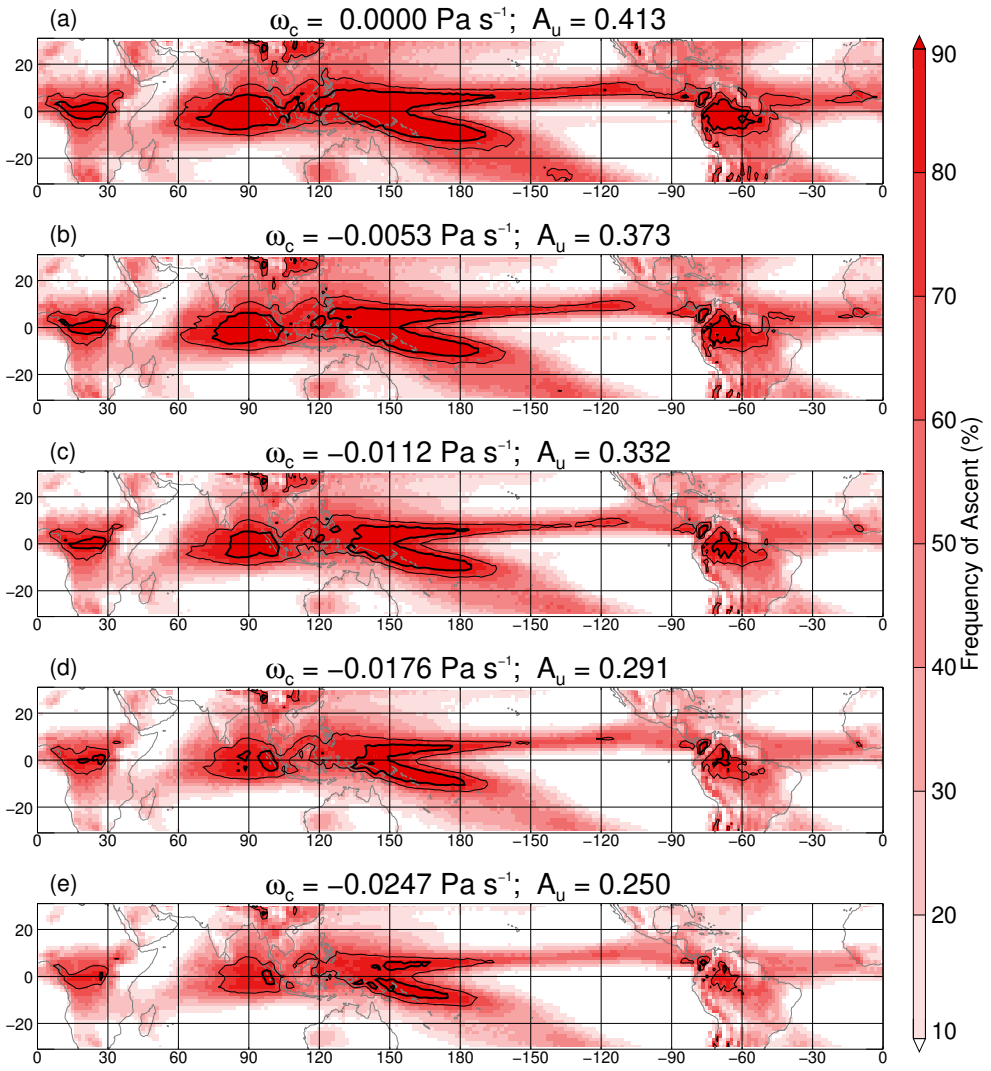

Figure A.4: As in Figure A.3, but for ω_{500}.

hPa but with generally wider meridional extent of ascent in the Pacific.

These findings show that tropical ascent area is not very sensitive to the pressure level chosen, with A_u being very similar between all pressure levels for a given ω_c. Sensitivity tests of the influence of the various A_u definitions on the results of this study showed little impact on the relationships between A_u and convective and cloud characteristics except when overly strict thresholds were used; i.e., 40th percentile or above. However, even under the strictest threshold, the interpretation of the results does not change, with relationships indicating an intensification of convection

with ascent regions with reductions in A_u. Thus, the Su et al. (2019) definition ($\omega_{500} < 0.0$) is used here to define ascent for comparison with previous works.

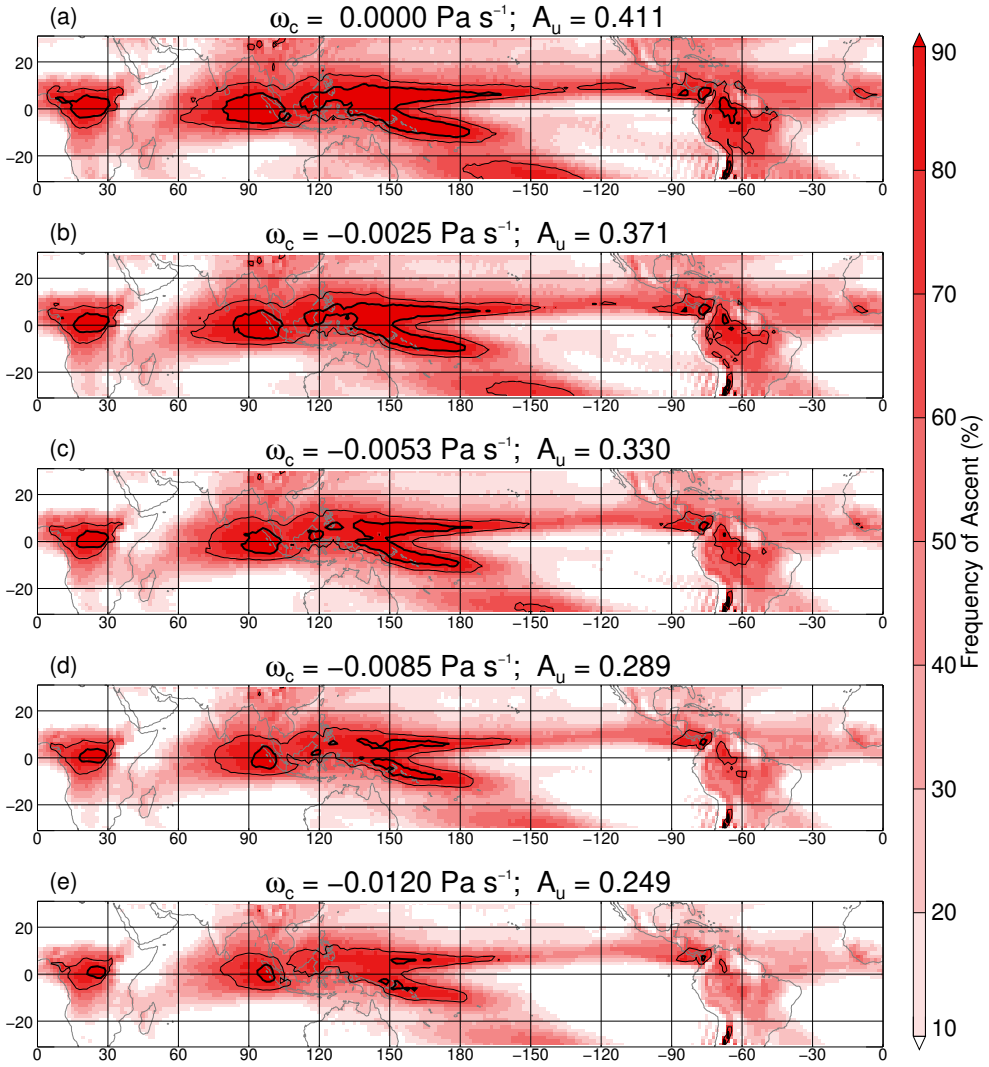

Figure A.5: As in Figure A.3, but for ω_{200}.